Doping Behavior of Cations in Perovskite-type Oxide Materials for Protonic Ceramic Fuel Cells

by

Donglin Han

Department of Materials Science and Engineering

Kyoto University

2011

Contents

Chapter 1

General Introduction

Chapter 2

Evaluation of Site Occupation of Sc, Y, Sm, Eu and Dy in BaZrO$_3$ by Comparing Lattice Volumes of Ba-rich and Ba-poor Samples

Chapter 3

Evaluation of Site Occupation of Y in BaZrO$_3$ by Powder X-ray Diffraction Based on Anomalous Dispersion Effect

Chapter 4

Evaluation of Site Occupation of Sc, Sm, Eu and Dy in BaZrO$_3$ by Powder X-ray Diffraction with Synchrotron Radiation

Chapter 5

Atmosphere Dependence of Valence State of Dy in BaZrO$_3$

Chapter 6

Preparation of La$_{1-x}$Sr$_x$Sc$_{1-y}$Fe$_y$O$_{3-\delta}$ (LSSF) Aiming Mixed Protonic and Electronic Conductive Cathode for PCFCs

Chapter 7

Chapter 1

General Introduction

The broad object of this work is to investigate the behavior of dopants when they are introduced into the perovskite-type oxides, such as clarification of their site occupation and valence state. By such investigation, some puzzled phenomena in protonic conductivity and phase transition greatly attributed to the dopants are anticipated to be revealed. In addition, some meaningful and practical knowledge is generated for guiding the further research of mixed protonic and electronic conductor for cathode material of fuel cells based on protonic conductive electrolytes.

In this chapter, essential knowledge relevant to the perovskite-type oxide, protonic ceramic fuel cells, especially their cathode material, is provided in brief.

1.1 Perovskite-type Oxides

1.1.1 Structure

Perovskite-type structure derives from the mineral perovskite, $CaTiO_3$, which was named to honor a Russian mineralogist Count Lev Alekseevich Perovskii (1792-1856). There are several alternative ways to view the perovskite structure [00Smy]. A common one which is adopted in this work is shown in Figure 1.1, with cubic structure of *pm-3m* space group for example. There are two sites for cation occupation. One 12-fold coordinated site locates at the corners of the unit cell (0,0,0), and is generally called as A-site. The other 6-fold coordinated site locates at the body center $(\frac{1}{2},\frac{1}{2},\frac{1}{2})$, and is called as B-site. Oxide ions occupy the face centers of the unit cell with the coordinates of $(0,\frac{1}{2},\frac{1}{2})$, $(\frac{1}{2},0,\frac{1}{2})$ and $(\frac{1}{2},\frac{1}{2},0)$. The formula of perovskite-type structure can therefore be expressed as ABO_3.
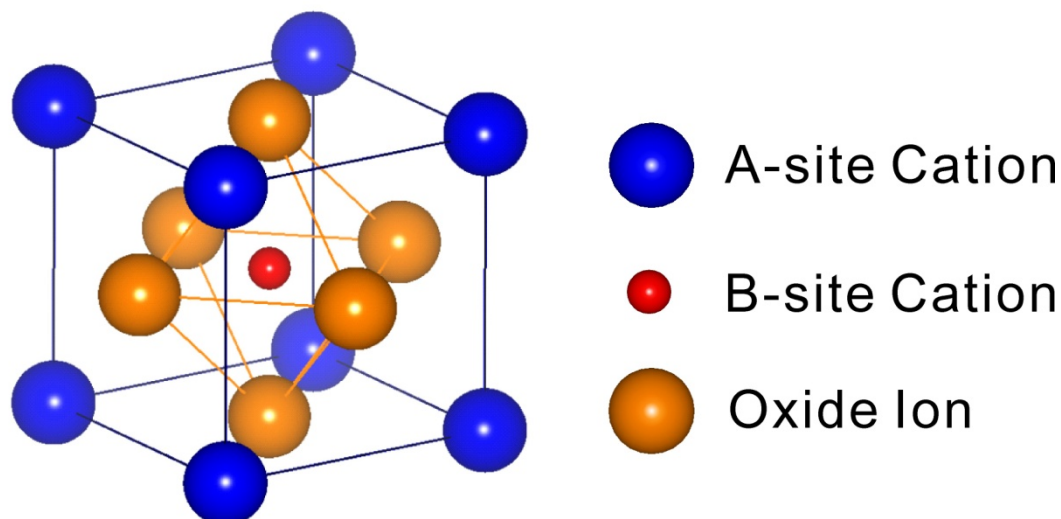
Figure 1.1 Unit cell of cubic perovskite-type structure of *pm-3m* space group.

The construction of perovskite-type structure greatly depends on the radii of the cations occupying A and B-sites. [99Hay, 01Ito, 04Li, 07Zha, 09Bha]   Since A and B sites are twelve-fold and six-fold coordinated, respectively, the cations with relatively larger size are expected to occupy the A-site, while smaller ones intend for B-site.   In order to evaluate the influence of cation radius on the perovskite-type structure more quantitatively, Goldschmidt introduced a term of tolerance factor t [26Gol] as given in Eq. (1-1), where r_A and r_B are the average radii for the cations in A and B site, respectively, and r_O is the radius of oxide ion.

$$t = \frac{r_A + r_O}{\sqrt{2}\left(r_B + r_O\right)}$$
(1-1)

Several works have been conducted to clarify the relation between the tolerance factor and the perovskite-type structure, with different range estimated for the existence of cubic structure [99Hay, 04Li, 07Zha].   Anyhow, it is generally admitted that cubic structure is preferred when the tolerance factor approaches to 1.   And structural distortion generally occurs for relaxation if the tolerance factor deviates significantly from 1.   For example, by using the Shannon radii [76Sha], the tolerance of $BaZrO_3$, which is of cubic structure at ambient environment [03Lev], is calculated to be 1.01, very close to 1.   And the tetragonal [02Aoy] and hexagonal [94Aki]

structures are reported for $BaTiO_3$, whose tolerance factor is 1.07. When relatively larger cation of Ce(IV) is introduced to occupy the B-site to form $BaCeO_3$, a tolerance factor of 0.94 is calculated and structures of orthorhombic [72Jac] and tetragonal [81Lon] are reported for measurement in ambient environment. Therefore, the tolerance factor is a meaningful indicator for evaluating the structure variation tendency in certain extent.

As has been mentioned, relatively large cations occupy the twelve-coordinated A-site, and relatively small cations occupy the six-coordinated B-site. Thus, by introducing dopant cations with different radii into the material with perovskite-type structure, different site occupation is expected to occur. For example, in the $BaTiO_3$ system, it was reported by Tsur *et al*. [01Tsu] that for doping of cations with relatively small radii, such as Lu(III) and Yb(III), the dopant cations were confirmed to occupy the B-site. However, when the radii of the dopant cations increase, Jeong *et al*. [04Jeo], Park *et al*. [09Par] found that Y(III) cations occupied both the A and B-sites, behaving as an amphoteric dopant. The similar amphoteric phenomenon was also observed for doping Dy(III) [01Tsu, 06Mia, 09Par] and Ho(III) [01Kis, 01Tsu] into $BaTiO_3$. When the cations with much larger radii were doped into $BaTiO_3$, Takeda [68Tak] found that Eu(II) cations only occupied A-site. And the same A-site occupation of Sm(III) cations was also confirmed by Goodman [63Goo], Tsur *et al*. [01Tsu]. The similar phenomena of dependence of site occupation on the radii of dopant cations were also reported in some other perovskite-type oxides, such as $BaCeO_3$ [97Mak, 04Wu, 05Wu1, 05Wu2], *etc*. However, the relevant research is insufficient for the system of $BaZrO_3$. Although several works [08Aza, 10Yam, 11Gia] have been conducted to reveal the site occupancy of dopant in Y-doped $BaZrO_3$, which attracts great interest due to its high protonic conductivity, unfortunately, no definitely confident conclusion was obtained.

1.1.2 Protonic Conductivity

The perovskite-type oxides are gifted many amazing characteristics, one of which is ionic conductivity. In the 1970s, Takahashi and Iwahara [71Tak] first reported fast ionic conductivity in Ti- and Al- based compositions. And until now, a family of perovskite-type oxides with remarkably high oxide ionic conductivity has been developed, such as $La_{1-x}Ca_xAlO_{3-\delta}$ [93Miz], $La_{0.8}Sr_{0.2}Ga_{1-y}Mg_yO_{3-\delta}$ [94Ish, 96Hua, 98Hua], *etc*. Later in the 1980s, protonic conductivity in perovskite-type oxide was also discovered by Iwahara [81Iwa, 83Iwa] in trivalent cations of Yb(III), Y(III) and Sc(III) doped $SrCeO_3$. And it became a hot subject in the relevant research field due to the possibility for application as electrolyte in fuel cells, hydrogen pumps, and various sensors, *etc.*[03Sch] After the research for about 30 years, several oxides of perovskite-type structure were confirmed to be protonic conductive in humid atmosphere [99Kre, 99Nor, 03Kre]. A high protonic conductivity about 10^{-2} Scm^{-1} was first obtained in 10% Y-doped $BaCeO_3$ for measurement in humid H_2 [00Kat], which satisfies the requirement in conductivity of 10^{-2} $S\cdot cm^{-1}$ for electrolyte in fuel cells [01Ste]. However, $BaCeO_3$ is unstable in CO_2 contained atmosphere [93Gap, 93Sch, 96Tan]. In contrast, doped $BaZrO_3$ exhibits significant stability against CO_2 [00Kat, 09Gu1], together with remarkably high protonic conductivity in humid atmosphere (about 10^{-2} $S\cdot cm^{-1}$ at 450^oC [09Yam]), therefore, is regarded to be a promising candidate for electrolyte in fuel cells. In addition to $BaCeO_3$ and $BaZrO_3$, several other perovskite-type oxides, such as $La_{1-x}Sr_xScO_{3-\delta}$ [97Nom, 99Lyb, 02Nom], $La_{1-x}Sr_xYO_{3-\delta}$ [97Rui, 00Rui] and $La_{1-x}Ba_xScO_{3-\delta}$ [01Kim, 02Lee] *etc*., also exhibit protonic conduction in humid atmosphere. However, their conductivities are not comparable to the values of doped $BaZrO_3$ and $BaCeO_3$ until now, and further investigation is essential.

Referring to the mechanism of protonic conductivity in perovskite-type oxides, trivalent cation (M(III)) doped $BaZrO_3$ is taken as example for explanation. When dopant cations are introduced into $BaZrO_3$, they conventionally occupy the B-site in $BaZrO_3$, namely partially

replace the Zr(IV) cations.　Then oxide ion vacancies ($V_O^{\bullet\bullet}$) are generated consequently for charge compensation, as given in Eq. (1-2).

$$2Zr_{Zr}^{\times} + M_2O_3 + O_O^{\times} \rightarrow 2ZrO_2 + 2M_{Zr}^{'} + V_O^{\bullet\bullet} \tag{1-2}$$

When the material is placed in humid atmosphere, water molecules are absorbed, and as given in Eq. (1-3), dissociate into hydroxide, which fill oxide ion vacancies, and protons, which form hydroxide ions with lattice oxide ions.　The protons rotate around the lattice oxide ions and jump in the network among them, by which the protonic conductivity is generated.　This way of free proton migration is also referred to be as Grotthuss mechanism [82Iwa, 86Nor, 04Nor].　From Eq. (1-3), it is clear that the existence of oxide ion vacancies is essential for protonic conductivity.

$$H_2O + V_O^{\bullet\bullet} + O_O^{\times} \rightarrow 2OH_O^{\bullet} \tag{1-3}$$

However, as has been illustrated in 1.1.3, it is also possible for dopant cations to occupy the A-site.　Under such circumstance, as shown in Eq. (1-4), the dopant cations with relatively higher valence state substitute Ba(II) cations.　Then, oxide ion vacancies are consumed for charge compensation.　Therefore, the A-site occupation of dopant cations is unfavorable for protonic conductivity.　And understanding the site occupation of dopants, also their influences on proton incorporation is considered to be meaningful for further elevating the protonic conductivity.

$$2Ba_{Ba}^{\times} + M_2O_3 + V_O^{\bullet\bullet} \rightarrow 2BaO + 2M_{Ba}^{\bullet} + O_O^{\times} \tag{1-4}$$

1.2 Solid Oxide Fuel Cell and Protonic Ceramic Fuel Cell

As an alternative method for electrochemically converting chemical energy of hydrocarbon fuels into electricity, fuel cells is gaining increasing attention in recent years for clean and efficient distributed power generation.　And solid oxide fuel cell (SOFC), which uses oxide ion conductor as electrolyte, is the most efficient one, with the conversion

efficiency approaching 75% [03Sin].   The way how SOFC works can be understood briefly from the schematic in Figure 1.2.   Oxide ions are formed by reducing oxygen molecules at the cathode, and move across the electrolyte to the cathode, then react with fuel, such as H_2 for example, to produce water.   And simultaneously, current is generated in the closed circuit.   However, although SOFC is attractive for high efficiency, it meets some unconquerable disadvantages such as fuel dilution at the anode due to by-product of water, and high operation temperature around 800 to $1000^o C$ for generation of significant oxide ionic conductivity, resulting in the severe requirement for structural materials.
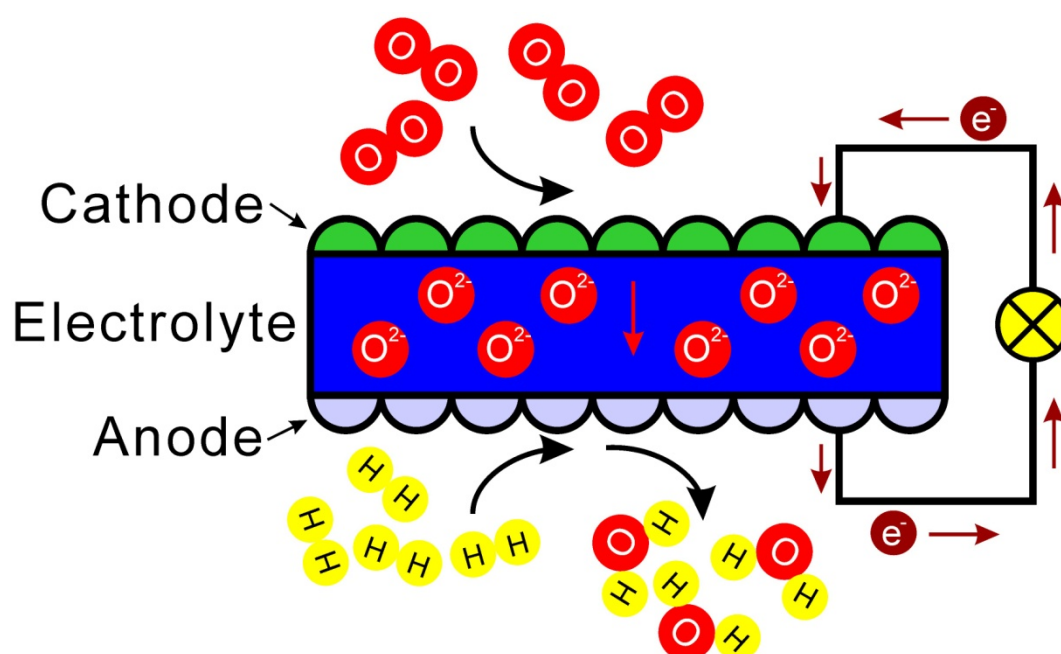

Figure 1.2 Schematic of a solid oxide fuel cell.   Oxide ions move in electrolyte from anode to cathode, and react with hydrogen molecules to generate water molecules and electrons at the anode.

In contrary, fuel cells based on protonic conductive ceramic as electrolytes, generally named as protonic ceramic fuel cells (PCFCs) [03Coo, 04Coo], operate at the intermediate temperature range about 600 to $700^o C$ [09Lef], therefore, some common materials like stainless steel can be applied as separator or structural materials.   The schematic of PCFC is as shown in Figure 1.3.   Different from SOFC, protons play the role of carriers in PCFC, and move in

the electrolyte from anode to cathode. Then protons react with oxygen and electrons at the cathode to form water. Therefore, no dilution of fuel occurs for PCFC, indicating a more efficient fuel usage. Based on these advantages, PCFC attracts great interest. Although it is not practically commercialized like SOFC, some exiting results have been achieved in laboratory scale. Ito *et al.* [05Ito] prepared a cell with the $BaCe_{0.8}Y_{0.2}O_{3-\delta}$ as electrolyte which was deposited by pulsed laser deposition (PLD) on Pd hydrogen permeation membrane as supporting anode. And a maximum power density of 1.4 Wcm^{-2}, which is the record for PCFC until now, was obtained. The reported PCFC performances with Y-doped $BaZrO_3$ as electrolyte are summarized in Table 1.1. The performance is greatly dependent on the electrolyte thickness, and is not comparable to that of the PCFC with doped $BaCeO_3$ as electrolyte. Therefore, further effort is essential in thinning the electrolyte, and elevating the electrode performance.
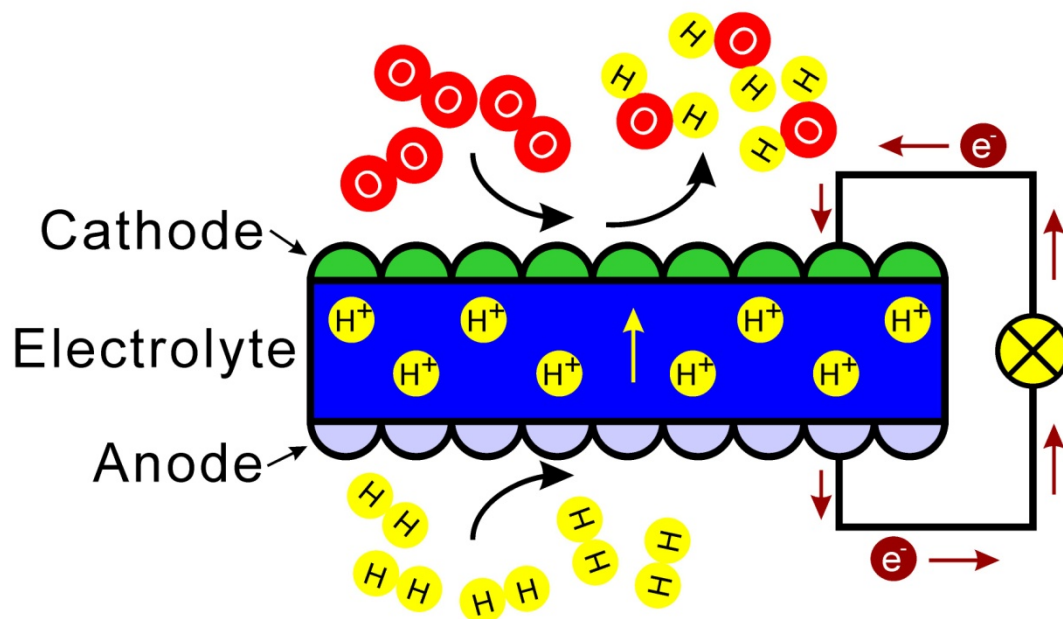

Figure 1.3 Schematic of a protonic ceramic fuel cell. Protons move in electrolyte from anode to cathode, and react with oxygen molecules and electrons to form water molecules at the cathode.

Table 1.1 Main experimental parameters of PCFCs based on Y-doped $BaZrO_3$ as electrolyte. The relative maximum power densities were obtained by using humid H_2 as fuel and air as oxidant.

Ref.	Electrolyte		Thickness / μm	Anode	Cathode	Open circuit voltage at 600°C / V	Maximum power density at 600°C / $mWcm^{-2}$
	Composition	Deposition method					
[08Epi]	$BaZr_{0.8}Y_{0.2}O_{3-\delta}$	Sintering at 1600°C	600	NiO - $BaZr_{0.8}Y_{0.2}O_{3-\delta}$ (7:3)	$La_{0.8}Sr_{0.2}Co_{0.8}Fe_{0.2}O_{3-\delta}$	~ 1.0	~ 6.7
[10Per]	$BaZr_{0.8}Y_{0.2}O_{3-\delta}$	Pulsed laser deposition	4	NiO - $BaZr_{0.8}Y_{0.2}O_{3-\delta}$ (1:1)	$La_{0.6}Sr_{0.4}Co_{0.2}Fe_{0.8}O_{3-\delta}$ - $BaCe_{0.9}Yb_{0.1}O_{3-\delta}$ (1:1)	0.99	110
[10Sun]	$BaZr_{0.8}Y_{0.2}O_{3-\delta}$	Dry-pressing, co-firing at 1400°C	20	NiO - $BaZr_{0.1}Ce_{0.7}Y_{0.2}O_{3-\delta}$ (3:2)	$Sm_{0.5}Sr_{0.5}CoO_{3-\delta}$ - $Ce_{0.8}Sm_{0.2}O_{3-\delta}$ (3:2)	1.014	70
[07Igu]	$BaZr_{0.95}Y_{0.05}O_{3-\delta}$	Sintering at 1800°C	500	Pt	Ag	1.05	~ 3.8
[08Igu]	$BaZr_{0.85}Y_{0.15}O_{3-\delta}$	Sintering at 1800°C	500	Pt	Ag	1.05	
[09Shi]	$BaZr_{0.8}Y_{0.2}O_{3-\delta}$	Pulsed laser deposition	0.13	Pt	Pt	0.45 (at 450°C)	120 (at 450°C)
[11Kan]	$BaZr_{0.8}Y_{0.2}O_{3-\delta}$	Pulsed laser deopsition	1	Pd	Pt	~ 1 (at 400°C)	9.1 (at 400°C)

1.3 Cathode Materials for PCFCs

Conventionally, cathode reaction for PCFCs, as given in Eq. (1-5), occurs at the three-phase-boundary (TPB) where electrolyte, gas and cathode meet, as shown in Figure 1.4(a).

$$4H^+ + O_2 + 4e^- \rightarrow 2H_2O \tag{1-5}$$

Based on such mechanism, a couple of electronic conductive materials has been verified for application as cathode material, such as metals like Pt [82Iwa, 85Uch, 88Iwa, 90Iwa], Ag [07Igu, 07Igu], etc., and electronic conductive oxides like $La_{0.7}Sr_{0.3}FeO_{3-\delta}$ [05Yam], $La_{0.6}Sr_{0.4}CoO_{3-\delta}$ [04Maf], $La_{0.8}Sr_{0.2}Co_{0.8}Fe_{0.2}O_{3-\delta}$ [08Epi], $Ba_{0.5}Sr_{0.5}Co_{0.8}Fe_{0.2}O_{3-\delta}$ [09Gu2], $La_{0.6}Ba_{0.4}Co_{0.8}O_{3-\delta}$ [93Iwa], $Ba_{0.5}Pr_{0.5}CoO_{3-\delta}$ [02Hib], etc. And in order to elevate the cathode performance, attempts for preparing composite cathode were also conducted [07Yan, 09Fab, 10Per], by which TPB was expected to be increased.
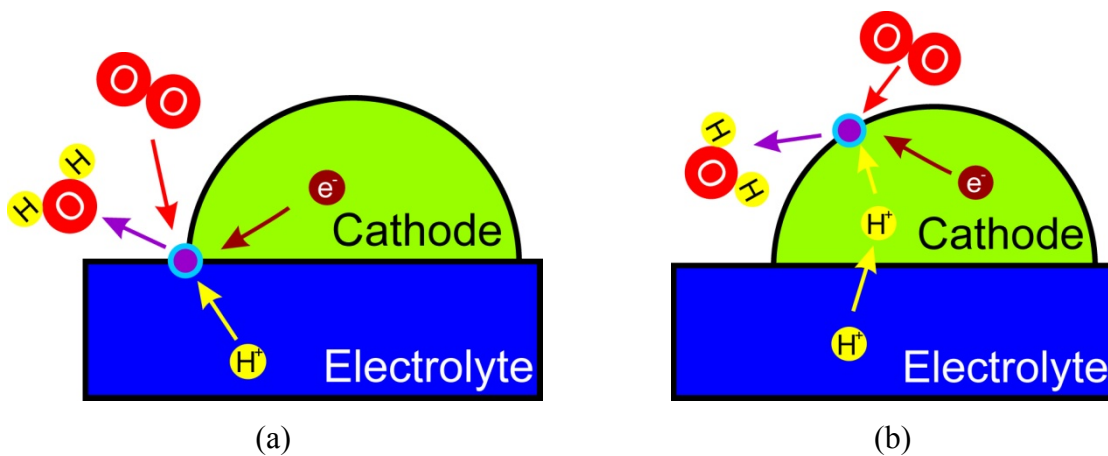

Figure 1.4 Reactive sites for cathode reaction of (a) three-phase-boundary, where cathode, electrolyte, and gas phases meet, and (b) surface of cathode material.

However, compared with increasing reactive sites for cathode reaction by extending TPB, it is more attractive if the whole interface between the cathode and gas phase is reactive [10Fab], as shown in Figure 1.4(b). Theoretically, such idea can be realized if the cathode material is mixed protonic and electronic conductive. Thus, protons can migrate across the

interface between electrolyte and cathode, and move to the surface of cathode, thereby the cathode reaction can occur at the entire surface of cathode. Relatively limited works have been conducted for preparing the mixed protonic and electronic conductor. Song et al. [03Son, 05Son, 07Son] attempted to introduce Eu and Yb into SrCeO$_3$. And Fabbri et al [09Fae] doped Yb, Eu, Sm into SrCeO$_3$ and BaCeO$_3$. However, their researches did not succeed in obtaining a novel mixed protonic and electronic conductor appropriate for the application as cathode for PCFCs. Anyhow, such work is attractive and worth continuously challenging.

References

[26Gol] V.M. Goldschmidt, *Naturwissenschaften* 14 (1926) 477-485.

[63Goo] G. Goodman, *J. Am. Ceram. Soc.* 46 (1963) 48-54.

[68Tak] T. Takeda, *J. Phys. Soc. Jpn.* 24 (1968) 533-542.

[71Tak] T. Takahashi, H. Iwahara, *Energy Conversion* 11 (1971) 105-111.

[72Jac] A.J. Jacobson, B.C. Tofield, B.E.F. Fender, *Acta Crystallogr. B* 28 (1972) 956-961.

[76Sha] R.D. Shannon, *Acta Crystallogr. A* 32 (1976) 751-767.

[81Iwa] H. Iwahara, T. Esaka, H. Uchida, N. Maeda, *Solid State Ionics* 3-4 (1981) 359-363.

[81Lon] V. Longo, D. Minichelli, *J. Mater. Sci.* 16 (1981) 3503-3505.

[82Iwa] H. Iwahara, H. Uchida, N. Maeda, *J. Power Source* 7 (1982) 293-301.

[83Iwa] H. Iwahara, H. Uchida, S. Tanaka, *Solid State Ionics* 9-10 (1983) 1021-1026.

[85Uch] H. Uchida, S. Tanaka, H. Iwahara, *J. Appl. Electrochem.* 15 (1985) 93-97.

[86Nor] T. Norby, P. Kofstad, *Solid State Ionics* 20 (1986) 169-184.

[88Iwa] H. Iwahara, H. Uchida, K. Ono, *J. Electrochem. Soc.* 135 (1988) 529-533.

[90Iwa] H. Iwahara, H. Uchida, K. Morimoto, *J. Electrochem. Soc.* 137 (1990) 462-465.

[93Iwa] H. Iwahara, T. Yajima, T. Hibino, H. Ushida, *J. Electrochem. Soc.* 140 (1993) 1687-1691.

[93Miz] J. Mizusaki, I. Yasuda, J. Shimoyama, S. Yamauchi, K. Fueki, *J. Electrochem. Soc.* 140 (1993) 467-471.

[93Gap] S. Gapalan, A.V. Virkar, *J. Electrochem. Soc.* 140 (1993) 1060-1065.

[93Sch] M.J. Scholten, J. Schoonman, *Solid State Ionics* 61 (1993) 83-91.

[94Aki] J. Akimoto, Y. Gotoh, Y. Oosawa, *Acta Crystallogr. C* 50 (1994) 160-161.

[94Ish] T. Ishihara, H. Matsuda, Y. Takita, *J. Am. Chem. Soc.* 116 (1994) 3801-3803.

[96Hua] P. Huang, A. Petric, *J. Electrochem. Soc.* 143 (1996) 1644-1648.

[96Tan] C.W. Tanner, A.V. Virkar, *J. Electrochem. Soc.* 143 (1996) 1386-1389.

[97Mak] D. Makovec, Z. Samardzija, D. Kolar, *J. Am. Ceram. Soc.* 80 (1997) 3145-3150.

[97Nom] K. Nomura, S. Tanase, *Solid State Ionics* 98 (1997) 229-236.

[97Rui] E. Ruiz-Trejo, J.A. Kilner, *Solid State Ionics* 97 (1997) 529-534.

[98Hua] K. Huang, R.S. Tichy, J.B. Goodenough, *J. Am. Ceram. Soc.* 81 (1998) 2565-2575.

[99Hay] H. Hayashi, H. Inaba. M. Matsuyama, N.G. Lan, M. Dokiya, H. Tagawa, *Solid State Ionics* 122 (1999) 1-15.

[99Kre] K.D. Kreuer, *Solid State Ionics* 97 (1997) 1-15.

[99Nor] T. Norby, *Solid State Ionics* 125 (1999) 1-11.

[99Lyb] D. Lybye, N. Bonanos, *Solid State Ionics* 125 (1999) 399-344.

[00Kat] K. Katahira, Y. Kohchi, T. Shimura, H. Iwahara, *Solid State Ionics* 138 (2000) 91-98.

[00Smy] D.M. Smyth, *The Defect Chemistry of Metal Oxides*, Oxford University Press, Inc., Oxford (2000).

[01Ito] K. Ito, K. Tezuka, Y. Hinatsu, *J. Solid State Chem.* 157 (2001) 173-179.

[01Kim] S. Kim, K. Lee, h. Lee, *Solid State Ionics* 144 (2001) 109-115.

[01Kis] H. Kishi, N. Kohzu, Y. Iguchi, J. Sugino, M. Kato, H. Ohsato, T. Okuda, *J. Eur. Ceram. Soc.* 21 (2001) 1643-1647.

[00Rui] E. Ruiz-Trejo, J.A. Kilner, *Solid State Ionics* 130 (2000) 313-324.

[01Ste] B.C.H. Steele, A. Heinzel, *Nature* 414 (2001) 345-352.

[01Tsu] Y. Tsur, A. Hitomi, I. Scrymgeour, C. Randall, *Jpn. J. Appl. Phys*. 40 (2001) 255-258.

[02Aoy] S. Aoyagi, Y. Kuroiwa, A. Sawada, I. Yamashita, T. Akate, *J. Phys. Soc. Jpn.* 71 (2002) 1218-1221.

[02Hib] T. Hibino, A. Hashimoto, M. Suzuki, M. Sano, *J. Electrochem. Soc.* 149 (2002) A1503-A1508.

[02Lee] K. Lee, H. Kim, S. Kim, H. Lee, *J. Ceram. Process. Res*. 3 (2002) 128-131.

[02Nom] K. Nomura, T. Takeuchi, S. Tanase, H. Kageyama, K. Tanimoto, Y. Miyazaki, *Solid State Ionics* 154-155 (2002) 647-652.

[03Coo] W.G. Coors, *J. Power Sources* 118 (2003) 150-156.

[03Kre] K.D. Kreuer, *Annu. Rev. Mater*. Res. 33 (2003) 333-359.

[03Lev] I. Levin, T.G. Amos, S.M. Bell, L. Farber, T.A. Vanderah, R.S. Roth, B.H. Toby, *J. Solid State Chem.* 175 (2003) 170-181.

[03Sch] T. Schober, *Solid State Ionics* 162-163 (2003) 277-281.

[03Sin] S.C. Singhal, K. Kendall, *High Temperature Solid Oxide Fuel Cells, Fundamentals, Design and Applications*, Elesevier, Oxford (2003).

[03Son] S. Song. E.D. Wachsman, S.E. Dorris, U. Balachandran, *J. Electrochem. Soc.* 150 (2003) A1484-A1490.

[04Coo] W.G. Coors, *J. Electrochem. Soc.* 151 (2004) A994-A997.

[04Jeo] J. Jeong, M. Park, Y. Han, *J. Electroceram*. 13 (2004) 805-809.

[04Li] C. Li, K.C.K. Soh, P. Wu, *J. Alloys Compd.* 372 (2004) 40-48.

[04Maf] N. Maffei, L. Pelletier, A. McFarlan, *J. Power Sources* 136 (2004) 24-29.

[04Nor] T. Norby, M. Widerøe, R. Glöckner; Y. Larring, *Dalton Trans.* (2004) 3012-3018.

[04Wu] J. Wu, L. Li, W.T.P. Espinosa, S.M. Haile, *J. Mater. Res.* 19 (2004) 2366-2376.

[05Ito] N. Ito, M. Iijima, K. Kimura, S. Iguchi, *J. Power Sources* 152 (2005) 200-203.

[05Son] S. Song, E.D. Wachsman, J. Rhodes, H. Yoon, K. Lee, *J. Mater. Sci.* 40 (2005) 4061-4066.

[05Wu1] J. Wu, S.M. Webb, S. Brennan, S.M. Haile, *J. Appl. Phys*. 97 (2005) 054101.

[05Wu2] J. Wu, R.A. Davies, M.S. Islam, S.M. Haile, *Chem. Mater.* 17 (2005) 846-851.

[05Yam] H. Yamamura, T. Ikuta, H. Yahiro, G. Okada, *Solid State Ionics* 176 (2005) 269-274.

[06Mia] H. Miao, M. Dong, G. Tan, Y. Pu, *J. Electroceram.* 16 (2006) 297-300.

[07Igu] F. Iguchi, T. Tokikawa, T. Miyoshi, T. Tsurui, Y. Nagao, N, Sata, H. Yugami, *ECS Transactions* 7 (2007) 2331-2336.

[07Son] S. Song, H. Park, *J. Mater. Sci.* 42 (2007) 6177-6182.

[07Yan] L. Yang, C. Zuo, S. Wang, Z. Cheng, M. Liu, *Adv. Mater.* 20 (2008) 3280-3283.

[07Zha] H. Zhang, N. Li, K. Li, D. Xue, *Acta. Crystallogr. B* B63 (2007) 812-818.

[08Aza] A.K. Azad, C. Savaniu, S. Tao, S. Duval, P. Holtappels, R.M. Ibberson, J.T.S. Irvine, *J. Mater. Chem.* 18 (2008) 3414-3418.

[08Igu] F. Iguchi, N. Sata, Y. Hiroo, *Proceedings of Fuel Cell 2008*, Denver, 2008, pp. 79-84.

[08Epi] A.D'Epifanio, E. Fabbri, E. Di Bartolomeo, S. Licoccia, E. Traversa, *Fuel Cells* 1 (2008) 69-76.

[09Bha] M. Bharathy, A.H. Fox, S.J. Mugavero, H.-C. zur Loye, *Solid State Sci.* 11 (2009) 651-654.

[09Fab] E. Fabbri, S. Licoccia, E. Traversa, E.D. Wachsman, *Fuel Cells* 2 (2009) 128-138.

[09Fae] E. Fabbri, T. Oh, S. Licoccia, E. Traversa, E.D. Wachsman, *J. Electrochem. Soc.* 156 (2009) B38-B45.

[09Gu1] Y. Guo, Y. Lin, H. Shi, R. Ran, Z. Shao, *Chin. J. Catal*. 30 (2009) 479-481.

[09Gu2] Y. Guo, Y. Lin, R. Ran, Z. Shao, *J. Power Sources* 193 (2009) 400-407.

[09Lef] F. Lefebvre-Joud, G. Gauthier, J. Mougin, *J. Appl. Electrochem.* 39 (2009) 535-543.

[09Par] K. Park, C. Kim, Y. Yoon, S. Song, Y. Kim, K. Hur, *J. Eur. Ceram. Soc.* 29 (2009) 1735-1741.

[09Shi] J. Shim, J. Park, J. An, T. Gür, S.Kang, F.B. Prinz, *Chem. Mater.* 21 (2009) 3290-3296.

[09Yam] Y. Yamasaki, R. Hernandez-Sanchez, S.M. Haile, *Chem. Mater.* 21 (2009) 2755-2762.

[10Fab] E. Fabbri, D. Pergolesi, E. Traversa, *Sci. Technol. Adv. Mater.* 11 (2010) 044301.

[10Per] D. Pergolesi, E. Fabbri, E. Traversa, *Electrochem. Commun.* 12 (2010) 977-980.

[10Sun] W. Sun, L. Yan, Z. Shi, Z. Zhu, W. Liu, *J. Power Sources* 195 (2010) 4727-4730.

[10Yam] Y. Yamazaki, R, Hernandez-Sanchez, S.M. Haile, *J. Mater. Chem.* 20 (2010) 8158-8166.

[11Gia] F. Giannici, M. Shirpour, A. Longo, A. Martorana, R. Merkle, J. Maier, *Chem. Mater.* DOI: 10.1021/cm200682.

[11Kan] S. Kang, P. Heo, Y. Lee, J. Ha, I. Chang, S. Cha, *Electrochem. Commun.* 13 (2011) 374-377.

Chapter 2

Evaluation of Site Occupation of Sc, Y, Sm, Eu and Dy in BaZrO$_3$ by Comparing Lattice Volumes of Ba-rich and Ba-poor Samples

2.1 Introduction

As illustrated in Chapter 1, the protons, which are the carriers for protonic conductivity, are introduced by dissociative dissolving of water molecules into oxide ion vacancies. By doping of trivalent cations into BaZrO$_3$, oxide ion vacancies are consumed or generated, corresponding to the A or B-site occupation of the dopant cations, respectively. Therefore, site selectivity of dopant cations has direct influence on the protonic conductivity that which site dopant cations occupy when they are doped into BaZrO$_3$. However, the research about the site occupation of dopant cations in BaZrO$_3$ is limited. In this chapter, the site selectivity of Sc, Y, Sm, Eu and Dy is evaluated by comparing the lattice volume of Ba-rich and Ba-poor samples.
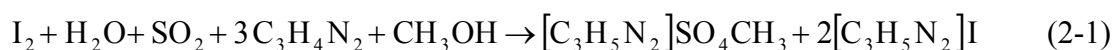

2.2 Experimental

2.2.1 Material Preparation

Samples were fabricated by conventional solid state reaction. Starting materials were prepared by mixing BaCO$_3$, ZrO$_2$, and M$_2$O$_3$ (M = Sc, Y, Sm ,Eu or Dy) at the desired ratios. After ball-milling for 24 h, the mixtures were pressed into pellets under 9.8 MPa and heated at 1000 $^{\circ}$C for 10 h. The samples were then ball-milled for 10 h, and pressed into pellets under 9.8 MPa again, followed by a subsequent heat treatment at 1300 $^{\circ}$C for 10 h. The procedure of the ball-milling for 10 h and heat treatment at 1300 $^{\circ}$C for 10 h was repeated for three times at most. After that, the samples were ball-milled for 10 h and mixed with an organic binder solution consisting of water, polyvinyl alcohol, glycerin and ethanol. The mixtures were

then pressed into pellets at 392 MPa, followed by a subsequent heat treatment at 600 $^{\circ}$C for 8 h to remove the binder solution.　Finally, the pellets were heated up to the sintering temperature of 1600 $^{\circ}$C at a heating rate of 4 $^{\circ}$Cmin^{-1}, and kept for 24 h in O_2 flow, then furnace-cooled to room temperature.　In this work, structures of the samples were identified by X-ray diffraction analysis (XRD, PANalytical B. V., X'Pert-ProMPD, Cu Kα).　Rietveld refinement was carried out by utilizing a commercial software X'Pert HighScore Plus (PANalytical B. V.) to determine lattice volumes.　And morphologies of the sintered pellets were evaluated by a scanning electron microscope (SEM, Keyence Co., VE-7800).

2.2.2 Measurement of Water Content

Water contents of the hydrated samples were measured by Karl-Fischer titration method.　The sintered pellets were broken into pieces about 2 mm in length, and hydrated for 72 h at the desired temperature in atmosphere of 5% H_2O - Ar or 5% H_2O - O_2 for saturation of water.　Powder samples were not used, in order to eliminate the interference of surface water.　After that, the samples were quenched at room temperature to hold the water absorbed, and subsequently placed in a furnace already kept at 1000°C to dehydrate, as shown in Figure 2.1.　Water vapor was carried by dry N_2 flow (200 ml/min) into the titration cell, and induced a reaction consuming I_2 molecules to form I$^-$ anions as Eq. (2-1).　The same amount of I$^-$ anions were oxidized electrochemically to I_2 molecules as Eq. (2-2), where the end point is detected by a bipotentiometric method.　Thus, by measuring the electrons exchanged during the electrolysis, the water contents in the samples were determined.
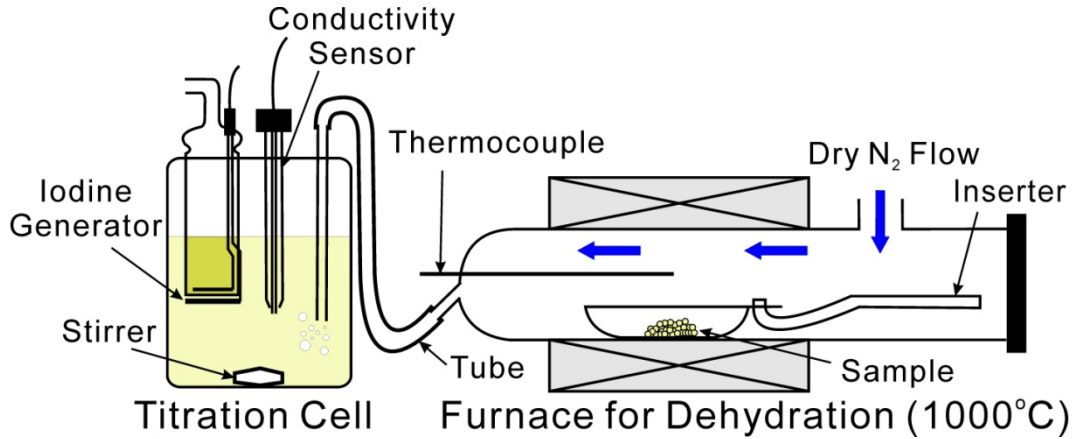
$$I_2 + H_2O + SO_2 + 3C_3H_4N_2 + CH_3OH \rightarrow \left[C_3H_5N_2\right]SO_4CH_3 + 2\left[C_3H_5N_2\right]I \qquad (2\text{-}1)$$

$$2I^- \rightarrow I_2 + 2e^- \qquad (2\text{-}2)$$

Figure 2.1 Schematic of Karl-Fischer Moisture Titrator for measuring the water content of the samples.

2.3 Methodology

The method adopted in this work for verifying whether the dopant cation occupies both the A and B-sites is first reported by Tsur et al. [01Tsu]. In this work, some refinements in theoretical consideration have been made.

When the dopant cations are amphoteric, the equilibrium constants of the reactions of their incorporation into A and B-sites, as given in Eq. (1-4) and (1-2), can be written as Eq. (2-3) and (2-4), respectively.

$$K_{\text{A-Occupation}} = \frac{a_{\text{BaO}}^2 \; a_{\text{M}_{\text{Ba}}^\bullet}^2 \; a_{\text{O}_\text{O}^\times}}{a_{\text{Ba}_{\text{Ba}}^\times}^2 \; a_{\text{M}_2\text{O}_3} \; a_{\text{V}_\text{O}^{\bullet\bullet}}} \tag{2-3}$$

$$K_{\text{B-Occupation}} = \frac{a_{\text{ZrO}_2}^2 \; a_{\text{M}_{\text{Zr}}^{'}}^2 \; a_{\text{V}_\text{O}^{\bullet\bullet}}}{a_{\text{Zr}_{\text{Zr}}^\times}^2 \; a_{\text{M}_2\text{O}_3} \; a_{\text{O}_\text{O}^\times}} \tag{2-4}$$

The Schottky reactions in A and B-sites of BaZrO$_3$ and their equilibrium constants can be expressed as Eq. (2-5), (2-7) and Eq. (2-6), (2-8), respectively. Although the formation of intrinsic Schottky disorder in the BaZrO$_3$ system is considered to be difficult due to high formation energy [10Sto], the variants of activity of $V_{\text{Ba}}^{''}$ and $V_{\text{Zr}}^{''''}$ ($a_{V_{\text{Zr}}^{''}}$ and $a_{V_{\text{Zr}}^{''''}}$) can be thermodynamically treated.

Schottky reaction in A-site:

$$Ba_{Ba}^{\times} + O_O^{\times} \rightarrow V_{Ba}^{''} + V_O^{\bullet\bullet} + BaO \tag{2-5}$$

$$K_{\text{A-Schottky}} = \frac{a_{V_{Ba}^{''}} \, a_{V_O^{\bullet\bullet}} \, a_{BaO}}{a_{Ba_{Ba}^{\times}} \, a_{O_O^{\times}}} \tag{2-6}$$

Schottky reaction in B-site:

$$Zr_{Zr}^{\times} + 2O_O^{\times} \rightarrow V_{Zr}^{''''} + 2V_O^{\bullet\bullet} + ZrO_2 \tag{2-7}$$
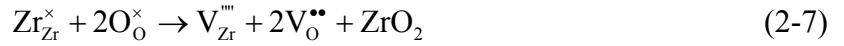
$$K_{\text{B-schottky}} = \frac{a_{V_{Zr}^{''''}} \, a_{V_O^{\bullet\bullet}}^2 \, a_{ZrO_2}}{a_{Zr_{Zr}^{\times}} \, a_{O_O^{\times}}^2} \tag{2-8}$$

By combining Eq. (2-3) and (2-6) to cancel the activity of BaO (a_{BaO}), it gives:

$$\frac{K_{\text{A-Occupation}}}{K_{\text{A-Schottky}}^2} = \frac{a_{M_{Ba}^{\bullet}}^2 \, a_{O_O^{\times}}^3}{a_{M_2O_3} \, a_{V_{Ba}^{''}}^2 \, a_{V_O^{\bullet\bullet}}^3} \tag{2-9}$$

And by combining Eq. (2-4) and (2-8) to cancel the activity of ZrO₂ (a_{ZrO_2}), it gives:

$$\frac{K_{\text{B-Occupation}}}{K_{\text{B-Schottky}}^2} = \frac{a_{M_{Zr}^{'}}^2 \, a_{O_O^{\times}}^3}{a_{M_2O_3} \, a_{V_{Zr}^{''''}}^2 \, a_{V_O^{\bullet\bullet}}^3} \tag{2-10}$$

Therefore, Eq. (2-11) can be achieved by combining Eq. (2-9) and (2-10) to cancel the activity of M₂O₃ ($a_{M_2O_3}$).

$$\frac{a_{M_{Ba}^{\bullet}}}{a_{M_{Zr}^{'}}} = \left(\sqrt{\frac{K_{\text{A-Occupation}}}{K_{\text{B-Occupation}}}} \frac{K_{\text{B-Schottky}}}{K_{\text{A-Schottky}}} \right) \frac{a_{V_{Ba}^{''}}}{a_{V_{Zr}^{''''}}} \tag{2-11}$$

Since activity is a product of concentration and activity coefficient, Eq. (2-11) can also be expressed in the form of Eq. (2-12), where γ and brackets represent the activity coefficient and the concentration of the specified defect, respectively.

$$\frac{\gamma_{M_{Ba}^{\bullet}} [M_{Ba}^{\bullet}]}{\gamma_{M_{Zr}^{'}} [M_{Zr}^{'}]} = \left(\sqrt{\frac{K_{\text{A-Occupation}}}{K_{\text{B-Occupation}}}} \frac{K_{\text{B-Schottky}}}{K_{\text{A-Schottky}}} \right) \frac{\gamma_{V_{Ba}^{''}} [V_{Ba}^{''}]}{\gamma_{V_{Zr}^{''''}} [V_{Zr}^{''''}]} \tag{2-12}$$

Therefore, if all the activity coefficients are treated as constants due to diluted species,

an important proportional relationship as given in Eq. (2-13) can be achieved between the concentration ratio of the dopant cations occupying Ba-site to that of Zr-site, and the concentration ratio of the vacancies existing in Ba-site to that in Zr-site.

$$\frac{[M_{Ba}^{\bullet}]}{[M_{Zr}^{'}]} \propto \frac{[V_{Ba}^{''}]}{[V_{Zr}^{''''}]} \tag{2-13}$$

Kuwabara et al. reported that by using first principle calculation to evaluate the defect equilibrium in $BaZrO_3$ at $1627^{\circ}C$ (1700 K), which is close to the sintering temperature of $1600^{\circ}C$ in our work, the difference in formation energy between $V_{Zr}^{''''}$ and $V_{Ba}^{''}$ is smaller for a Ba-rich sample than for a Ba-poor sample for the system satisfying the electroneutrality condition [10Ku1, 10Ku2], inferring that comparing to the Ba-rich sample, the concentration ratio of the $V_{Ba}^{''}$ to $V_{Zr}^{''''}$ is higher in the Ba-poor sample, as given in Eq. (2-14). And if the sample is slightly doped, it is reasonable to consider that such relationship still works.

$$\left(\frac{[V_{Ba}^{''}]}{[V_{Zr}^{''''}]}\right)_{Ba-rich} < \left(\frac{[V_{Ba}^{''}]}{[V_{Zr}^{''''}]}\right)_{Ba-poor} \tag{2-14}$$

By comparing Eq. (2-13) and (2-14), it gives:

$$\left(\frac{[M_{Ba}^{\bullet}]}{[M_{Zr}^{'}]}\right)_{Ba-rich} < \left(\frac{[M_{Ba}^{\bullet}]}{[M_{Zr}^{'}]}\right)_{Ba-poor} \tag{2-15}$$

It means that if the dopant cation is amphoteric and its concentration in the sample is kept constant, compared with the Ba-rich sample, the concentration of the dopant cations occupying A-site will be higher, while the concentration of the dopant cations occupying B-site will be lower in the Ba-poor sample. In experiment, the difference in occupation of dopant cations in A and B-sites for Ba-rich and Ba-poor samples is supposed to be qualitatively evaluable from the lattice volumes of the samples.

2.4 Results and Discussion

2.4.1 Confirmation of B-site Occupation of Dopants

The lattice volumes of the samples of $BaZr_{1-y}M_yO_{3-\delta}$ (M = Sc, Y, Sm, Eu, Dy) with the dopant concentration varying from $y = 0$ to 0.03 are shown in Figure 2.2.   It can be observed that when doped with Y, Dy, Eu or Sm, the lattice volumes of the samples increased with the increasing dopant concentration.   Meanwhile, no obvious change in the lattice volumes was observed for the samples doped with Sc.
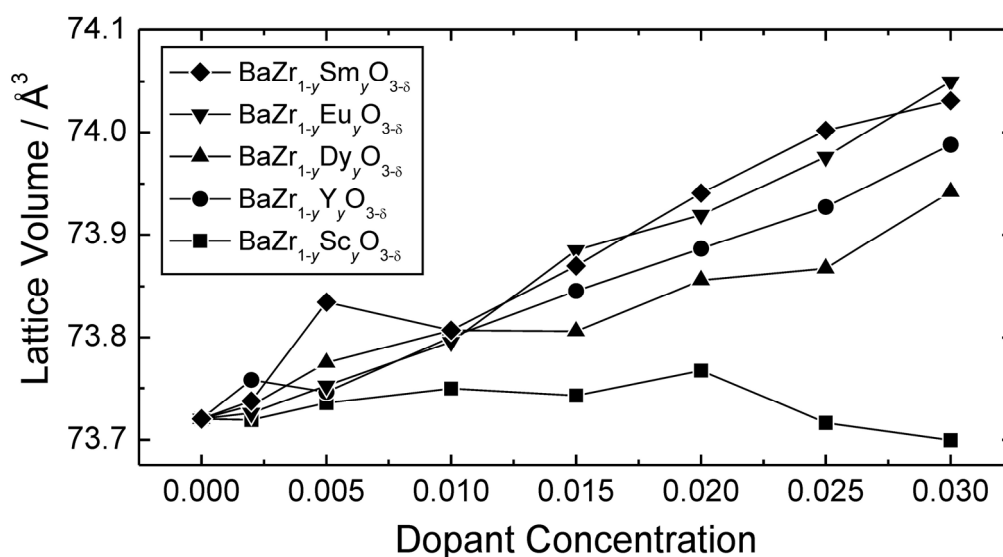
Figure 2.2 Lattice volumes of the samples of $BaZr_{1-y}M_yO_{3-\delta}$ (M = Sc, Y, Sm, Eu, Dy) with the dopant concentration increasing from y = 0 to 0.03.   The samples were sintered at 1600°C for 24 h in O_2 flow.

According to Vegard's Law, replacing lattice cations by larger ones will induce an expansion in lattice volume.   Since the six-fold coordinated radii of the cations of Y(III) (0.900 Å), Dy(III) (0.912 Å), Eu(III) (0.947 Å) and Sm(III) (0.958 Å) are larger than that of the Zr(IV) cation (0.72 Å) [76Sha], and the reported radius of twelve-fold coordinated Sm(III) cation (1.24 Å [76Sha]), also the radius obtained by extrapolation [09Par] of the cations of Y(III) (1.251 Å), Dy(III) (1.255 Å) and Eu(III) (1.295 Å) are smaller than that of Ba(II) (1.61 [76Sha]), the expanding of the lattice volume with the increasing dopant concentration is considered to

be attributed to the B-site occupation of significantly large amount of dopant cations. While for doping of Sc, since the six-fold coordinated radius of the Sc(III) cation (0.745 Å [76Sha]) is close to that of the Zr(IV) cation, substituting the Zr(IV) cations with the Sc(III) cations does not induce obvious change in the lattice volume. Therefore, it is rather difficult to judge whether Sc occupies A or B-site from Figure 2.2, although Sc is generally recognized to be of B-site occupation.

2.4.2 Investigation of Possibility of A-site Occupation of Dopants

The conclusion can be drawn from the analysis in 2.4.1 that a significantly large amount of Y(III), Sm(III), Eu(III) and Dy(III) cations occupy B-site when they are doped into $BaZrO_3$, but it cannot be treated as equal to that these cations occupy B-site solely. Even though the dopant cations partially occupy A-site of $BaZrO_3$, if their amount in A-site is relatively less than that in B-site, a combined effect leading to the expansion of lattice volume will be expressed eventually. For example, although an increase of lattice volume with the increasing dopant concentration of Y was shown in Figure 2.2 clearly, some phenomena of the possible A-site occupation of Y(III) cations were already reported as well [08Aza, 10Yam].

In order to apply the method explained in 2.3, Ba-poor (nominal concentration of Ba: 0.99), Ba-rich (nominal concentration of Ba: 1.01) and stoichiometric (nominal concentration of Ba: 1.00) samples with the dopant concentration of 0.01 were prepared. The lattice volumes of these samples are summarized in Figure 2.3. The lattice volume differences, which are defined as the lattice volumes of the Ba-rich samples minus those of the Ba-poor samples, are as shown in Figure 2.4, with the reported values of doped $BaTiO_3$ [01Tsu] for comparison. It is observed that for the samples doped with Eu and Sm, the differences between the lattice volumes of the Ba-rich and Ba-poor samples are larger than that of the undoped samples. While, for doping of Dy and Y, the values of the lattice volume

differences are close to that of the undoped one. And when doped with Sc, the value of the lattice volume difference is less than that of the undoped samples.
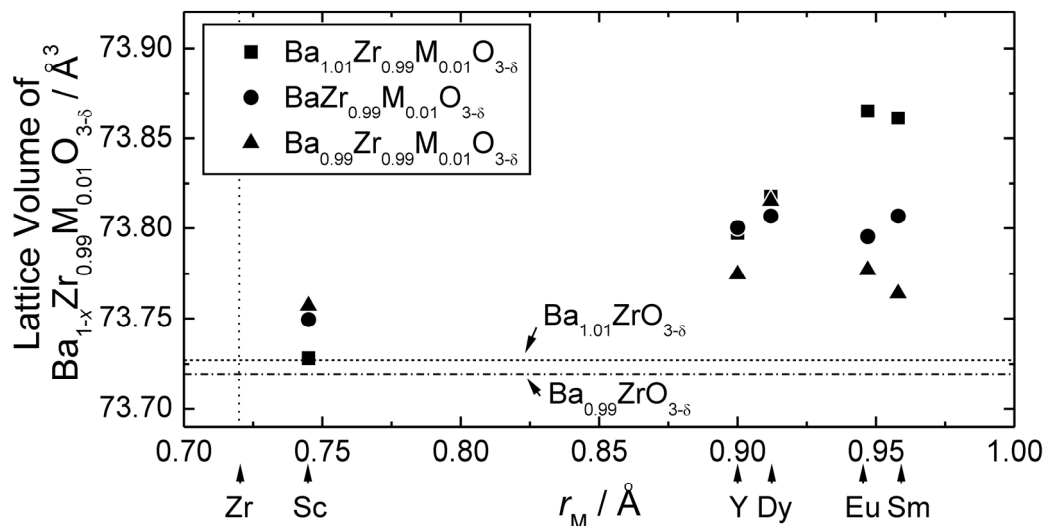

Figure 2.3 Lattice volumes of the samples of $Ba_{1.01}Zr_{0.99}M_{0.01}O_{3-\delta}$, $BaZr_{0.99}M_{0.01}O_{3-\delta}$ and $Ba_{0.99}Zr_{0.99}M_{0.01}O_{3-\delta}$ (M = Sc, Y, Sm, Eu, Dy), which were sintered at $1600^{\circ}C$ for 24 h in O_2 flow.
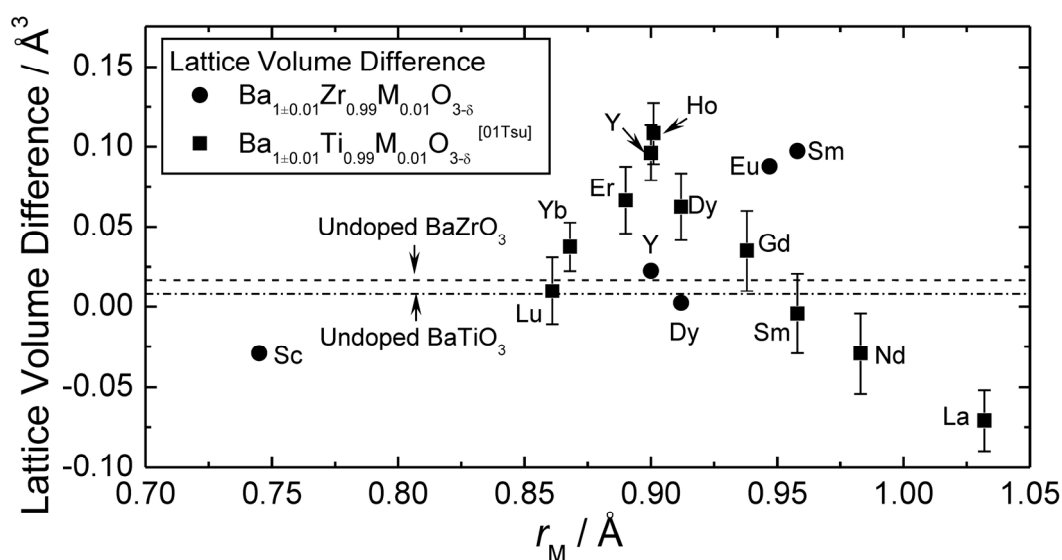
Figure 2.4 Lattice volume differences, identified as the lattice volume of the Ba-rich sample ($Ba_{1.01}Zr_{0.99}M_{0.01}O_{3-\delta}$ (M = Sc, Y, Sm, Eu, Dy)) minus that of the Ba-poor sample ($Ba_{0.99}Zr_{0.99}M_{0.01}O_{3-\delta}$ (M = Sc, Y, Sm, Eu, Dy)). The reported values of doped $BaTiO_3$ [01Tsu] are plotted for comparison. The doped $BaZrO_3$ samples were all sintered at $1600^{\circ}C$ for 24 h in O_2 flow.

In respect of the undoped samples, their lattice volumes can be regarded to mainly depend on the concentrations of vacancies in various sites. However, the variation of the lattice volume of doped samples is a combination of the effects not only induced from vacancies, but also the occupation of dopant cations in different sites. In order to evaluate the influence of the vacancies on the lattice volume, a series of the undoped samples with intentionally introduced deficiency of Ba were prepared, with the lattice volumes of the perovskite-type phases summarized in Figure 2.5. The circles indicate that a single phase was obtained after being sintered at 1600 ^{o}C. The triangles indicate that the samples were identified to be composed of perovskite-type and zirconia phases. As confirmed in Figure 2.5, there is small fluctuation of lattice volume, suggesting that the contribution from vacancies in A-site to the lattice volume is negligible compared to the experimental error. As shown in Figure 2.4, the differences in lattice volumes of the samples doped with Eu and Sm are greatly larger than that of the undoped samples (or fluctuation of lattice volume). Therefore, in such circumstance, not only the influence of vacancies, but also that of occupation of dopant cations in different sites should be taken into account. Since the radii of Eu(III) and Sm(III) cations are larger than that of Zr(IV) cation, but smaller than that of Ba(II) cation, larger difference in lattice volume than that of undoped samples is considered to be greatly attributed to the fact that compared with other dopant cations, relatively more Eu(III) and Sm(III) cations occupy A-site in a Ba-poor sample. However, as recognized in 2.4.1, a large portion of Eu(III) and Sm(III) cations was confirmed to occupy B-site. Namely, Eu and Sm are amphoteric for doping into BaZrO$_3$.

For doping of Y and Dy, the values of the lattice volume differences are close to that of the undoped samples, indicating that the variation in Ba concentration induced no obvious change in the occupation of the dopant cations. We consider that Dy(III) and Y(III) cations mainly occupy B-site. Although Y is reported to be also a possible amphoteric dopant for

BaZrO$_3$ [08Aza, 10Yam], it is unable to confirm the corresponding phenomenon in our work. This may be related to the sensitivity of the method we adopted, or the possibility that the capability of Y occupying A-site is not comparable to that of Eu and Sm. In addition, for doping of Sc, the value of the lattice volume difference is less than that of the undoped ones. The reason for this phenomenon is not clear at present.
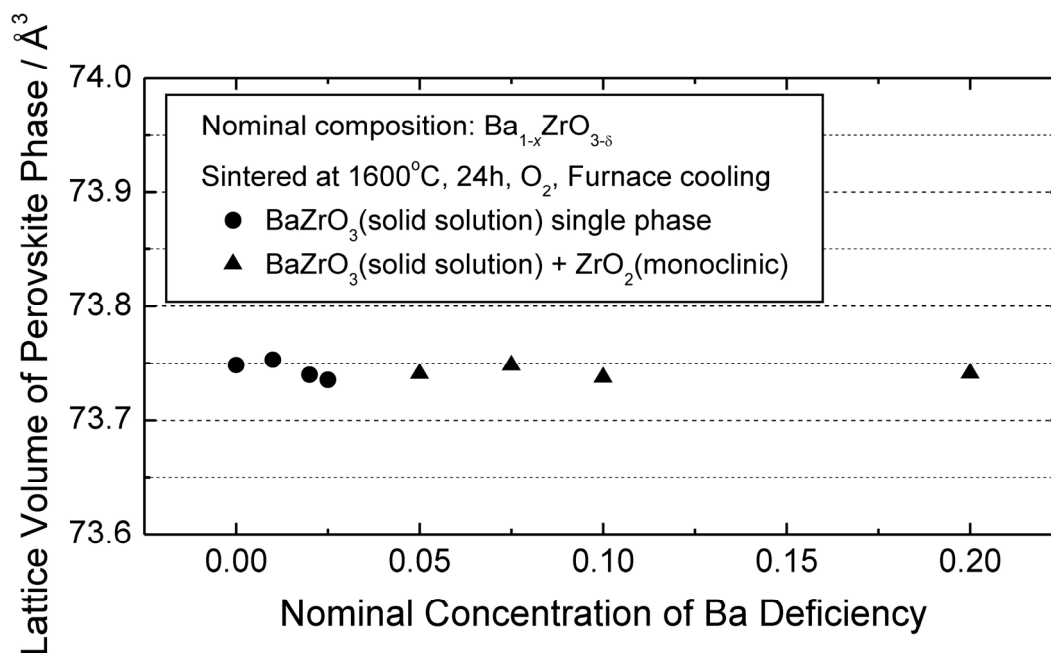

Figure 2.5 Lattice volume of the perovskite phase in the samples with the nominal composition of Ba$_{1-x}$ZrO$_{3-\delta}$ (x = 0, 0.01, 0.02, 0.025, 0.05, 0.075, 0.1 and 0.2). All the samples were sintered at 1600°C for 24h in O$_2$ flow.

Another interesting phenomenon was observed in the morphologies of the sintered pellets. As shown in Figure 2.6, for doping of Eu, the Ba-poor and stoichiometric samples exhibited fine grain size around 0.35 μm. While for the Ba-rich sample, the grains grown up obviously. Similar phenomena were also observed for the doping of the other dopants as well. In the work of Imashuku et al. [07Ima], growth of grain size in the Y-doped Ba-rich sample was also reported. Although the reason for such phenomenon is not very clear, one hypothesis is that for the Ba-rich samples, liquid phase forms during the sintering process at 1600 ^{o}C [07Ima], from which the growth of the grain may be benefitted.

(a) $Ba_{0.99}Zr_{0.99}Eu_{0.01}O_{3-\delta}$

(b) $BaZr_{0.99}Eu_{0.01}O_{3-\delta}$
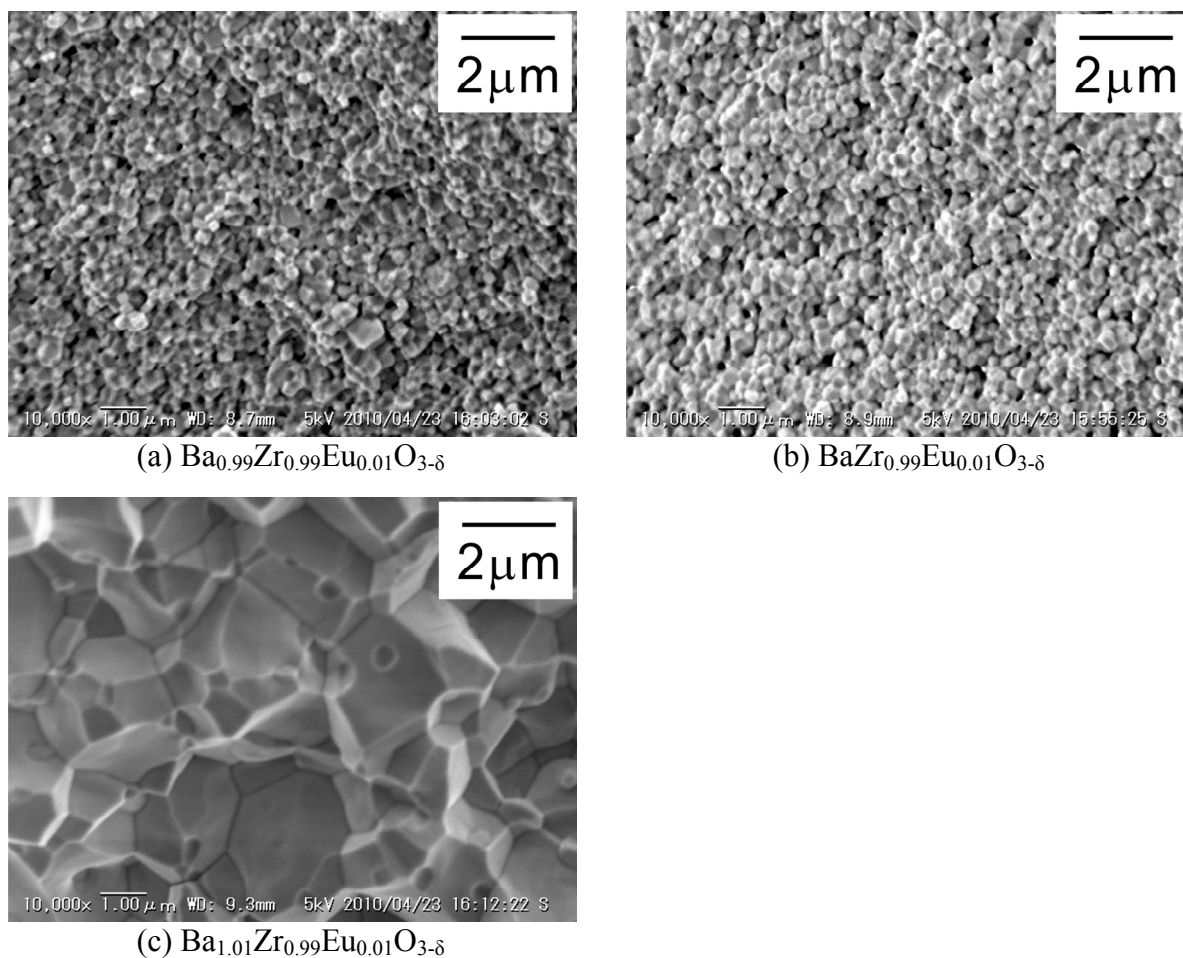

(c) $Ba_{1.01}Zr_{0.99}Eu_{0.01}O_{3-\delta}$

Figure 2.6 Morphologies of cross-section of the Eu doped samples with various Ba concentrations of (a) Ba-poor, (b) stoichiometry and (c) Ba-rich. All the samples were sintered at $1600^{o}C$ for 24 h in an O_2 flow.

2.4.3 Water Content of $BaZr_{0.8}M_{0.2}O_{3-\delta}$ (M = Sc, Y, Sm, Eu, Dy)

The results of the measurement of water contents of the samples of $BaZr_{0.8}M_{0.2}O_{3-\delta}$ (M = Sc, Y, Sm, Eu, Dy) hydrated in 5% H_2O - Ar or 5% H_2O - O_2 are shown in Figure 2.7. The results revealed that when hydrated in humid O_2, the concentrations of hydroxide ions of the samples doped with Dy, Eu or Sm were much lower than those of the samples doped with Sc or Y. When hydrated in humid Ar, comparing with those hydrated in humid O_2, no significant difference was observed for the samples of $BaZr_{0.8}M_{0.2}O_{3-\delta}$ (M = Sc, Y, Sm, Eu). While for the sample of $BaZr_{0.8}Dy_{0.2}O_{3-\delta}$, a great elevation in concentration of hydroxide ions was observed when hydrated in humid Ar.

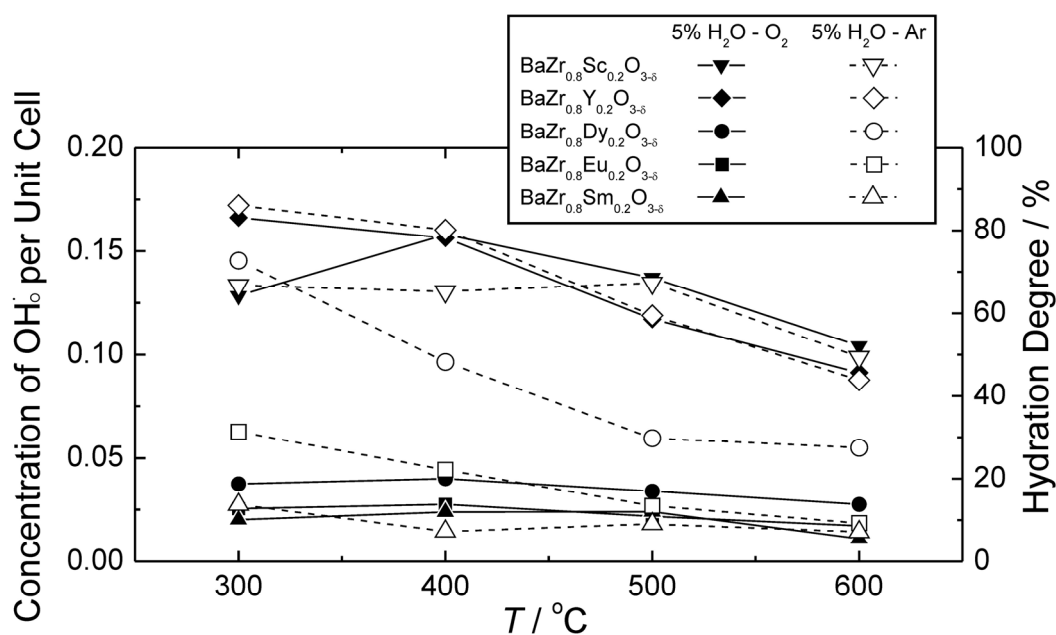**Figure 2.7** Concentrations of hydroxide ions per unit cell and hydration degree of the samples of $BaZr_{0.8}M_{0.2}O_{3-\delta}$ (M = Sc, Y, Sm, Eu, Dy) hydrated in the atmosphere of 5% H_2O- Ar or 5% H_2O - O_2.   The samples for hydration of the size about 2 mm in length, broken from the pellets sintered at 1600°C for 24 h in an O_2 flow.

One possible reason for lower water content in the Eu and Sm doped samples is considered to be attributed to the partial A-site occupation of these dopants, which reduces the oxide ion vacancies and obstructs the hydration reaction in consequence.   And it is also possible that by doping of Eu and Sm, a significant change of the material property may occur.

2.5 Conclusions

(1) With the method of comparing the lattice volumes of doped and undoped Ba-rich, and Ba-poor samples, it was confirmed that for doping Eu or Sm, not only B-site, but also A-site seemed to be occupied by the dopant cations.   Therefore, Eu and Sm are considered to be amphoteric dopants for $BaZrO_3$.

(2) For doping of Sc, Y or Dy into $BaZrO_3$, the dopant cations mainly occupied B-site.

Although some possible A-site occupation phenomena of Y were reported [08Aza, 10Yam], restricted to the sensitivity of the method applied in this work, or the significantly low concentration of Y occupying the A-site, the relevant A-site occupation phenomena was not observed with the method of this work. Further investigations are conducted in the following chapters (Chapter 3 and 4).

(3) The concentrations of hydroxide ions in the Sm and Eu doped $BaZrO_3$ were greatly lower than those in the Sc and Y doped samples, regardless whether hydrated in humid Ar or humid O_2. And the concentration of hydroxide ions in the sample of Dy doped sample hydrated in humid Ar was obviously higher than that hydrated in humid O_2.

References

[76Sha] R.D. Shannon, *Acta Crystallogr. A* 32 (1976) 751-767.

[01Tsu] Y. Tsur. A. Hitomi, I. Scrymgeour, C. Randall, *Jpn. J. Appl. Phys*. 40 (2001) 255-258.

[07Ima] S. Imashuku, T. Uda, Y. Awakura, *Electrochem. Solid St*. 10 (2007) B175-B178.

[08Aza] A.K. Azad, C. Savaniu, S. Tao, S. Duval, P. Holtappels, R.M. Ibberson, J.T.S. Irvine, *J. Mater. Chem*. 18 (2008) 3414-3418.

[09Par] K. Park, C. Kim, Y. Yoon, S. Song, Y. Kim, K. Hur, *J. Eur. Ceram. Soc.* 29 (2009) 1735-1741.

[10Sto] S.J. Stokes, M.S. Islam, *J. Mater. Chem.* 20 (2010) 6258-6264.

[10Yam] Y. Yamazaki, R, Hernandez-Sanchez, S.M. Haile, *J. Mater. Chem*. 20 (2010) 8158-8166.

[10Ku1] A. Kuwabara, C.A. Fisher, H. Moriwake, F. Oba, K. Matsunaga, I. Tanaka, *Abstracts of the 15th International Conference on Solid State Proton Conductors,* Santa Barbara, USA, 2010.

[10Ku2] A. Kuwabara, K. Toyoura, Y. Koyama, F. Oba, C.A. Fisher, H. Moriwake, K. Matsunaga, I. Tanaka, *Extended abstracts of the 36th Symposium on Solid State Ionics in Japan*, Sendai, Japan, 2010.

Chapter 3

Evaluation of Site Occupation of Y by Powder X-ray Diffraction Based on Anomalous Dispersion Effect

3.1 Introduction

According to the research until now, Y is the optimal acceptor dopant for $BaZrO_3$ to generate protonic conductivity [03Kre, 09Yam, 10Fab]. However, as described in Chapter 1, if Y plays the role as a donor dopant, namely partitioning into A-site of $BaZrO_3$, oxide ions which are essential for introducing protons are consumed, resulting in a detrimental effect for protonic conductivity. Several works have been conducted in order to clarify the site occupation of Y in $BaZrO_3$. Yamazaki *et al*. [10Yam] prepared a series of samples of $Ba_{1-x}Zr_{0.8}Y_{0.2}O_{3-\delta}$ by introducing Ba deficiency intentionally. In their work, only the cubic perovskite-type single phase was identified for the samples with the Ba-deficiency up to 0.06 by X-ray diffraction (XRD) analysis with the tube source of Cu Kα (8.04 keV). A decrease of conductivity and water content with the increasing Ba-deficiency was confirmed, which leaded to the conclusion that Y(III) cations partitioned into A-site in the Ba-deficient sample, resulting in a decrease of oxide ion vacancies which were necessary for introducing protons. However, decrease of oxide ion vacancies is not the only reason which will lower the protonic conductivity. Structure distortion and precipitation of other phases, which are attributed to the nonstoichiometric composition and probably difficult to be observed with conventional laboratory XRD, may also influence the protonic conductivity. In the work of Azad *et al*. [08Aza], diffraction pattern of $BaZr_{0.9}Y_{0.1}O_{3-\delta}$ was collected by high resolution neutron diffraction. By Rietveld refinement, they reported the sample of $BaZr_{0.9}Y_{0.1}O_{3-\delta}$ was a single phase of perovskite-type (α), or a mixture of two phases of perovskite-type (α and β), greatly depending on the preparation methods. In phase α, Y(III) cations were solely of B-site

occupation, and in phase β, a part of Y (III) cations occupied A-site. A recent work of Giannici *et al.* [11Gia] reported the collecting of diffraction pattern of Y-doped $BaZrO_3$ with synchrotron radiation with the incident energy about 31 keV (wavelength of 0.4 Å). Aided by the results of EXAFS and Raman spectroscopy, they found that for the sample with stoichiometric composition, no evidence of A-site occupation of Y(III) cations was observed. Their work showed the advantage of high-brightness monochromatic X-ray in structure analysis. And in this work, we utilized synchrotron radiation to collect the diffraction patterns of Y-doped $BaZrO_3$ with the incident energy close to the Y K absorption edge.

3.2 Methodology

Intensity (I_{hkl}) of (hkl) reflection can be expressed as Eq. (3-1), where F_{hkl}, p ,and LP represent structure factor, multiplicity, and Lorentz polarization factor, respectively.

$$I_{hkl} = \mid F_{hkl} \mid^2 \times p \times LP \tag{3-1}$$

In addition, the definition of structure factor F_{hkl} is given in Eq. (3-2), where x_j, y_j, z_j are coordinates of position j in a unit cell, and f_j is scattering factor of ions occupying the position j. i is the imaginary unit.

$$F_{hkl} = \sum_j f_j \exp[-2\pi i(h \times x_j + k \times y_j + l \times z_j)] \tag{3-2}$$

The perovskite-type structure factor can be shortened as Eq. (3-3) - (3-6), depending on the parity of the sum of Miller indices as ($h + k + l$).

For the case that ($h + k + l$) is even,

$$\text{If } h, k, l \text{ are all even, } \quad F_{hkl} = (f_A + f_B) + 3f_O \tag{3-3}$$

$$\text{Otherwise, } \quad F_{hkl} = (f_A + f_B) - f_O \tag{3-4}$$

For the case that ($h + k + l$) is odd,

$$\text{If } h, k, l \text{ are all odd, } \quad F_{hkl} = (f_A - f_B) - 3f_O \tag{3-5}$$

$$\text{Otherwise,} \quad F_{hkl} = (f_A - f_B) + f_O \qquad (3\text{-}6)$$

f_A, f_B, f_O are the scattering factors of cations in A and B-site, and oxide ions, respectively.

It can therefore be observed from Eq. (3-3) - (3-6) that in addition to the contribution from the oxide ions, when the sum of the Miller indices is even, the structure factor is a sum of the contributions from all the cations in A and B-sites, regardless of their occupancy in either site.   However, for the case that the sum of the Miller indices is odd, the structure factor depends on the difference in individual occupancy of the cations in A and B-sites. Thus, by comparing the structure factors of reflections with different Miller indices, the site occupancy of certain cation is determinable.   In addition, as given in Eq. (3-1), since the diffraction intensity of certain reflection is proportional to the square of the absolute value of its structure factor, the comparison of structure factors is equivalent to that of intensities. And such work can be performed by the Rietveld refinement.

The scattering factor for ion n is as given in Eq. (3-7).

$$f_n = f_{n,0}(\sin\theta/\lambda) + f'_n(E) + \mathrm{i}\,f''_n(E) \qquad (3\text{-}7)$$

As shown in Figure 3.1, although the term of $f_{n,0}(\sin\theta/\lambda)$ of Ba(II) cation is significantly larger than those of the cations of Y(III) and Zr(IV), the difference in $f_{n,0}(\sin\theta/\lambda)$ between Y(III) and Zr(IV) cations is very small due to their adjacent position in the periodic table. Referring to the term of $f'_n(E) + \mathrm{i}\,f''_n(E)$, which is named as anomalous dispersion term, as shown in Figure 3.2, if the XRD analysis is performed with the X-ray of Cu Kα (8.04 keV), the difference in either the real part or the imaginary part is still very small.   However, a dramatic drop in $f'_n(E)$ of Y occurs near the energy of Y K-edge, which is named as the anomalous dispersion effect, and the difference in $f'_n(E)$ between Y and Zr increases obviously.   Based on such phenomenon, if the X-ray with the energy near Y K-edge can be applied, the difference in scattering factor between Y(III) and Zr(IV) cations can be enlarged,
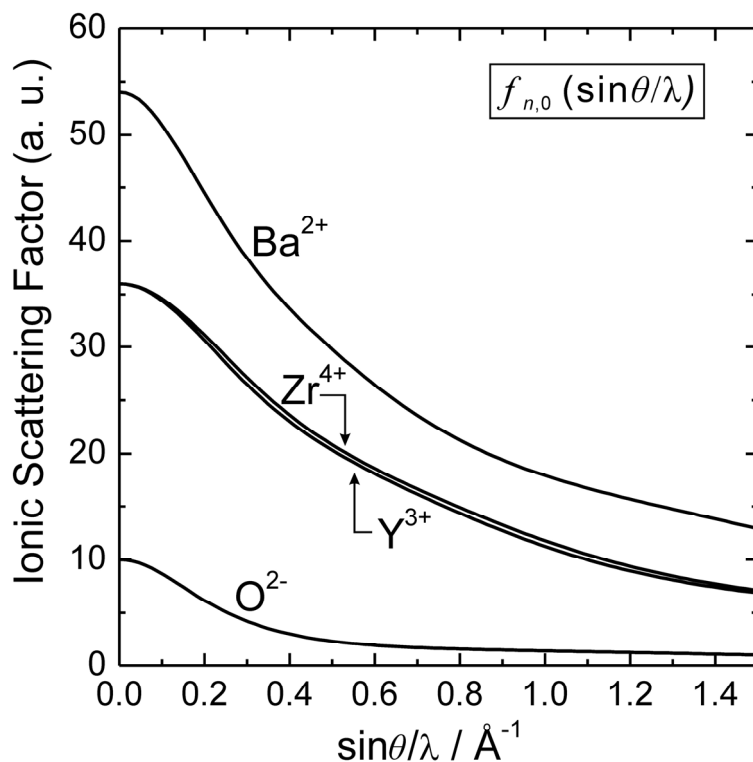
Figure 3.1 Scattering factors of $f_{n,0}(\sin\theta/\lambda)$, before taking anomalous dispersion terms into account.
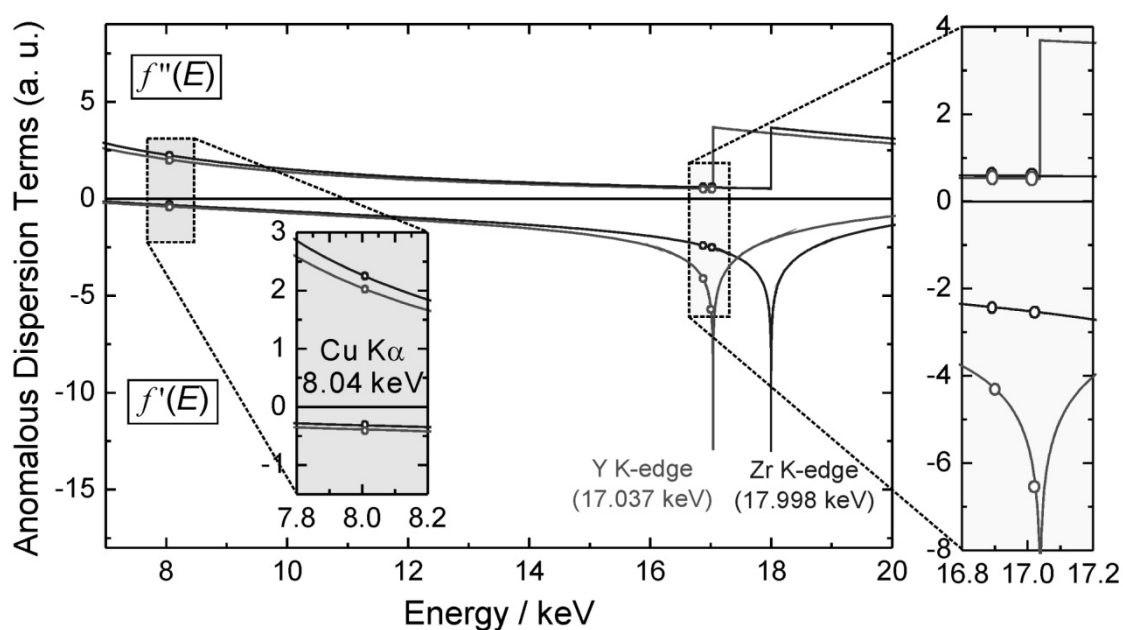

Figure 3.2 Anomalous dispersion terms of Y and Zr. Difference in either $f'(E)$ or $f''(E)$ between Y and Zr is small at incident energy of Cu Kα (8.04 keV). And dramatic drop of $f'(E)$ of Y occurs when incident energy approaches Y K-edge (17.037 keV), resulting in an increase of the difference in $f'(E)$ between Y and Zr.

by which the contributions from Y(III) and Zr(IV) cations to the structure factor is consequently separable, and site occupancy of Y(III) cations becomes determinable with better precision.

3.3 Experimental

Samples with nominal compositions of $BaZr_{0.8}Y_{0.2}O_{3-\delta}$ and $Ba_{0.9}Zr_{0.8}Y_{0.2}O_{3-\delta}$ were prepared by conventional solid state reaction method as described in Chapter 2. For sintering, two different heating processes were adopted. One process is initially heating the pellets to $1600\,^{\circ}C$ at a heating rate of $4\,^{\circ}Cmin^{-1}$ and keeping for 24 h, then furnace cooling to room temperature. After that, the pellets were heated to $1600\,^{\circ}C$, kept for 24 h again, and quenched at room temperature. The other process is inserting the pellets directly into the furnace already heated up to $1600\,^{\circ}C$. After being kept for 24 h, the pellets were quenched at room temperature. In the followings, these two processes are named as "*slow heating process*" and "*rapid heating process*", respectively.

Total compositions of the samples with the nominal compositions of $BaZr_{0.8}Y_{0.2}O_{3-\delta}$ and $Ba_{0.9}Zr_{0.8}Y_{0.2}O_{3-\delta}$ were identified to be $Ba_{0.97}Zr_{0.81}Y_{0.19}O_{3-\delta}$ and $Ba_{0.89}Zr_{0.81}Y_{0.19}O_{3-\delta}$, respectively, by inductive coupled plasma-atomic emission spectroscopy (ICP-AES, Seiko Instruments Inc., SPS4000). Microstructure was observed by SEM and a transmission electron microscope (TEM, JEOL, JEM-2100F). The TEM samples were thinned by an ion slicer (JEOL, EM-09100IS). Local composition was identified by energy dispersion X-ray spectroscopy (EDX, JEOL, JED-2300) equipped with TEM. Powder XRD analysis was performed with laboratory tube X-ray source of Cu Kα, and also at SPring-8 with the approval of the Japan Synchrotron Radiation Research Institute (JASRI) as industrial application proposal (proposal No. 2010B1850) by using the beam line of BL19B2 with the nominal X-ray energies of 16.898 keV and 17.023 keV, close to the energy of Y K-edge of

17.037 keV, and calibrated to be 16.908 keV and 17.026 keV, respectively. The samples for measurement were sealed in Lindemann glass made capillaries (Hilgenberg GmbH). Rietveld refinement was performed by a commercial software TOPAS (Bruker AXS GmbH).

3.4 Results

3.4.1 Morphology

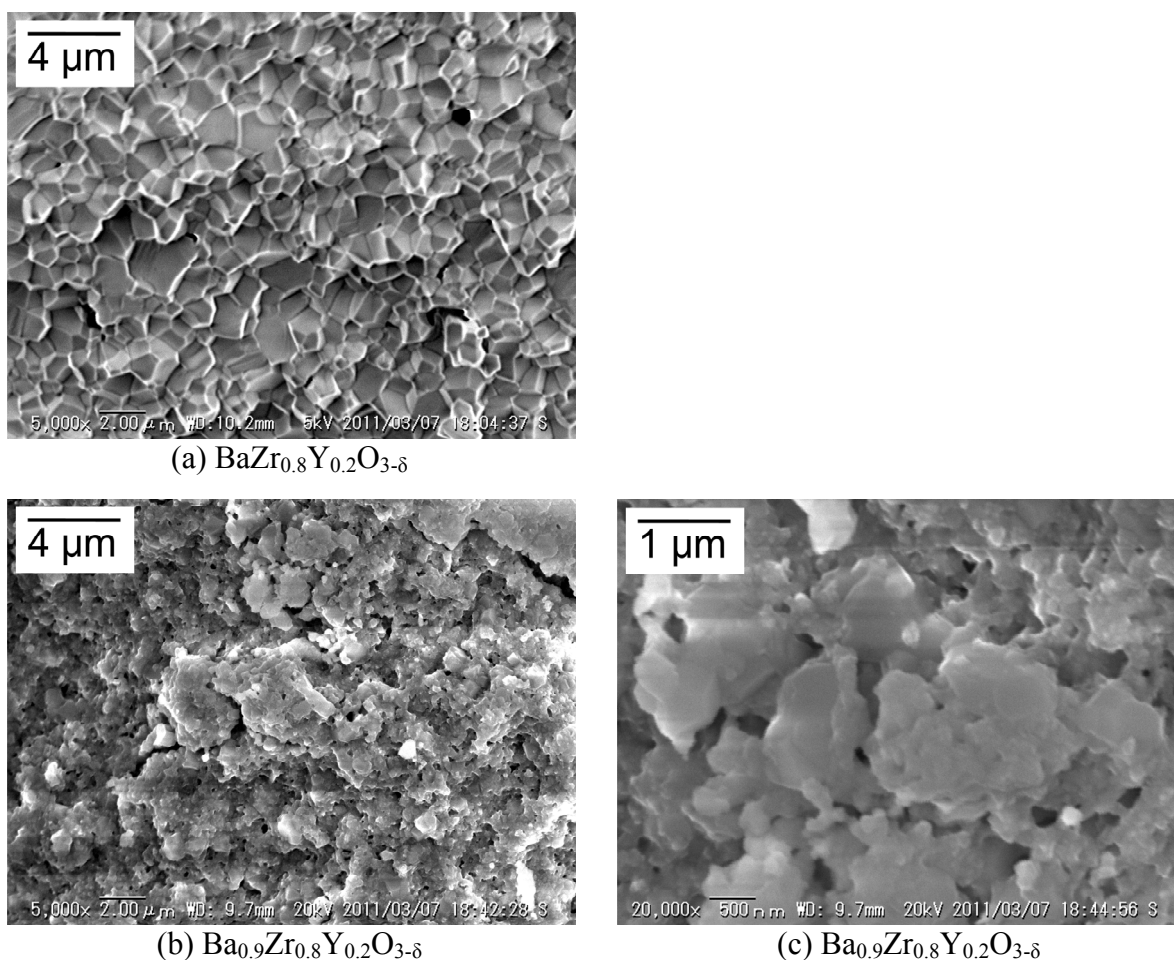Morphologies of the cross-section area of the samples prepared by slow heating process are as shown in Figure 3.3.

(a) $BaZr_{0.8}Y_{0.2}O_{3-\delta}$

(b) $Ba_{0.9}Zr_{0.8}Y_{0.2}O_{3-\delta}$

(c) $Ba_{0.9}Zr_{0.8}Y_{0.2}O_{3-\delta}$

Figure 3.3 SEM images of the cross-section of the samples of with the nominal composition of (a) $BaZr_{0.8}Y_{0.2}O_{3-\delta}$, (b) and (c) $Ba_{0.9}Zr_{0.8}Y_{0.2}O_{3-\delta}$. Both the two samples were sintered at 1600°C in an O_2 flow for 48h in total and quenched at room temperature.

For the sample with the nominal composition of $BaZr_{0.8}Y_{0.2}O_{3-\delta}$, dense morphology

with uniform grain size was obtained after being sintered at 1600 ^{o}C and subsequently quenched at room temperature.   However, the cross-section morphology of the sample with the nominal composition of $Ba_{0.9}Zr_{0.8}Y_{0.2}O_{3-\delta}$ was loose.   And a mixture of grains with two size scales can be observed from Figure 3.3(c), one is about 500 μm, and the other is relatively small, about 100 μm.

3.4.2 X-ray Diffraction

For the samples prepared by slow heating process, their diffraction patterns collected by utilizing the synchrotron radiation with the incident energy of 17.026 keV with the glancing angle (2θ) from 8.35^o to 76.48^o, and tube source X-ray of Cu Kα with the glancing angle from 17.77^o to 90.00^o are plotted as a function of ($\sin\theta/\lambda$) for comparison in Figure 3.4.   By taking the (321) reflection for example, for the case using the X-ray of Cu Kα, a peak separation of Kα1 and Kα2 was observed for both the two samples.   Meanwhile, for the patterns collected by using the synchrotron radiation, in addition to the sharp peak (peak 1), an overlapping of small peak (peak 2) can be seen apparently for $Ba_{0.9}Zr_{0.8}Y_{0.2}O_{3-\delta}$.   Such phenomenon was also confirmed for "all the peaks" at high angle region for the pattern of $Ba_{0.9}Zr_{0.8}Y_{0.2}O_{3-\delta}$, suggesting the possibility of coexistence of two perovskite-type phases.   However, such phenomenon was unable to observe from the pattern collected by X-ray source of Cu Kα, due to the interference of overlapping of Cu Kα 1 and Kα 2.   In addition, all the peaks in the pattern of $BaZr_{0.8}Y_{0.2}O_{3-\delta}$ collected by synchrotron radiation exhibited a small slope at the left side of the sharp main peak, just like the (321) reflection as shown in Figure 3.4.   And the poorly symmetric peaks were also confirmed from the pattern collected by Cu Kα.

Identified with X-ray source of Cu Kα, the (321) reflections of the samples prepared by rapid heating process are shown in Figure 3.5.   Compared with the case for $BaZr_{0.8}Y_{0.2}O_{3-\delta}$ prepared by slow heating process, an improvement of peak symmetry was observed from the

peak shape. However, due to the interference of overlapping of Cu Kα 1 and Kα 2, no conclusion can be drawn whether only one perovskite-type pattern exists.
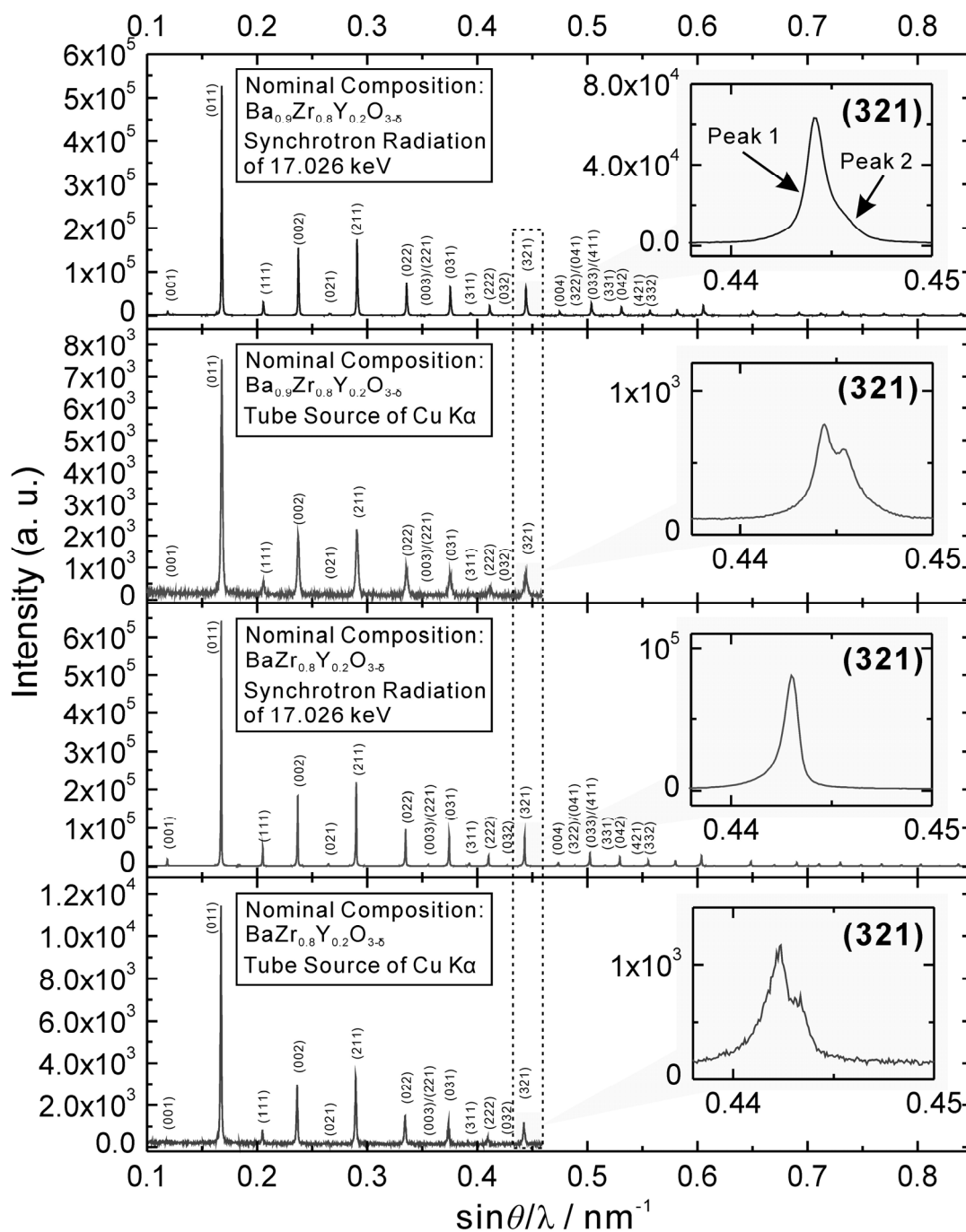

Figure 3.4 Comparison of the XRD patterns of the samples with the nominal composition of $Ba_{0.9}Zr_{0.8}Y_{0.2}O_{3-\delta}$ and $BaZr_{0.8}Y_{0.2}O_{3-\delta}$. The patterns were taken under synchrotron radiation with the X-ray energy of 17.026 keV, and conventional tube source of Cu Kα (8.04 keV).
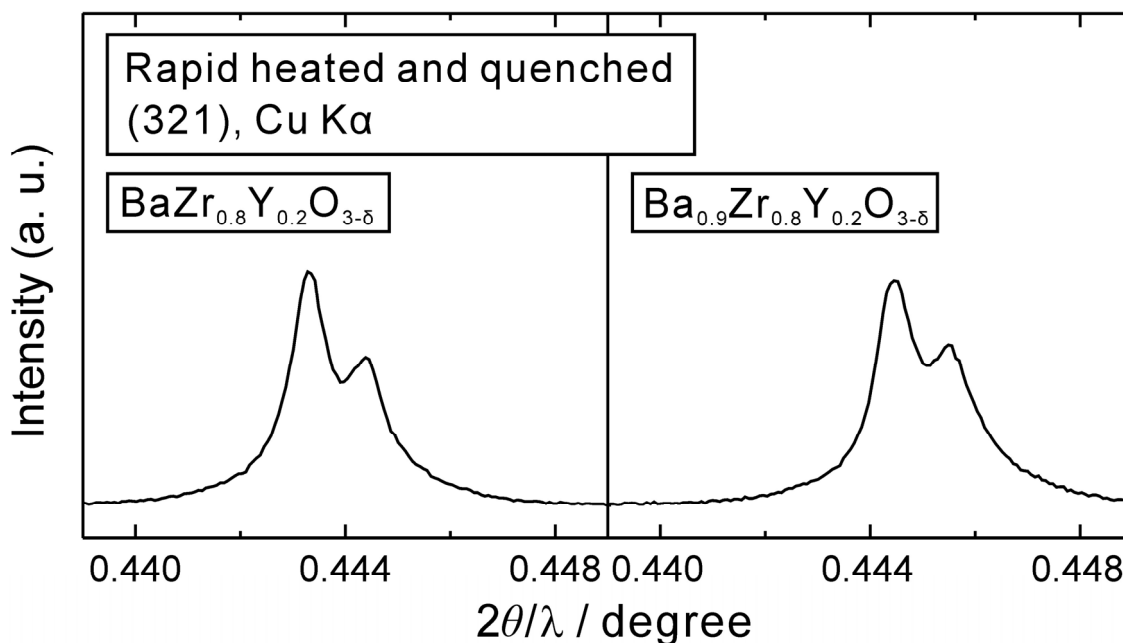
Figure 3.5 XRD pattern of (321) reflection of the sample with the nominal composition of $BaZr_{0.8}Y_{0.2}O_{3-\delta}$ and $Ba_{0.9}Zr_{0.8}Y_{0.2}O_{3-\delta}$ collected by X-ray source of Cu Kα. During the sintering process, the sample was inserted directly into the furnace already heated up to 1600 ^{o}C, and the quenched at room temperature after sintered at 1600 ^{o}C for 24 h.

3.4.3 TEM Observation

For the sample with the nominal composition of $Ba_{0.9}Zr_{0.8}Y_{0.2}O_{3-\delta}$, since phase separation was confirmed from the XRD pattern, EDX equipped with TEM was applied to identify the precise composition of each phase. The TEM samples were preliminarily sliced by a beam of argon ions (Ar^{+}), therefore, a gradual change in sample thickness formed. The schematic of the cross-section of the samples is shown in Figure 3.6. Since the electrons from the incident beam will diverge in the sample, the EDX results are expected to be dependent on the measuring position for the sample where grains with different compositions exist. For Point 1 in Figure 3.6, the electron beam strikes the grain at the thinnest part of the sample where only monolayer of grains exists. The electrons are thereby expected to diverge solely in the target grain. For Point 3, since the target grain size is large, the divergence of electrons is localized in the interior of the target grain. However, for Point 2

37

where multiple layers of grains exist and the target grain size is small, the electrons from the incident beam will probably diverge not only in the target grain, but also down to the bottom layer. Therefore, compared with Point 2, the measurements for Point 1 and Point 3 are considered to be more precisely. In this work, 36 points were measured by EDX with the results summarized in Figure 3.7. The EDX results can be divided into four groups. The symbols of open circles correspond to the compositions of large grains, as Point 3 in Figure 3.6, with the average composition of $Ba_{0.74}Zr_{0.55}Y_{0.45}O_{3-\delta}$, greatly Y-rich and Ba-deficient. The open triangles mean the compositions of small grains, as Point 1, with the average composition of $Ba_{0.87}Zr_{0.96}Y_{0.04}O_{3-\delta}$, which is Y-poor. The solid squares indicate the results of EDX performed at the position as Point 2, which are considered to be not precise significantly. In addition, two greatly Zr-rich points were detected as indicated in the TEM image of Figure 3.8, with their compositions marked as solid rhombuses in Figure 3.7. They are considered to be attributed to unreacted ZrO_2 from the starting material.
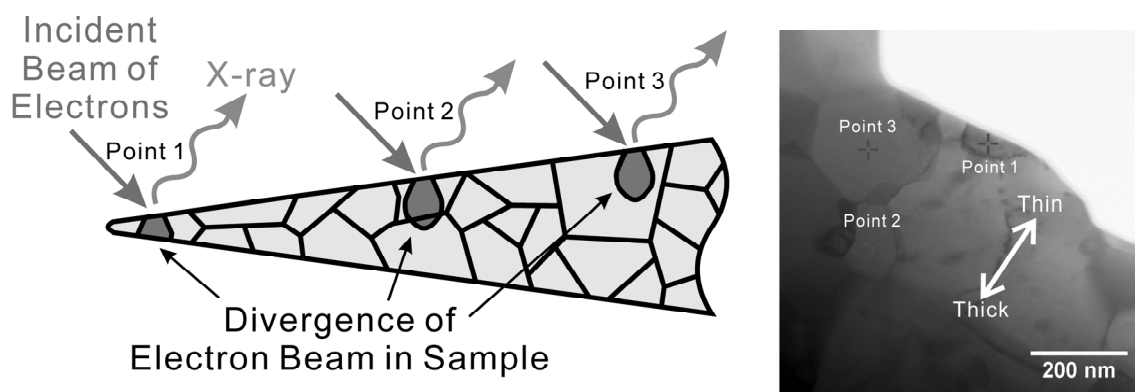

Figure 3.6 Schematic (left) of the position dependence of electron beam divergence in the sample when using EDX to determine the composition of individual grains. The positions where incident beam of electrons hit the sample, as marked as point 1 to 3 in the left schematic, correspond to the positions marked identically in the right TEM image.

Furthermore, as shown in Figure 3.9, planar defects along $(\bar{1}11)$ and $(1\bar{1}1)$ planes were observed in both the two samples. And much more periodic planar defects were confirmed for the relatively much nonstoichiometric sample of $Ba_{0.9}Zr_{0.8}Y_{0.2}O_{3-\delta}$.
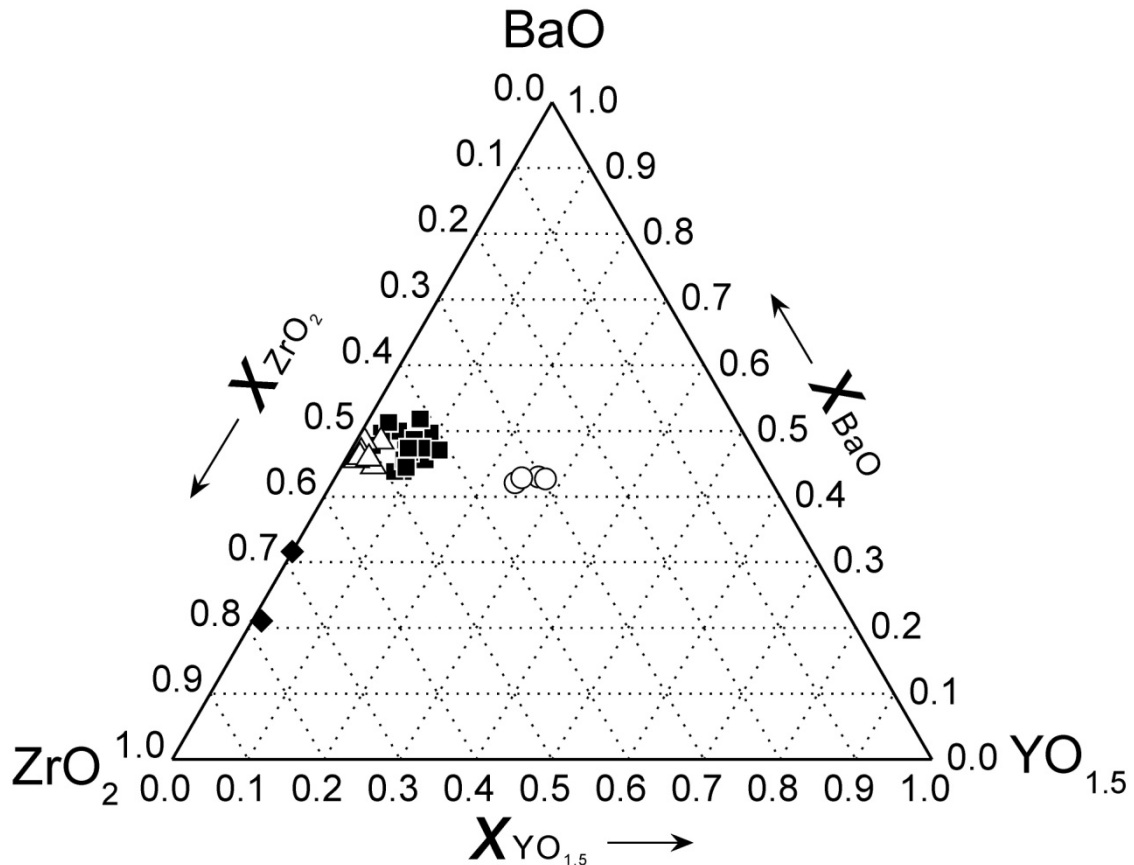
Figure 3.7 Summary of results by using EDX equipped with TEM to evaluate the grain composition in the sample with the nominal composition of $Ba_{0.9}Zr_{0.8}Y_{0.2}O_{3-\delta}$.

3.4.4 Rietveld Refinement

For the sample with the nominal composition of $BaZr_{0.8}Y_{0.2}O_{3-\delta}$ prepared by slow heating process, the composition identified by ICP-AES of $Ba_{0.97}Zr_{0.81}Y_{0.19}O_{3-\delta}$ was used for Rietveld refinement. Several constraints were established for precise refinement. The concentration of the cations and vacancies in both the A and B-sites must satisfy the site restrictions, as given in Eq. (3-8) and (3-9).

$$\text{A-site restriction:} \quad [Ba_{Ba}^{\times}] + [Y_{Ba}^{\bullet}] + [V_{Ba}^{''}] = 1 \tag{3-8}$$

$$\text{B-site restriction:} \quad [Zr_{Zr}^{\times}] + [Y_{Zr}^{'}] + [V_{Zr}^{''''}] = 1 \tag{3-9}$$
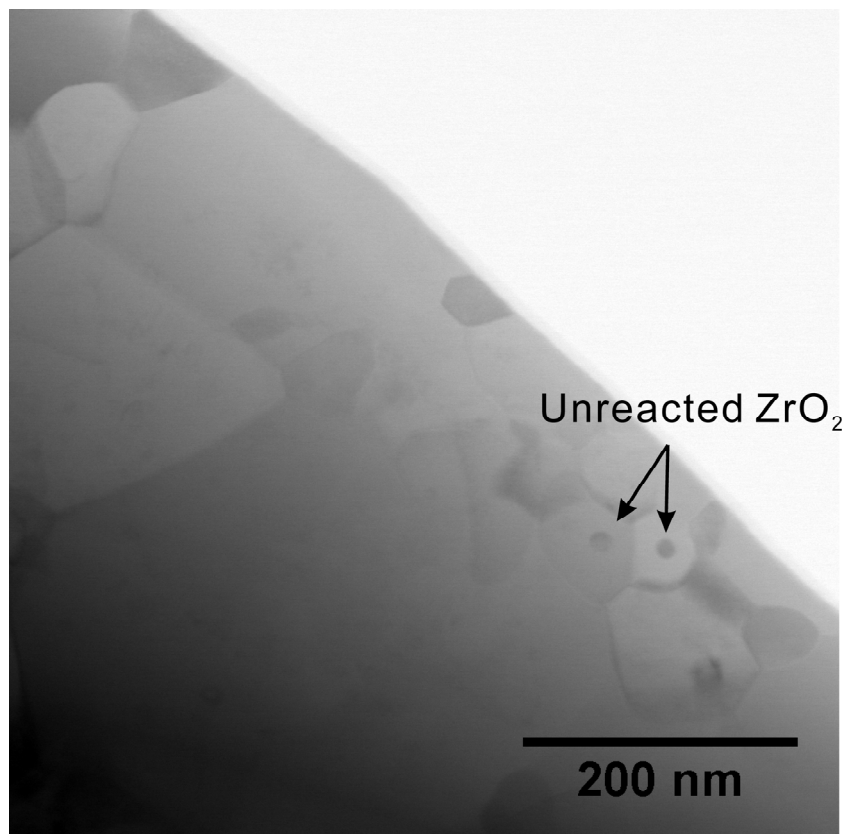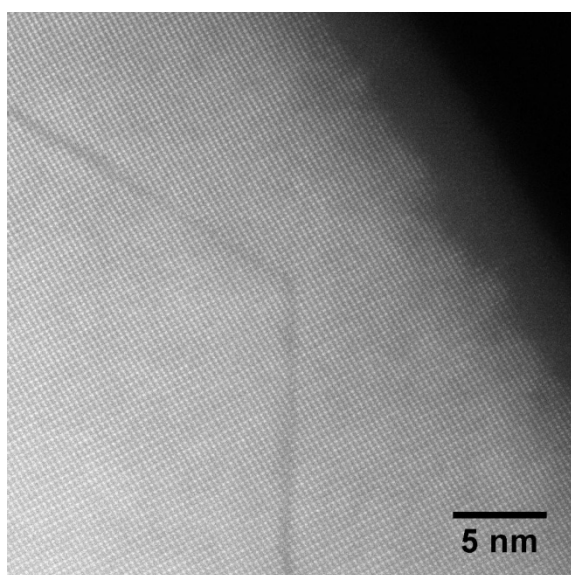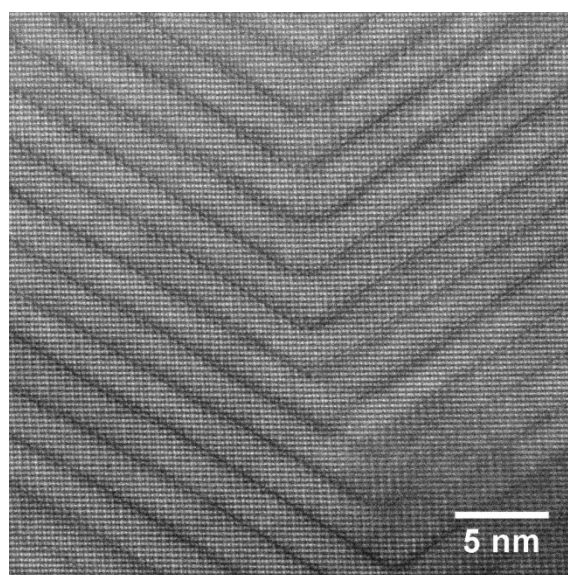
Figure 3.8 Unreacted ZrO_2 observed by TEM in the sample with the nominal composition of $Ba_{0.9}Zr_{0.8}Y_{0.2}O_{3-\delta}$.

(a) $BaZr_{0.8}Y_{0.2}O_{3-\delta}$ (b) $Ba_{0.9}Zr_{0.8}Y_{0.2}O_{3-\delta}$

Figure 3.9 Periodic planar defects observed by TEM in the samples with the nominal compositions of (a) $BaZr_{0.8}Y_{0.2}O_{3-\delta}$, and (b) $Ba_{0.9}Zr_{0.8}Y_{0.2}O_{3-\delta}$.

Compared to the formation energy of the vacancies in A-site ($V_{Ba}^{''}$), that of the vacancies in B-site ($V_{Zr}^{''''}$) is high significantly [10Sto] to treat reasonably the concentration of vacancies in B-site negligible. Therefore, Eq. (3-9) can be shortened as Eq. (3-10).

$$\text{B-site restriction:} \quad [Zr_{Zr}^{\times}] + [Y_{Zr}^{'}] = 1 \tag{3-10}$$

In addition, the relation among concentrations of all the cations should satisfy the composition relation identified by ICP-AES, as given in Eq. (3-11).

$$[Ba_{Ba}^{\times}] : [Zr_{Zr}^{\times}] : ([Y_{Ba}^{\bullet}] + [Y_{Zr}^{'}]) = 0.97 : 0.81 : 0.19 \tag{3-11}$$

By combing Eq. (3-10) and (3-11), if make the concentration of Y occupying the B-site ($[Y_{Zr}^{'}]$) as variable, the concentrations of all the cations can be expressed as the functions no $[Y_{Zr}^{'}]$, as given in Eq. (3-12) - (3-14).

$$[Ba_{Ba}^{\times}] = \frac{97 \times (1 - [Y_{Zr}^{'}])}{81} \tag{3-12}$$

$$[Zr_{Zr}^{\times}] = 1 - [Y_{Zr}^{'}] \tag{3-13}$$

$$[Y_{Ba}^{\bullet}] = \frac{19 - 100 \times [Y_{Zr}^{'}]}{81} \tag{3-14}$$

Based on these constraints, Rietveld refinement for the pattern measured with the synchrotron radiation with the incident energy of 17.026 keV was firstly performed on TOPAS, by using a cubic *pm-3m* unit cell for fitting. Fittings of reflections of (031) and (222) are shown in Figure 3.10. The factor of R_{wp} is 16.35 %, a high value, indicating poor quality of this refinement, which is attributed to the poor peak symmetry. Then, the tetragonal *p4/mbm* unit cell suggested by Giannici *et al.* [11Gia] was attempted for Rietveld refinement, as shown in Figure 3.11. However, although the lattice constants (a = 5.9732 Å, c = 4.2215 Å) obtained from the refinement of the pattern collected by incident energy of 17.026 keV are comparable to those reported by Giannici *et al.* for the 15 % Y-doped BaZrO$_3$ (a = 5.9716 Å, c = 4.2267 Å), the R_{wp} for this refinement is 17.62 %, indicating no

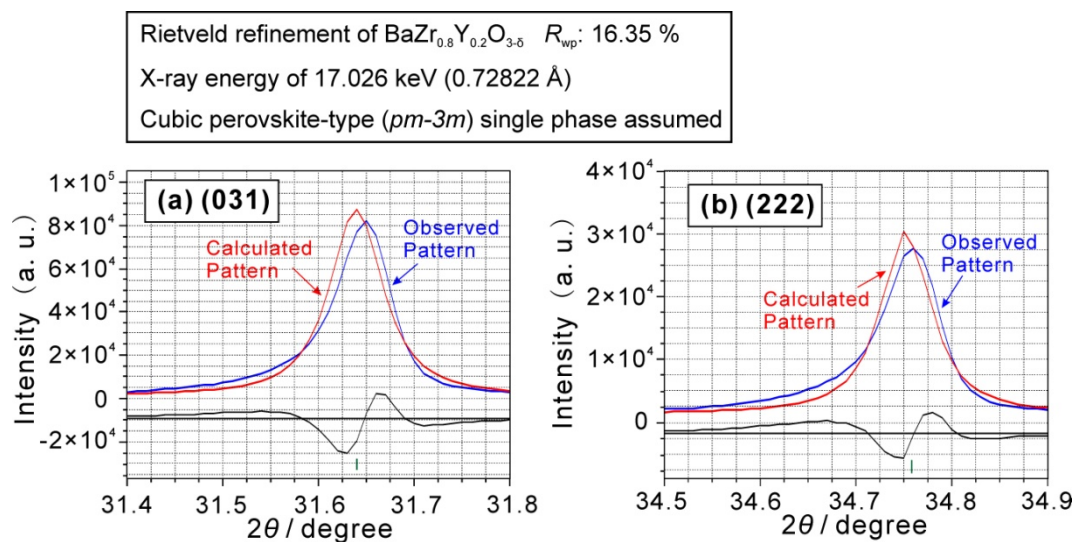**Figure 3.10** Rietveld refinement fitting of reflections of (a) (031), and (b) (222) of the sample with the nominal composition of $BaZr_{0.8}Y_{0.2}O_{3-\delta}$. The XRD pattern was collected with incident X-ray energy of 17.026 keV. Only single cubic perovskite-type (*pm-3m*) phase is assumed to exist in this refinement. Observed pattern (blue), calculated pattern (red), difference (black, at bottom) and the Bragg peaks of the candidate phases (vertical lines) are shown.
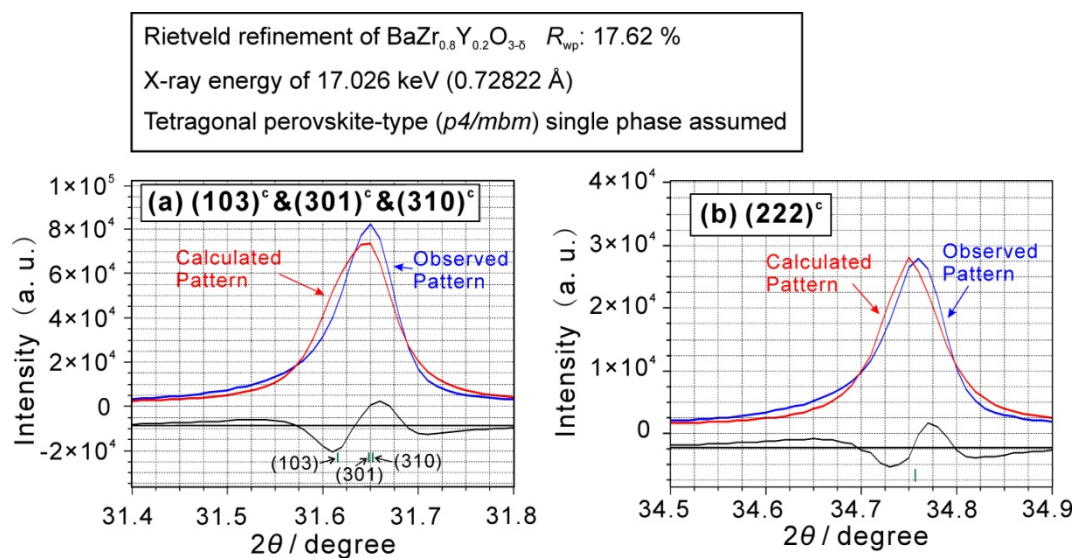

Figure 3.11 Rietveld refinement fitting of reflections of (a) $(103)^c$ & $(301)^c$ & $(310)^c$, and (b) $(222)^c$ of the sample with the nominal composition of $BaZr_{0.8}Y_{0.2}O_{3-\delta}$. The XRD pattern was collected with the incident X-ray energy of 17.026 keV. Tetragonal perovskite-type (*p4/mbm*) single phase was adopted for this refinement. Observed pattern (blue), calculated pattern (red), difference (black, at bottom) and the Bragg peaks of the candidate phases (vertical lines) are shown. $(hkl)^c$ indicates Miller indices in cubic system.

improvement in refinement quality. Especially for the (222) reflection, there is definitely no peak splitting due to different lattice constant along different orientation for tetragonal structure, such as the case for {310} reflections as shown in Figure. 3.11(a). However, as can be confirmed from Figure. 3.11(b), the peak belonging to (222) reflection is also poorly symmetric. We also considered about the possibility that this small slope appearing at the relatively low angle side of the main peak may be attributed to the reported phenomenon of relatively higher Y content near the grain boundary [08Cer, 09Igu], therefore, the lattice constant near the grain boundary is expected to be larger than that of the bulk. However, in this work, such phenomenon was not confirmed by EDX equipped with TEM. Then, we suggested that there might be a quasi-equilibrated phase whose Y content is slightly higher than the main perovskite-type phase. By comparing the relation between the lattice constant and the Y content [09Ima], the Y content in such phase is approximately 0.02 higher than that in the main phase, therefore, in addition to the main perovskite-type phase of $Ba_{0.97}Zr_{0.81}Y_{0.19}O_{3-\delta}$, another slightly Y-rich perovskite-type phase of $Ba_{0.97}Zr_{0.79}Y_{0.21}O_{3-\delta}$ was assumed here, and cubic *pm-3m* unit cell was assigned to both of the two perovskite-type phases for Rietveld refinement. The profile for the fitting is shown in Figure 3.12. R_{wp} decreased to 7.27 %, showing a good quality of refinement. The site occupancy of all the cations evaluated by the Rietveld refinement is summarized in Table 3.1, together with the results by fitting the pattern obtained from incident energy of 16.908 keV.

For the sample with the nominal composition of $Ba_{0.9}Zr_{0.8}Y_{0.2}O_{3-\delta}$, the compositions of the two perovskite-type phases identified by EDX of $Ba_{0.87}Zr_{0.96}Y_{0.04}O_{3-\delta}$ and $Ba_{0.74}Zr_{0.55}Y_{0.45}O_{3-\delta}$ were used for Rietveld refinement. In addition, the Y_2O_3 phase confirmed by diffraction pattern was also taken into account. The constraints for the relation among all the cations were established similar to that of $BaZr_{0.8}Y_{0.2}O_{3-\delta}$ as has been illustrated. The profile of Rietveld refinement is exhibited in Figure 3.13. A low value of 7.45 % was
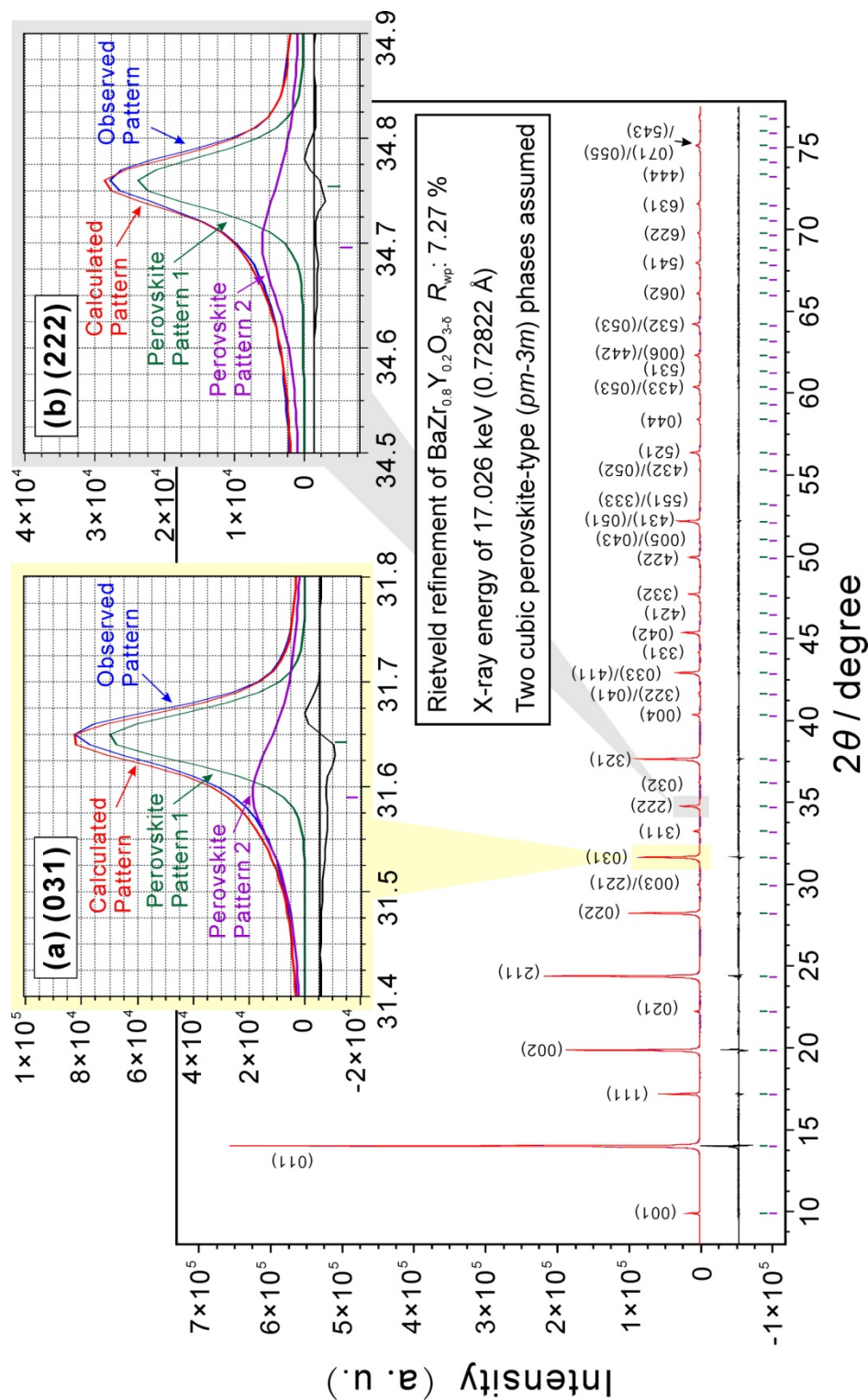
Figure 3.12 Rietveld refinement fitting of pattern of the sample with the nominal composition of $BaZr_{0.8}Y_{0.2}O_{3-\delta}$ collected with incident X-ray energy of 17.026 keV. The fittings of the reflections of (a) (031), and (b) (222) belonging to perovskite-type pattern are highlighted as insets in the top right corner. Two cubic perovskite-type (*pm-3m*) patterns are adopted for the refinement. Observed pattern (blue), calculated pattern (red), difference (black, at bottom) and the Bragg peaks of the candidate phases (vertical lines) are shown.
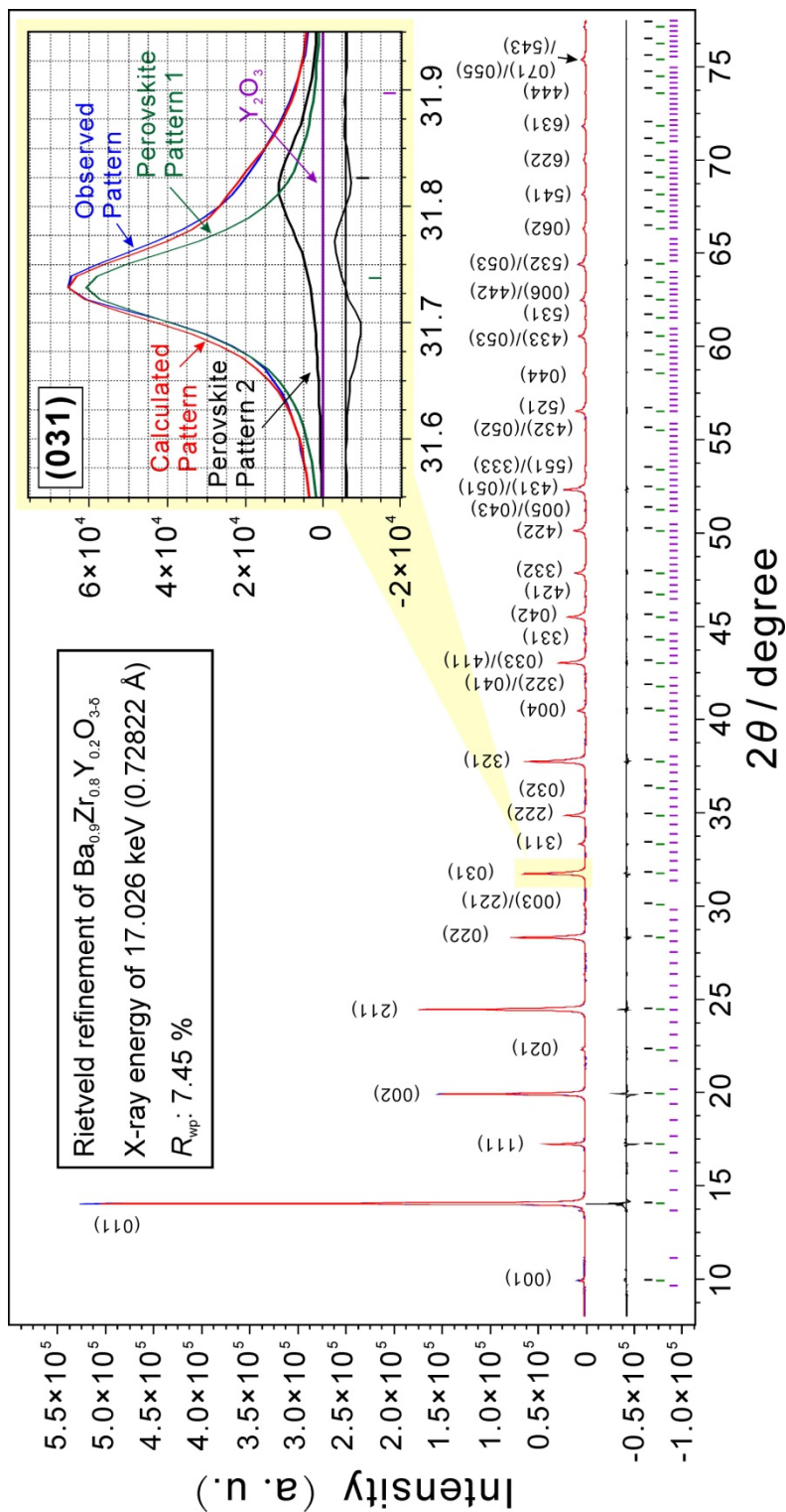
Figure 3.13 Rietveld refinement fitting of the pattern of the sample with the nominal composition of $Ba_{0.9}Zr_{0.8}Y_{0.2}O_{3-\delta}$ collected with incident X-ray energy of 17.026 keV. The fitting of (031) reflection is highlighted as an inset in the top right corner. Observed pattern (blue), calculated pattern (red), difference (black, at bottom) and the Bragg peaks of the candidate phases (vertical lines) are shown.

obtained for R_{wp}, implying a good quality of refinement.

3.5 Discussion

As summarized in Table 3.1, for the sample with the nominal composition of $BaZr_{0.8}Y_{0.2}O_{3-\delta}$, which was identified to be slightly Ba-deficient as $Ba_{0.97}Zr_{0.8}Y_{0.2}O_{3-\delta}$, all the Y(III) cations are evaluated to be of B-site occupation. For the sample with intentionally introduced Ba-deficiency of 0.1, in addition to the precipitation of Y_2O_3 solid solution, the coexistence of two perovskite-type phases was confirmed. One of the two phases was of relatively large grain size and lattice constant, with a high Y content of 0.45. A part of the Y(III) cations in this phase were evaluated to occupy A-site. The other perovskite-type phase is relatively small in both the grain size and the lattice constant, and low in the Y content. But all the Y(III) cations in this phase were evaluated to be of A-site occupation. The results obtained from utilizing the synchrotron radiation with the incident energies of 17.026 keV and 16.908 keV show good consistency. Although the total amount of doped Y was different for these perovskite-type phases, it is obvious that with the increasing Ba-deficiency, the Y content occupying A-site increased.

Although it remains unclear for the reason of the slope at the low angle side near the main peak in the sample of $BaZr_{0.8}Y_{0.2}O_{3-\delta}$ prepared by slow heating process, since the peak symmetry of the diffraction pattern of the samples prepared by rapid heating process improved, such phenomenon is possibly attributed to a kinetic reason depending on the route for sample preparation. According to the BaO - ZrO_2 - $YO_{1.5}$ pseudo-ternary phase diagram reported by Imashuku et $al.$ [10Ima], the composition of the Ba-deficient sample of $Ba_{0.89}Zr_{0.81}Y_{0.19}O_{3-\delta}$ locates in the two phase region of $BaZrO_3$ (solid solution) and ZrO_2 (cubic), indicated as solid circle in Figure 3.14, greatly different from the coexistence of Y_2O_3 and two perovskite-type phases identified in this work. While, in another estimated

pseudo-ternary phase diagram reported by Yamazaki *et al.* [10Yam], the composition of $Ba_{0.89}Zr_{0.81}Y_{0.19}O_{3-\delta}$ is in the two phase region of $BaZrO_3$ (solid solution) and Y_2O_3 (cubic), as shown in Figure 3.15.
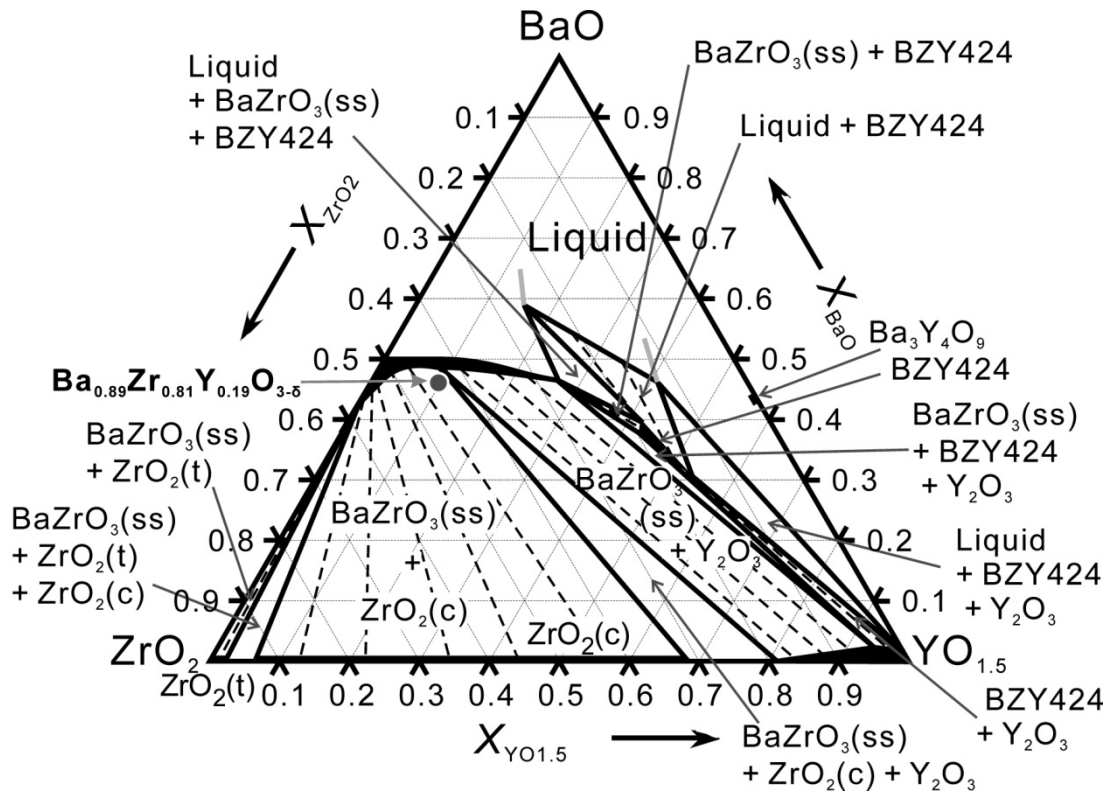

Figure 3.14 BaO - $YO_{1.5}$ - ZrO_2 pseudo-ternary phase diagram reported by Imashuku *et al.* [10Ima]   The solid circle indicates the composition of $Ba_{0.89}Zr_{0.81}Y_{0.19}O_{3-\delta}$, which is in the two phase region of $BaZrO_3$ (solid solution) and ZrO_2 (cubic).

And by comparing the preparation route, as listed in Table 3.2, the method adopted by Yamazaki *et al.* [10Yam] is similar to the slowing heating process of this work.   And the method of Imashuku *et al.* [10Ima] is the same as the rapid heating process of this work.   By combining these reported achievements with the results obtained in this work, we suggest the dependence of phase relationship on the heating process as shown in Figure. 3.16 and 3.17. For the slow heating process, phase relationship at low temperature might develop during heating to the sintering temperature of 1600 ^{o}C, since a significant difference exists in the phase diagram between 1600 ^{o}C and lower temperature [10Ima], these preliminarily formed low

temperature phases thereby will obstruct the phase equilibrium at 1600 ^{o}C in the desired time. When slowly cooled to room temperature, phase transition may also possibly occur. Contrarily, for the rapid heating process, the time for temperature changing between room temperature and sintering temperature is greatly reduced, and only the phase relationship of 1600 ^{o}C is expected to be developed.   Therefore, the phases of the samples prepared by the slow heating process are considered to be at the quasi-equilibrated status.
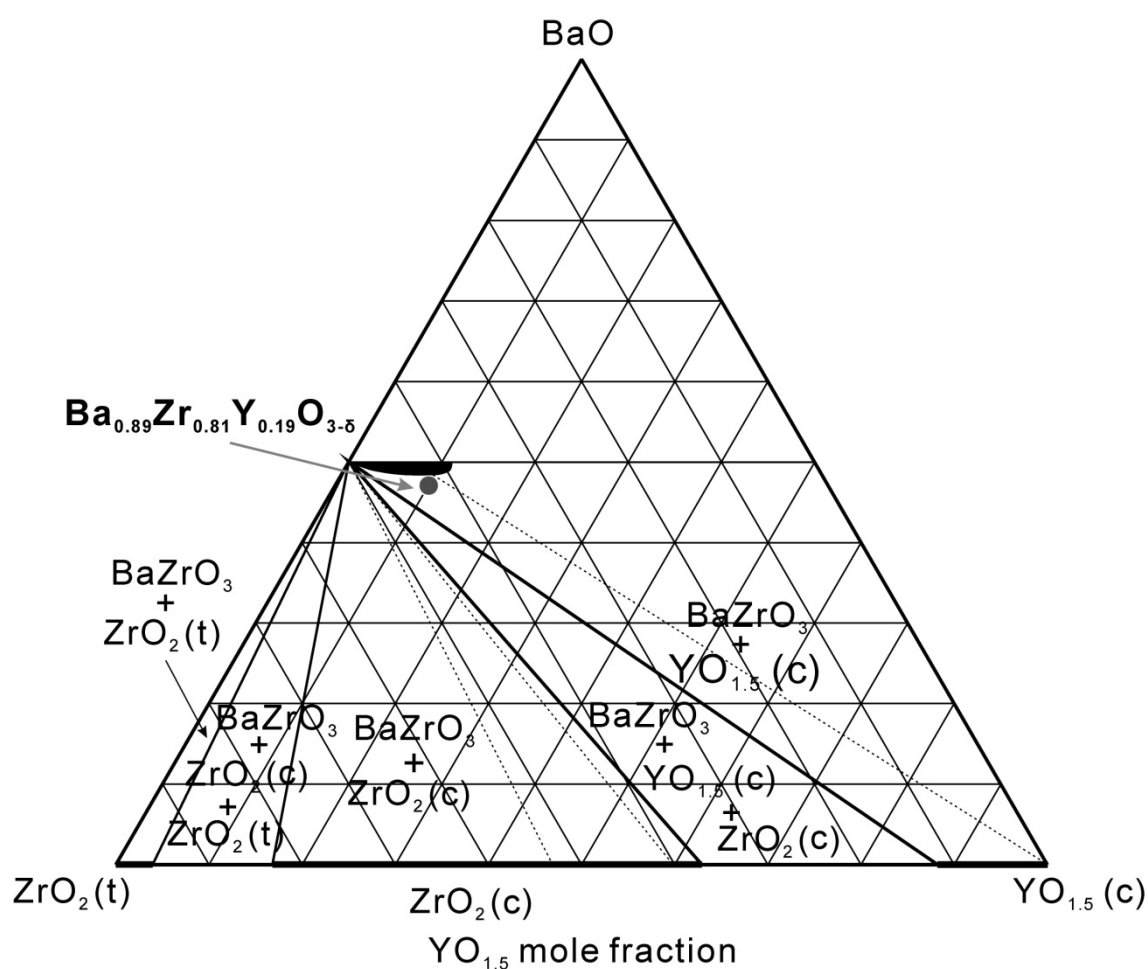

Figure 3.15 BaO - $YO_{1.5}$ - ZrO_2 pseudo-ternary phase diagram reported by Yamazaki *et al*. [10Yam]   The solid circle indicates the composition of $Ba_{0.89}Zr_{0.81}Y_{0.19}O_{3-\delta}$, which is in the two phase region of $BaZrO_3$ (solid solution) and Y_2O_3 (cubic).

The observation of periodic planar defects is also interesting.   The phase composition of $Ba_{0.74}Zr_{0.55}Y_{0.45}O_{3-\delta}$, which was identified in the sample with the nominal composition of

Table 3.1 Rietveld refinement results of $BaZr_{0.8}Y_{0.2}O_{3-\delta}$ and $Ba_{0.9}Zr_{0.8}Y_{0.2}O_{3-\delta}$ prepared by slow heating process.

Nominal Composition	X-ray Energy /keV	R_{wp}	Phase Composition	Unit Cell	Lattice Constant, a / Å	A-site Ba	A-site Y	B-site Zr	B-site Y
$BaZr_{0.8}Y_{0.2}O_{3-\delta}$	17.026	7.27 %	$Ba_{0.97}Zr_{0.81}Y_{0.19}O_{3-\delta}$	Cubic (*pm-3m*)	4.2304	0.97	0.00	0.81	0.19
			$Ba_{0.97}Zr_{0.79}Y_{0.21}O_{3-\delta}$ (assumed)	Cubic (*pm-3m*)	4.2231	0.97	0.00	0.79	0.21
	16.908	6.24 %	$Ba_{0.97}Zr_{0.81}Y_{0.19}O_{3-\delta}$	Cubic (*pm-3m*)	4.2291	0.97	0.00	0.81	0.19
			$Ba_{0.97}Zr_{0.79}Y_{0.21}O_{3-\delta}$ (assumed)	Cubic (*pm-3m*)	4.2228	0.97	0.00	0.79	0.21
$Ba_{0.9}Zr_{0.8}Y_{0.2}O_{3-\delta}$	17.026	7.45 %	$Ba_{0.87}Zr_{0.96}Y_{0.04}O_{3-\delta}$	Cubic (*pm-3m*)	4.1988	0.91	0.04	1.00	0.00
			$Ba_{0.74}Zr_{0.55}Y_{0.45}O_{3-\delta}$	Cubic (*pm-3m*)	4.2110	0.80	0.08	0.59	0.41
	16.908	6.98 %	$Ba_{0.87}Zr_{0.96}Y_{0.04}O_{3-\delta}$	Cubic (*pm-3m*)	4.1984	0.91	0.04	1.00	0.00
			$Ba_{0.74}Zr_{0.55}Y_{0.45}O_{3-\delta}$	Cubic (*pm-3m*)	4.2108	0.82	0.10	0.61	0.39

Table 3.2 Comparison of preparation methods. The samples were all sintered at 1600 ℃.

| Reporter	Synthesizing Method	Particle size / nm	Sintering Warming Method	Sintering Cooling Method	Remarks
Imashuku [10Ima]	Nitrate freeze drying	~ 30 [11Ima]	Inserting into the furnace already kept at 1600 ℃	Quenching at room temperature	
Yamazaki [10Yam]	Chemical solution route	~ 20 [09Yam]	Gradually warming up to 1600 ℃	Furnace cooling	
This work	Solid state reaction	~ 50	Gradually warming up to 1600 ℃ (4 ℃min⁻¹)	Finally Quenching at room temperature	Once furnace cooled to room temperature, and gradually warming up to 1600 ℃ again
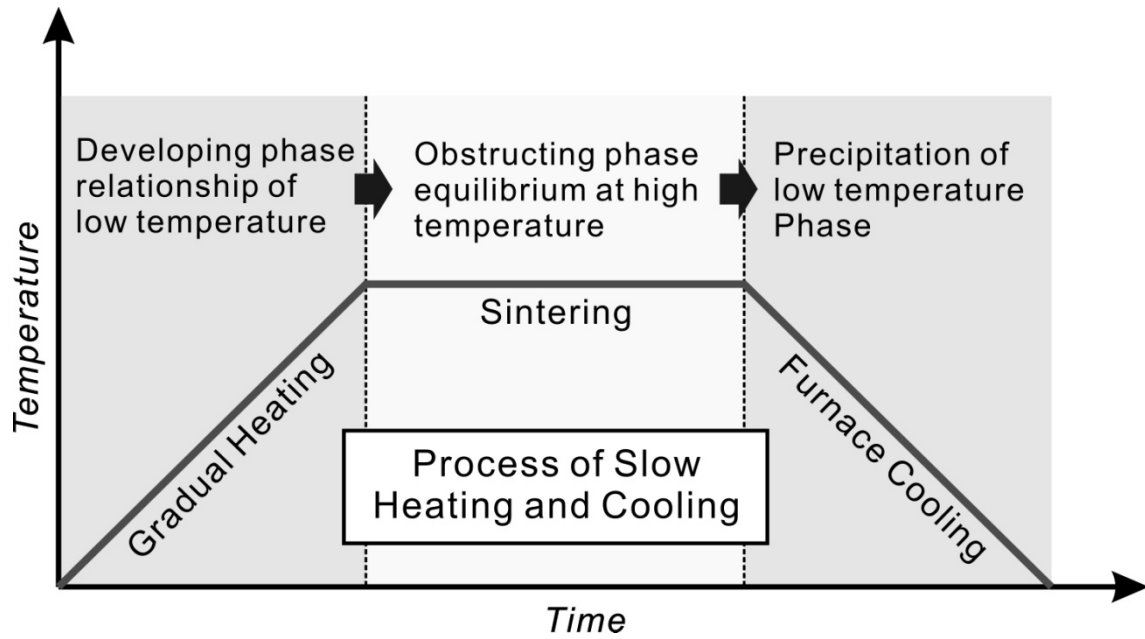
Figure 3.16 Heating profile for the process of slow heating and cooling. Samples were gradually heated up to the sintering temperature, and finally furnace cooled after being sintered.
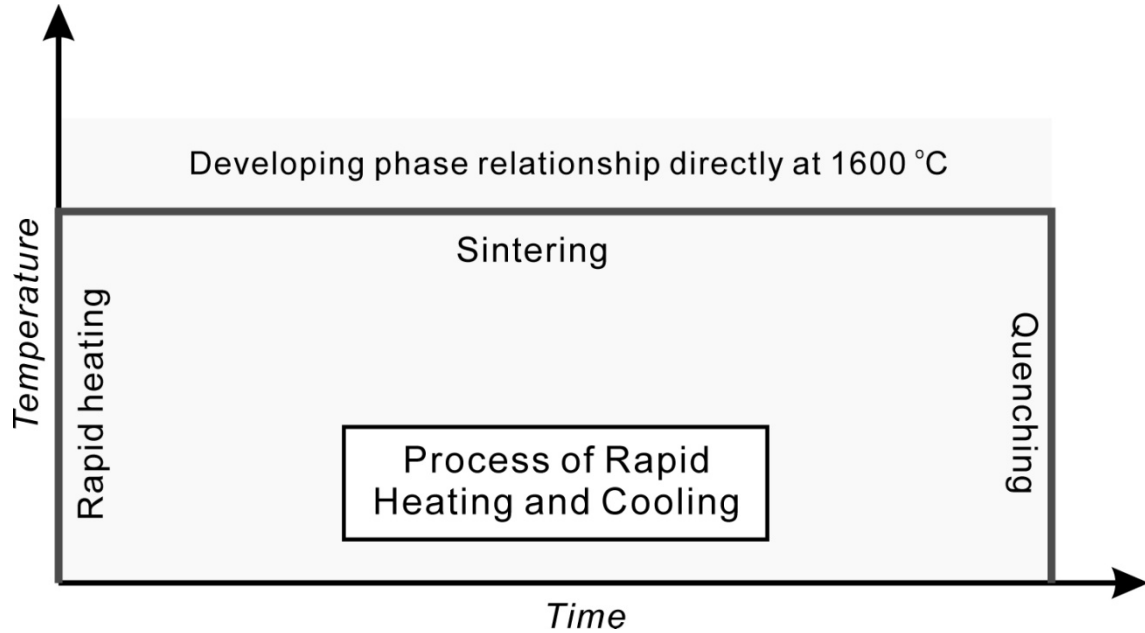
(b)

Figure 3.17 Heating profile for the process of rapid heating and cooling. Samples were directly inserted into the furnace already kept at the sintering temperature, and finally quenched to the room temperature after being sintered.

$Ba_{0.9}Zr_{0.8}Y_{0.2}O_{3-\delta}$, is greatly Ba-deficient, beyond the common knowledge for the available Ba-deficiency in $BaZrO_3$ system [10Yam]. However, since the nonstoichiometry is partially accommodated in the planar defects, the composition in the area away from the planar defects is expected not to be the value of chemical analysis by EDX equipped with TEM. The compositions used for Rietveld refinement in this work are EDX values, thus they are not very precise. However, period of these planar defects is long, and consequently does not have remarkable influence on the composition. Hence, the simulated result by Rietveld refinement is still acceptable. In addition, since these periodic planar defects divide the bulk into several discontinuous layers, it is reasonable to consider that proton conduction is probably obstructed by these defects. And the poor reproducibility of bulk conductivity for the samples even with the same composition but prepared by different preparation methods [10Fab] may possibly due to the dependence of formability of the planar defects on these preparation methods.

3.6 Conclusions

(1) Anomalous dispersion effect near Y K-edge was applied in powder X-ray diffraction for measuring the sample prepared by slowing heating process. By Rietveld refinement, it revealed that for the sample of $BaZr_{0.8}Y_{0.2}O_{3-\delta}$, which was composed of two perovskite-type phases, Y only occupied the B-site. For the sample of $Ba_{0.9}Zr_{0.8}Y_{0.2}O_{3-\delta}$, in addition to the precipitation of Y_2O_3, coexistence of two perovskite-type phases was confirmed. In one Y-poor phase, all doped Y was evaluated to be of A-site occupation. And in the other greatly Y-rich phase, in addition to B-site occupation, a partial amount of Y was estimated to occupy A-site.

(2) Dependence of phase relationship on preparation method was investigated. For the slow heating process, in which the samples were gradually heated up to the sintering temperature,

phase relationship of lower temperature is considered to be established preliminarily, obstructing the phase equilibrium at the sintering temperature in desired time. Phase transition also possibly occurred when the sample was furnace cooled to room temperature. On the contrary, during the rapid heating process, since the sample was inserted directly into the furnace already kept at the sintering temperature, and subsequently quenched to the room temperature, only the phase relationship at the sintering temperature is expected to be established.

(3) Periodic planar defects were observed in both the samples nominally stoichiometric and Ba-deficient. And the relatively larger amount of planar defects existed in the more Ba-deficient sample.   These defects probably obstruct the proton conduction.

References

[76Sha] R.D. Shannon, *Acta Crystallogr. A* 32 (1976) 751-767.

[03Kre] K.D. Kreuer, *Annu. Rev. Mater. Res*. 33 (2003) 333.

[08Aza] A.K. Azad, C. Savaniu, S. Tao, S. Duval, P. Holtappels, R.M. Ibberson, J.T.S. Irvine, *J. Mater. Chem*. 18 (2008) 3414-3418.

[08Cer] R.B. Cervera, Y. Oyama, S. Miyoshi, K. Kobayashi, T. Yagi, S. Yamaguchi, *Solid State Ionics* 179 (2008) 236-242.

[09Igu] F. Iguchi, T. Tsurui, N. Sata, Y. Nagao, H. Yugami, *Solid State Ionics* 180 (2009) 563-568.

[09Ima] S. Imashuku, Ph. D. Thesis, Kyoto University, 2009.

[09Yam] Y. Yamasaki, R. Hernandez-Sanchez, S.M. Haile, *Chem. Mater.* 21 (2009) 2755-2762.

[10Ima] S. Imashuku, T. Uda, Y. Nose, Y. Awakura, *J. Phase Equilib. Diff.* 31 (2010) 348-356.

[10Fab] E. Fabbri, D. Pergolesi, E. Traversa, *Chem. Soc. Rev*. 39 (2010) 4355-4369.

[10Per] D. Pergolesi, E. Fabbri, A. D'Epifanio, E.D. Bartolomeo, A. Tebano, S. Sanna, S. Licoccia, G. Balestrino, E. Traversa, *Nat. Mater*. 9 (2010) 846-852.

[10Sto] S.J. Stokes, M.S. Islam, *J. Mater. Chem.* 20 (2010) 6258-6264.

[10Yam] Y. Yamazaki, R, Hernandez-Sanchez, S.M. Haile, *J. Mater. Chem*. 20 (2010) 8158-8166.

[11Gia] F. Giannici, M. Shirpour, A. Longo, A. Martorana, R. Merkle, J. Maier, Chem. Mater. doi: 10.1021/cm200682.

[11Ima] S. Imashuku, T. Uda, Y, Nose, Y. Awakura, *J. Alloy Compd.* 509 (2011) 3872-3879.

Chapter 4

Evaluation of Site Occupation of Sc, Sm, Eu and Dy in BaZrO$_3$ by Powder X-ray Diffraction with Synchrotron Radiation

4.1 Introduction

The synchrotron radiation has attractive advantages in XRD analysis as already shown in Chapter 3, such as high brightness and monochromaticity.   In this chapter, powder XRD analyses were further applied to evaluate the site occupation of Sc, Dy, Sm and Eu in doped BaZrO$_3$.

4.2 Experimental

The Sc-doped BaZrO$_3$ with the nominal compositions of BaZr$_{0.8}$Sc$_{0.2}$O$_{3-\delta}$ and Ba$_{0.9}$Zr$_{0.8}$Sc$_{0.2}$O$_{3-\delta}$, Eu-doped sample of BaZr$_{0.8}$Eu$_{0.2}$O$_{3-\delta}$, and Dy-doped sample of BaZr$_{0.8}$Dy$_{0.2}$O$_{3-\delta}$ were prepared by conventional solid state reaction method as in Chapter 2 and 3.   For sintering, the heating profile is the same as the "*slow heating process*" as described in Chapter 3.

Sample compositions were measured by ICP-AES, and energy dispersive X-ray spectroscopy (EDX, EDAX, Genesis-XM2) equipped with a scanning electron microscope (SEM, Keyence Corporation, VE-7800).   Powder XRD analysis was performed by using the BL19B2 beam line at SPring-8 with the approval of the Japan Synchrotron Radiation Research Institute (JASRI) as industrial application proposal (proposal No. 2010B1850). The incident energy was 17.026 keV.   The samples for measurement were sealed in Lindemann glass made capillaries.   Rietveld refinement was performed by TOPAS.

4.3 Results

4.3.1 Evaluation of Site Occupation of Sc in BaZrO₃

The total compositions of the samples are summarized in Table 4.1.   Since coexistence of perovskite-type and Sc_2O_3 phases was confirmed from the XRD pattern of the Ba-deficient sample of $Ba_{0.9}Zr_{0.8}Sc_{0.2}O_{3-\delta}$, EDX was applied to evaluate the composition of individual grains, with the results plotted in the pseudo-ternary phase diagram of BaO - ZrO_2 - $ScO_{1.5}$ as shown in Figure 4.1.   Only the perovskite-type phase was detected by EDX, and the average composition is calculated to be $Ba_{1.00}Zr_{0.87}Sc_{0.13}O_{3-\delta}$.

Table 4.1 Total compositions of the as-sintered samples measured by ICP-AES.

Dopant	Nominal composition	Actual composition
Sc	$Ba_{0.9}Zr_{0.8}Sc_{0.2}O_{3-\delta}$	$Ba_{0.93}Zr_{0.84}Sc_{0.16}O_{3-\delta}$
	$BaZr_{0.8}Sc_{0.2}O_{3-\delta}$	$BaZr_{0.81}Sc_{0.19}O_{3-\delta}$
Sm	$BaZr_{0.8}Sm_{0.2}O_{3-\delta}$	$Ba_{0.98}Zr_{0.81}Sm_{0.19}O_{3-\delta}$
Eu	$BaZr_{0.8}Eu_{0.2}O_{3-\delta}$	$Ba_{0.96}Zr_{0.82}Eu_{0.18}O_{3-\delta}$
Dy	$BaZr_{0.8}Dy_{0.2}O_{3-\delta}$	$Ba_{0.97}Zr_{0.81}Dy_{0.19}O_{3-\delta}$

It is interesting to consider with the reported pseudo-ternary phase diagram of BaO - ZrO_2 - $ScO_{1.5}$ established at 1600 °C [07Ima], as shown in Figure 4.2.   The total composition of this sample identified by ICP-AES is marked as solid triangle, located in the two phase area of $BaZrO_3$ solid solution and Sc_2O_3.   The solid circle indicates the composition of $BaZrO_3$ solid solution confirmed by EDX.   By extending the lines connecting these two points, the intersection point of this line with the abscissa is located in the region for single Sc_2O_3 phase. It implies that the coexistence of perovskite-type $BaZrO_3$ solid solution and Sc_2O_3 phases for the sample with the total composition of $Ba_{0.93}Zr_{0.84}Sc_{0.16}O_{3-\delta}$ confirmed by experimental analysis also meets the phase relationship, and therefore can be considered to be in equilibrium at the sintering temperature.
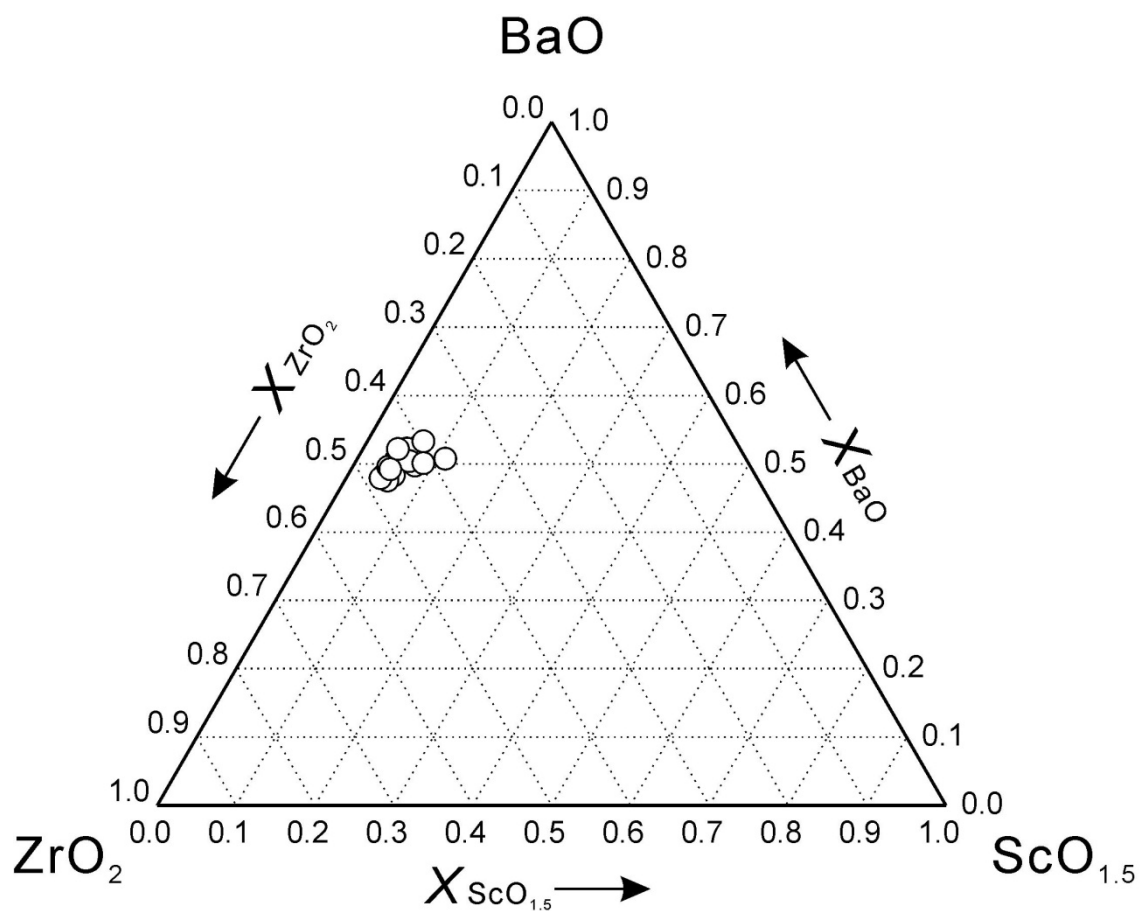
Figure 4.1 EDX Results of grain compositions of the sample with the nominal composition of $Ba_{0.9}Zr_{0.8}Sc_{0.2}O_{3-\delta}$ plotted in pseudo-ternary phase diagram of BaO - ZrO_2 - $ScO_{1.5}$.

Then Rietveld refinements were performed based on the similar compositional constraints established as illustrated in 3.4.4 for Y-doped $BaZrO_3$. It is generally regarded that only in the Ba-deficient sample can dopant cations partition into A-site. However, for the Sc-doped samples prepared in this work, there is no Ba-deficiency for the perovskite-type phase in either the nominally stoichiometric or Ba-deficient sample, therefore, it is considered that Sc cations cannot partition into A-site due to lack of available open seats, and were preliminarily fixed in B-site. Thus, the batches of Rietveld refinement for the Sc-doped samples here are not with the purpose to evaluate the site occupation of Sc, but verify the reasonability of fixing Sc in B-site. Cubic perovskite-type structure model of *pm-3m* was used for the refinements. The fitting profiles for the samples with the nominal compositions

of $Ba_{0.9}Zr_{0.8}Sc_{0.2}O_{3-\delta}$ and $BaZr_{0.8}Sc_{0.2}O_{3-\delta}$ are exhibited in Figure 4.3 and 4.4, respectively. And the R_{wp} for these two refinements are 8.75 % and 8.47 %, respectively, indicating good fitting qualities.   Therefore, assigning Sc for B-site occupation is considered to be reasonable.
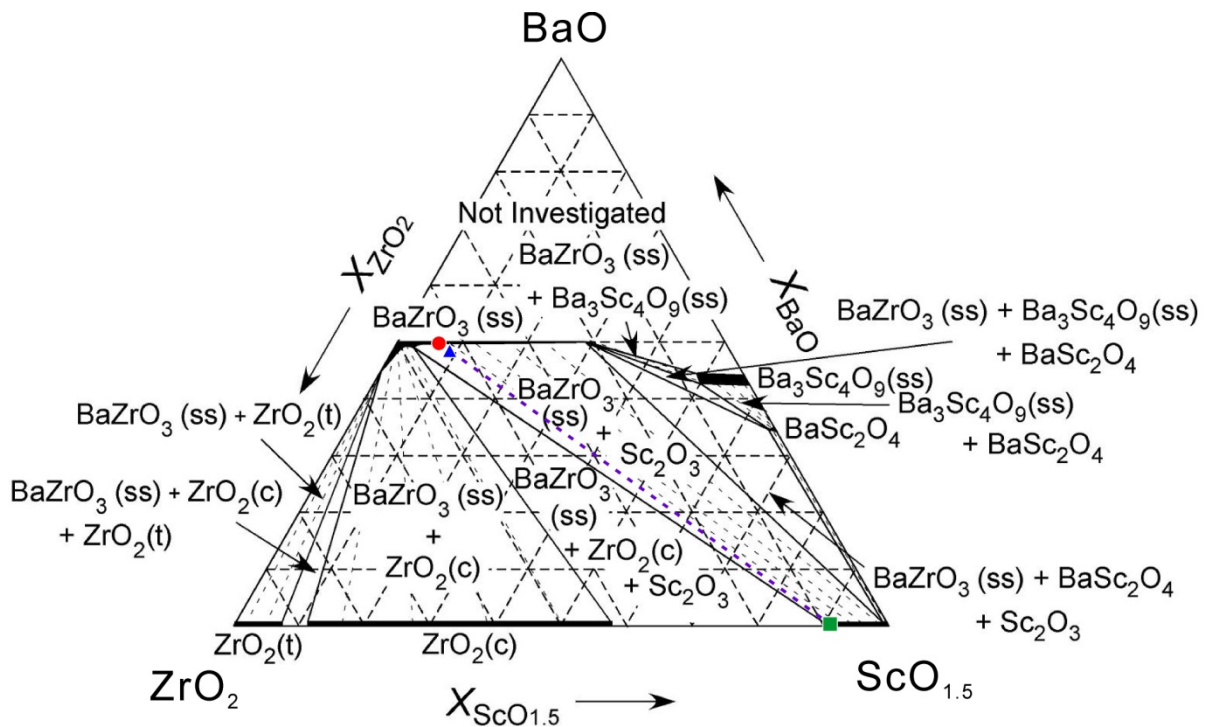

Figure 4.2 Comparison of the phase relationship observed in $Ba_{0.9}Zr_{0.8}Sc_{0.2}O_{3-\delta}$ in this work with the reported BaO - ZrO_2 - $ScO_{1.5}$ pseudo-ternary phase diagram established at 1600 °C [07Ima].   The solid triangle indicates the total composition evaluated by ICP-AES.   The solid circle indicates the grain composition of Sc-doped $BaZrO_3$ phase evaluated by EDX.   And the solid square represents the Sc_2O_3 phase, which is obtained as the intersection point of the abscissa and the line through the points of total composition and composition of Sc-doped $BaZrO_3$ phase.

4.3.2 Evaluation of Site Occupation of Sm in BaZrO₃

The fitting profile of the sample with the nominal composition of $BaZr_{0.8}Sm_{0.2}O_{3-\delta}$ by using the composition given in Table 4.1 is as shown in Figure 4.5.   Cubic structure model of *pm-3m* was used in this refinement.   The refined formula is expressed as $(Ba_{0.9899}Sm_{0.0101})(Zr_{0.8182}Sm_{0.1818})O_{3-\delta}$, indicating about 5.26 % of Sm occupied A-site in this
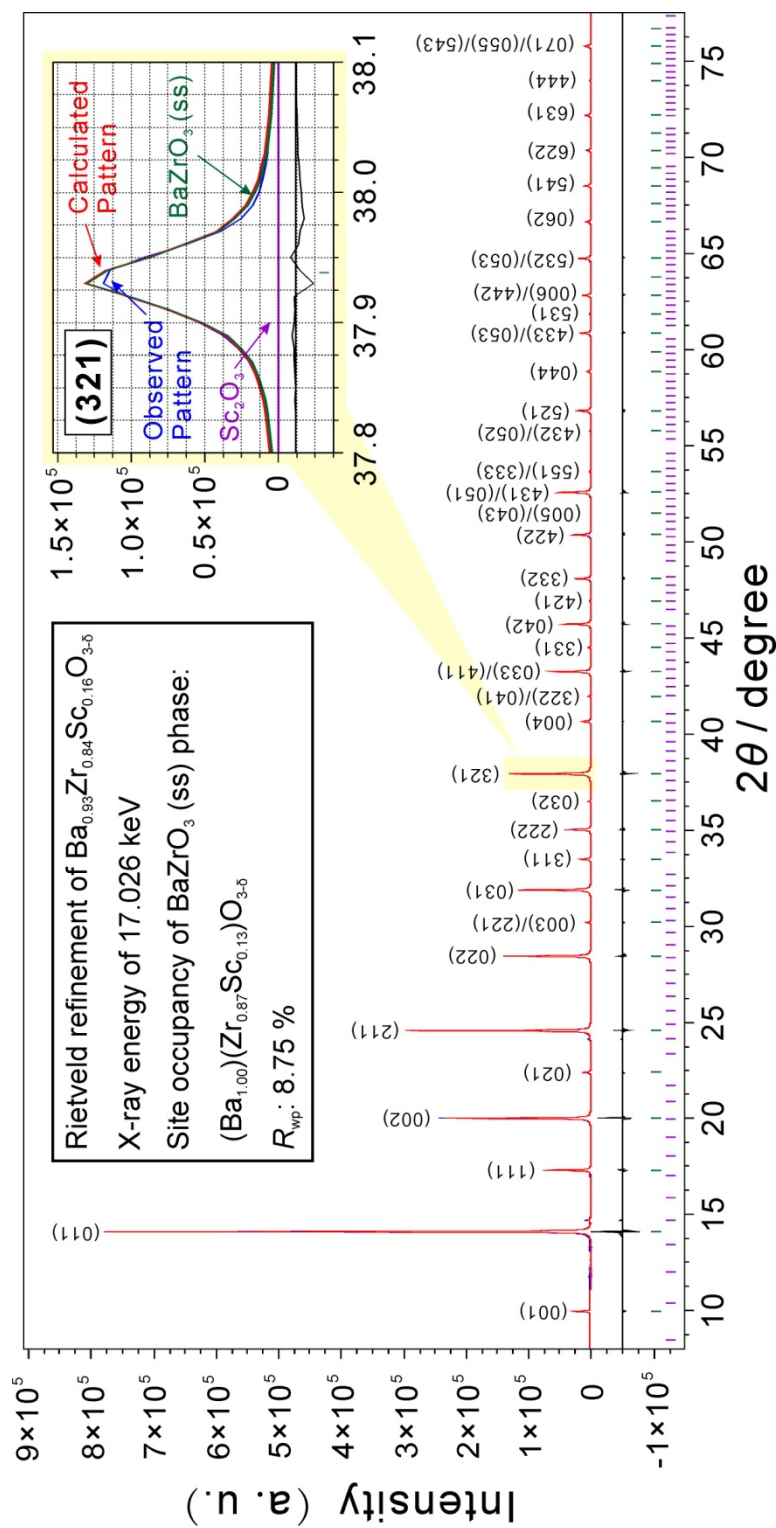
Figure 4.3 Rietveld refinement fitting of pattern of the sample with the nominal composition of $Ba_{0.9}Zr_{0.8}Sc_{0.2}O_{3-\delta}$ collected with incident X-ray energy of 17.026 keV. The fitting of the (321) reflection belonging to perovskite-type pattern is highlighted as inset in the top right corner. Observed pattern (blue), calculated pattern (red), difference (black, at bottom) and the Bragg peaks of the candidate phases (vertical lines) are shown.
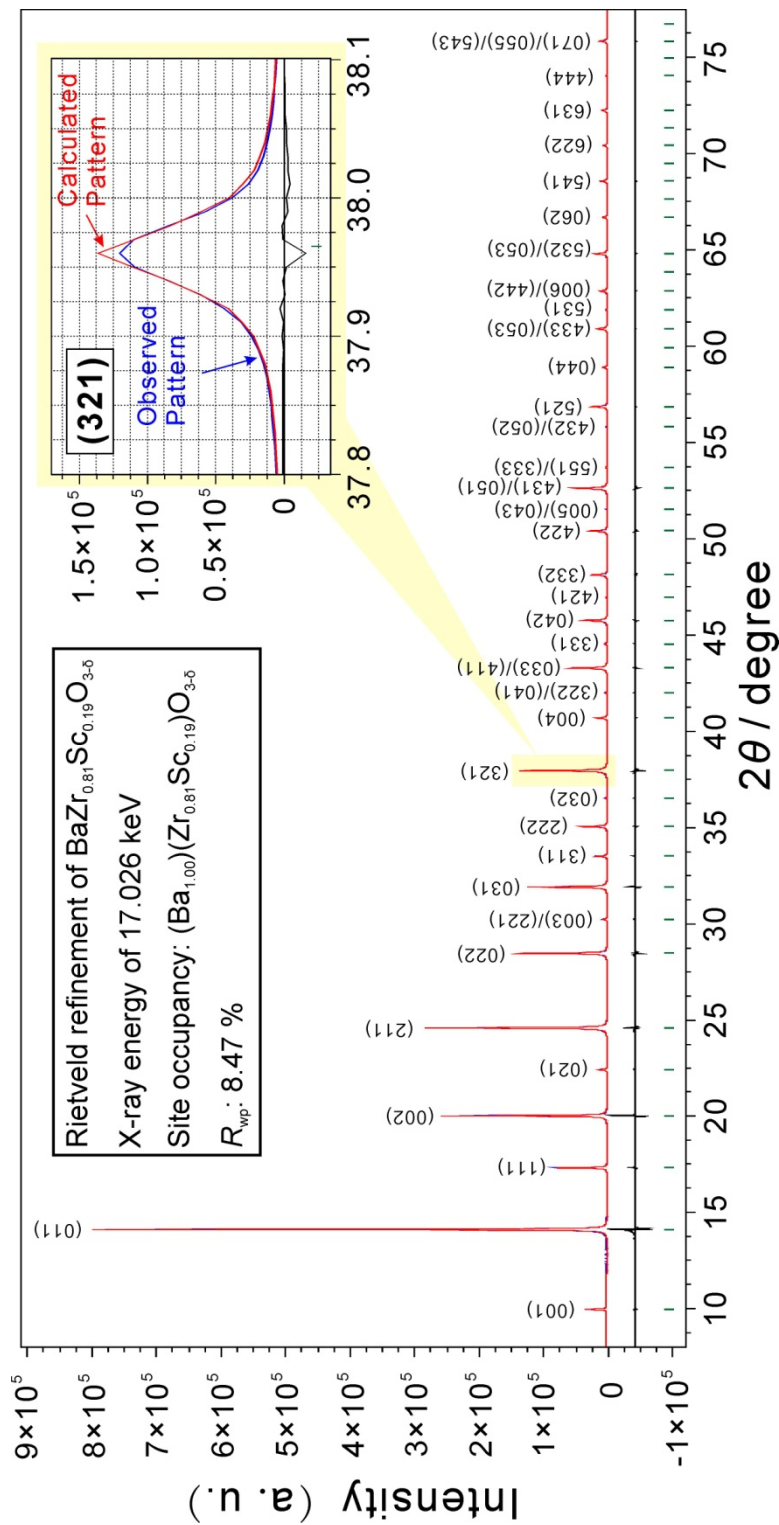
Figure 4.4 Rietveld refinement fitting of pattern of the sample with the nominal composition of $BaZr_{0.8}Sc_{0.2}O_{3-\delta}$ collected with incident X-ray energy of 17.026 keV. The fitting of the (321) reflection belonging to perovskite-type pattern is highlighted as inset in the top right corner. Observed pattern (blue), calculated pattern (red), difference (black, at bottom) and the Bragg peaks of the candidate phases (vertical lines) are shown.

sample with Ba-deficiency of 0.02.   However, R_{wp} was calculated to be 14.38 %, which means the refinement result is not very good.   The reason for this high R_{wp} value is attributed to the poor symmetry of the peaks, as can be observed in the inset in Figure 4.5 taking the (321) reflection for example.   The same phenomenon was also confirmed in the nominally stoichiometric Y-doped $BaZrO_3$, as described in Chapter 3.   For refinement of higher quality, further precise analysis to evaluate the structure and composition of this sample is essential.

4.3.3 Evaluation of Site Occupation of Eu in BaZrO$_3$

Since only the peaks of perovskite-type pattern with good symmetry are observed from the XRD pattern, the sample with the nominal composition of $BaZr_{0.8}Eu_{0.2}O_{3-\delta}$ is considered to be of perovskite-type single phase, and the cubic structure model of *pm-3m* was used for the Rietveld refinement.   The fitting profile is shown in Figure 4.6, and a value of 8.75 % was obtained for R_{wp}, indicating a good quality for the fitting.   The refined formula is expressed as $(Ba_{0.9783}Eu_{0.0191})(Zr_{0.8356}Eu_{0.1644})O_{3-\delta}$, therefore, about 10.41 % of Eu occupies the A-site in this sample.

4.3.4 Evaluation of Site Occupation of Dy in BaZrO$_3$

The sample with the nominal composition of $BaZr_{0.8}Dy_{0.2}O_{3-\delta}$ is also considered to be of perovskite-type single phase from the XRD pattern.   The cubic structure model of *pm-3m* was used for the Rietveld refinement.   The fitting profile is shown in Figure 4.7, and a value of 9.21 % was obtained for R_{wp}, indicating an acceptable fitting quality.   The refined formula is expressed as $(Ba_{0.9792}Dy_{0.0095})(Zr_{0.8177}Dy_{0.1823})O_{3-\delta}$, from which about 4.95 % of Dy occupying the A-site is evaluated.
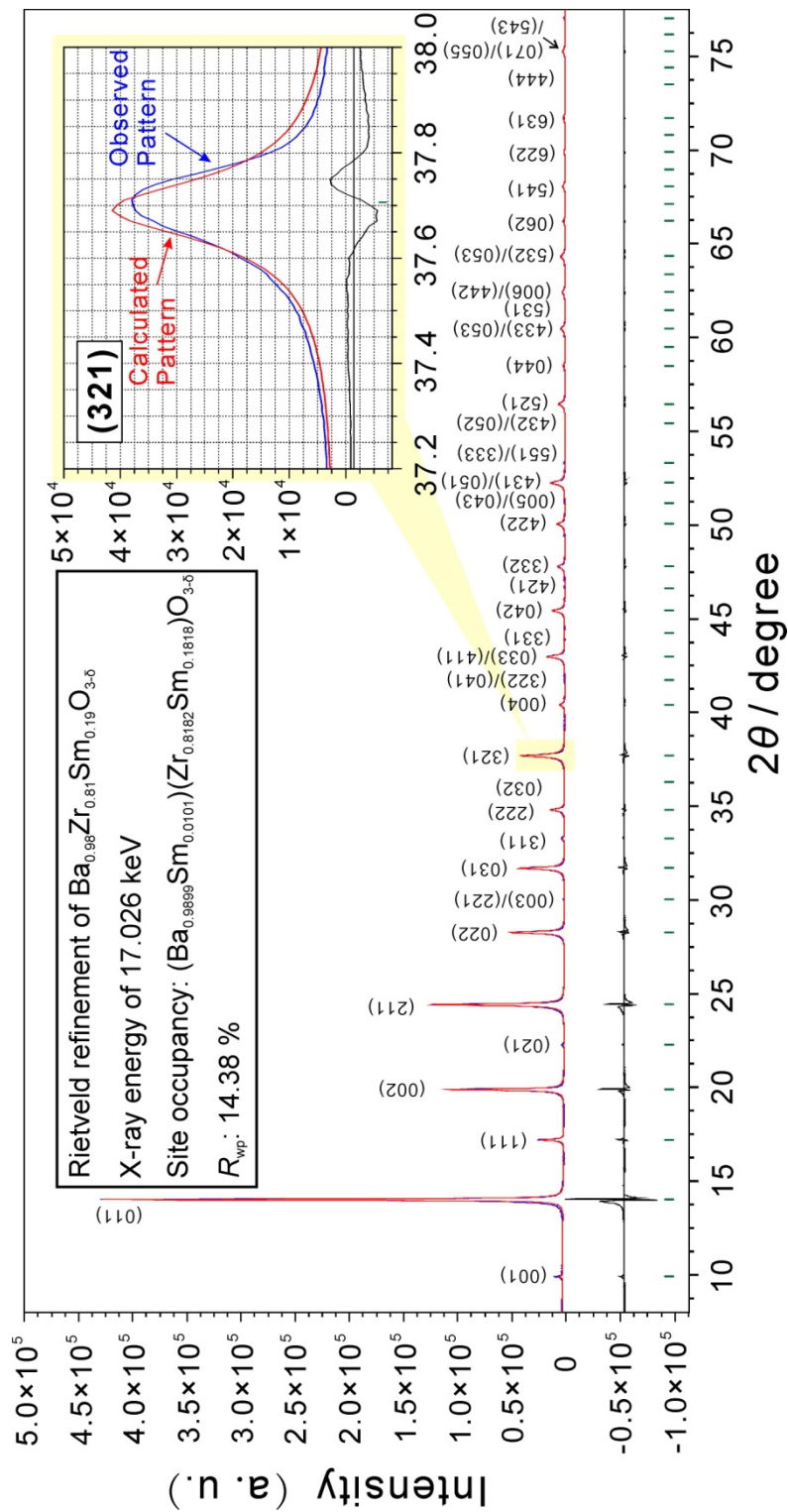
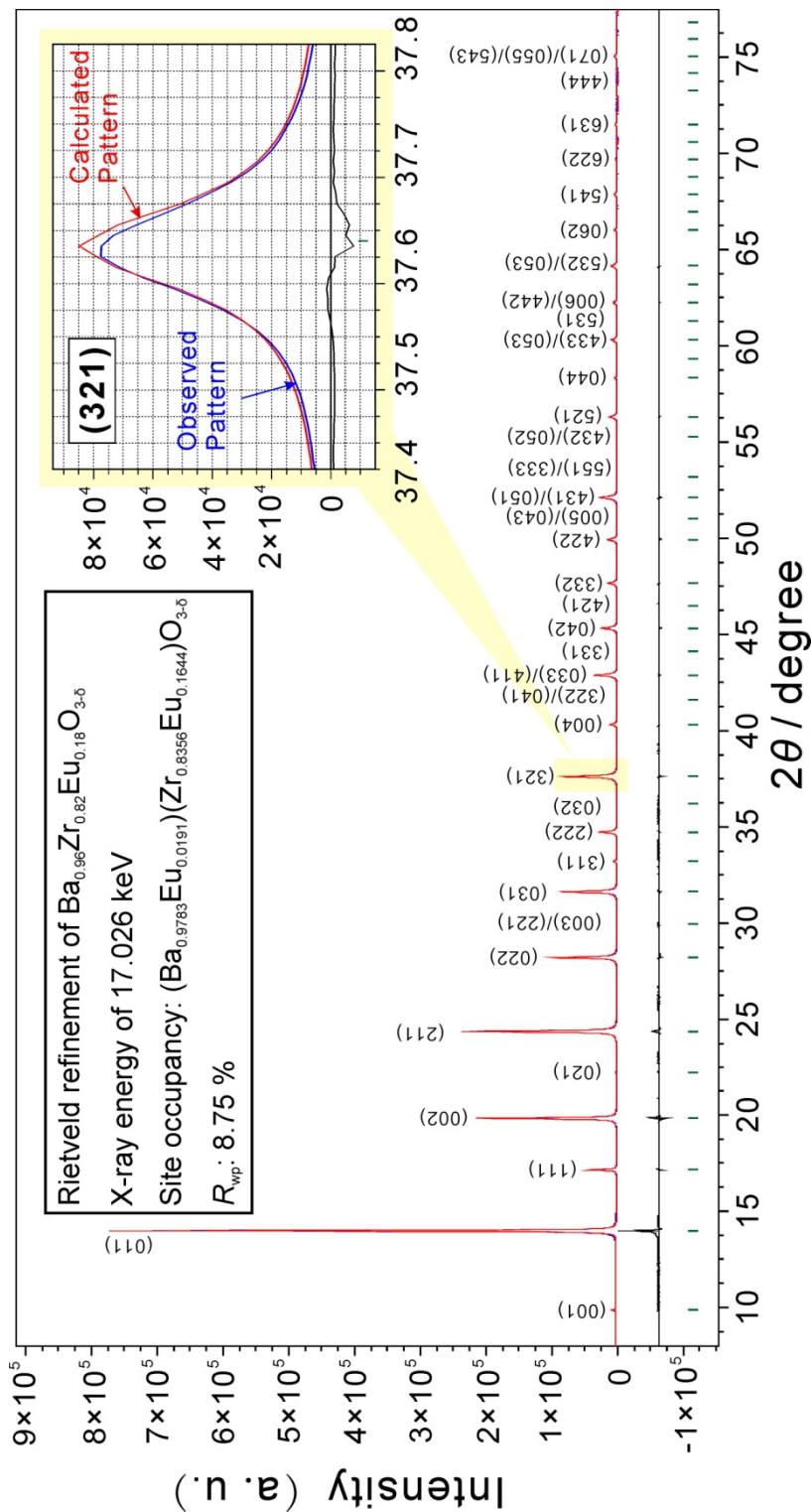**Figure 4.5** Rietveld refinement fitting of pattern of the sample with the nominal composition of $BaZr_{0.8}Sm_{0.2}O_{3-\delta}$ collected with incident X-ray energy of 17.026 keV. The fitting of the (321) reflection belonging to perovskite-type pattern is highlighted as inset in the top right corner. Observed pattern (blue), calculated pattern (red), difference (black, at bottom) and the Bragg peaks of the candidate phases (vertical lines) are shown.
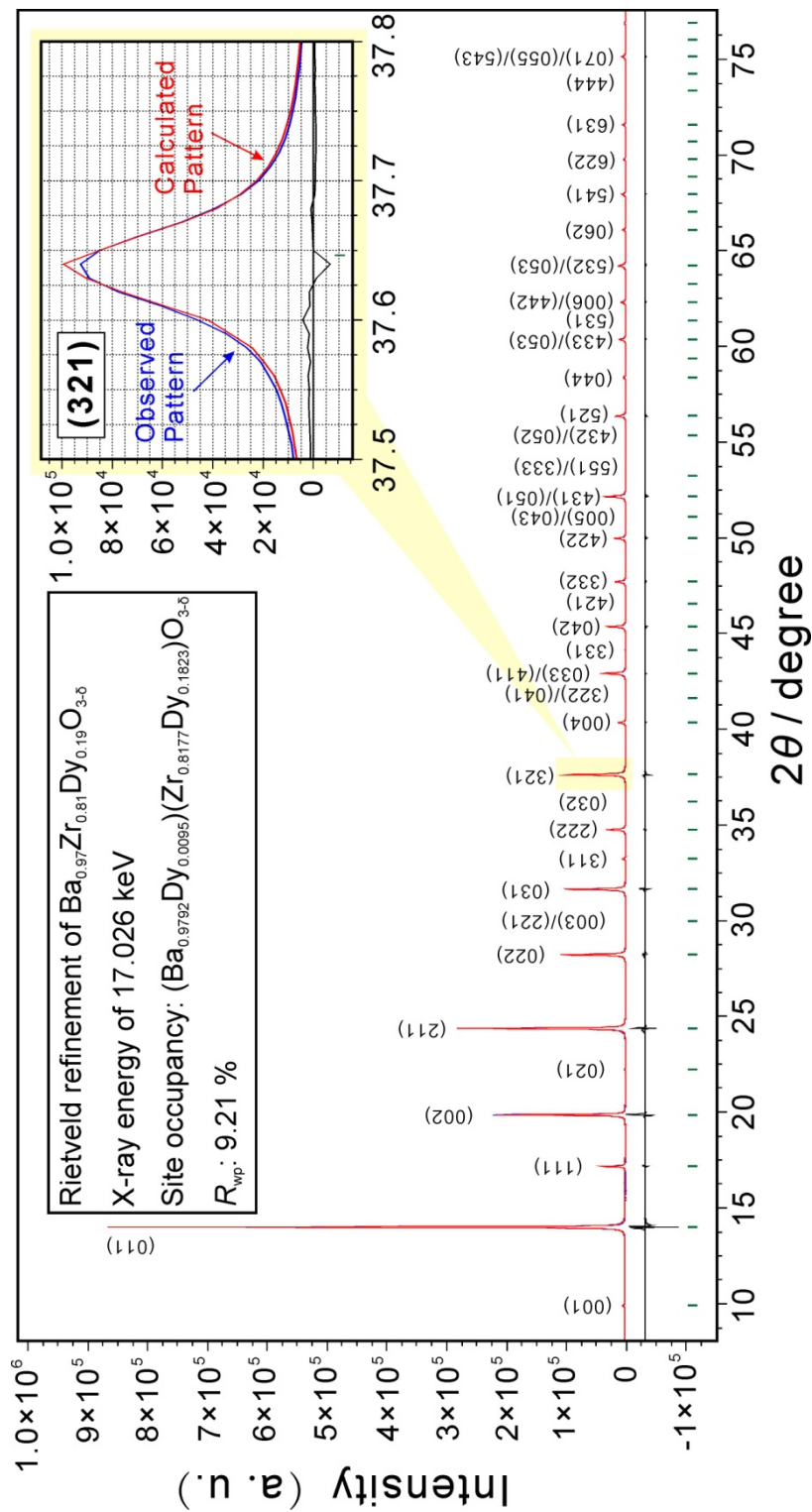
Figure 4.6 Rietveld refinement fitting of pattern of the sample with the nominal composition of $BaZr_{0.8}Eu_{0.2}O_{3-\delta}$ collected with incident X-ray energy of 17.026 keV. The fitting of the (321) reflection belonging to perovskite-type pattern is highlighted as inset in the top right corner. Observed pattern (blue), calculated pattern (red), difference (black, at bottom) and the Bragg peaks of the candidate phases (vertical lines) are shown.

Figure 4.7 Rietveld refinement fitting of pattern of the sample with the nominal composition of $BaZr_{0.8}Dy_{0.2}O_{3-\delta}$ collected with incident X-ray energy of 17.026 keV. The fitting of the (321) reflection belonging to perovskite-type pattern is highlighted as inset in the top right corner. Observed pattern (blue), calculated pattern (red), difference (black, at bottom) and the Bragg peaks of the candidate phases (vertical lines) are shown.

Chapter 4

4.4 Discussion

A combined summary of the results of Chapter 2 to 4 is preferred here. In Chapter 2, by evaluating the lattice volume difference between the Ba-rich and Ba-poor samples, Sc was determined to be only of B-site occupation, which is the same as the conclusion drawn in this chapter. Sm and Eu were evaluated to be amphoteric dopants for $BaZrO_3$ for occupying both the A and B-sites in Chapter 2. And the same results were also achieved in this chapter that relatively large amount of about 5.26 % of the doped Sm partitioned into A-site for the sample containing a slight Ba-deficiency of 0.02, and about 10.41 % of the doped Eu partitioned into A-site for the sample containing a Ba-deficiency of 0.04. However, in Chapter 2, Y and Dy were evaluated to solely occupy the B-site. But the results of Chapter 3 imply that for the slightly Ba-deficient sample, Y was estimated to be only of B-site occupation. When much Ba-deficiency is introduced, some of the doped Y also partitioned into A-site. While in this Chapter, for the sample with slight Ba-deficiency of 0.03, a small amount of Dy was evaluated to occupy A-site. Anyhow, compared with the amount of Sm and Eu occupying the A-site, the amount of A-site occupying Dy was relatively small. The reason for the difference in the results referring to the site occupancy evaluation of Y and Dy in $BaZrO_3$ is considered to be dependent on the sensitivity of the analysis method. In comparison with the method by applying the high-brightness monochromatic synchrotron radiation for XRD pattern collection in Chapter 3 and 4, the method adopted in Chapter 2 as evaluating the lattice volume difference is more susceptible to experimental errors.

By combining the results obtained from Chapter 2 to Chapter 4, the capacity occupying A-site of the dopants can be sequenced as Eu > Sm > Dy > Y > Sc. And such sequence is comparable to the six-fold coordinated Shannon radii for trivalent cations as Sm(III) (0.958 Å), Eu(III) (0.947 Å) > Dy(III) (0.912 Å) > Y(III) (0.900 Å) > Sc(III) (0.745 Å) [76Sha]. Therefore, it can also be concluded that the site occupation of dopants in $BaZrO_3$ greatly

depends on their radii.   For larger dopant cations, they exhibit stronger capability for A-site occupation.

4.5 Conclusions

Synchrotron radiation was applied for XRD pattern collection.   By utilizing the Rietveld refinement, the site occupation of Sc, Sm, Eu and Dy in BaZrO$_3$ were evaluated. The results revealed that Sc was only of B-site occupation.   In addition to the B-site occupation, a small amount of Dy was evaluated to occupy the A-site for the sample with Ba-deficiency of 0.03.   Meanwhile, relatively larger amounts of Sm and Eu occupying A-site were evaluated, implying more amphoteric behaviors of Sm and Eu when doped into BaZrO$_3$.

References

[76Sha] R.D. Shannon, *Acta Crystallogr. A* 32 (1976) 751-767.

[07Ima] S. Imashuku, T. Uda, T. Ichitsubo, E. Matsubara, Y. Awakura, *J. Phase Equilib. Diff.* 28 (2007) 517-522.

Chapter 5

Atmosphere Dependence of Valence State of Dy in BaZrO$_3$

5.1 Introduction

In Chapter 2, the water content of Dy-doped BaZrO$_3$ exhibited obvious dependence on the atmosphere for hydration. Relatively high water content was measured when the sample was hydrated in humid Ar. And an obvious decrease of water content was observed when the hydration atmosphere altered from humid Ar to O$_2$. Such phenomenon probably attributes to the decreased sites for water molecule accommodation, namely oxide ion vacancies in perovskite-type oxides, in oxidizing atmosphere. And it is common for perovskite-type oxides containing multivalent cations, which intend to be oxidized to higher valence states, resulting in a consumption of oxide ion vacancies for charge compensation [85Miz, 89Miz, 91Miz, 95Tai].

Brauer *et al*. [80Bra] reported a partial existence of tetravalent dysprosium cations (Dy (IV)) when doped into BaCeO$_3$. But a later work of Soderholm *et al*. [87Sod] did not trace the existence evidence of Dy(IV) in BaCeO$_3$. However, since the six-fold coordinated radius of Zr(IV) cation (0.72 Å [76Sha]) is smaller than that of Ce(IV) cation (0.87 Å [76Sha]), and the Dy(III) cation (0.912 Å [76Sha]) is much larger than Dy(IV) cation (0.78 Å [74Kno]), it might be easier for Dy cations to exist as tetravalent in BaZrO$_3$ than in BaCeO$_3$. If so, the atmosphere dependence of water content in Dy-doped BaZrO$_3$ can be understood. In this work, in order to verify the valence of Dy in the BaZrO$_3$ system, solid solutions of BaZr$_{0.8}$Dy$_x$Y$_{0.2-x}$O$_{3-\delta}$ (x = 0.05, 0.1, 0.15) were prepared. And the atmosphere dependence of valence state of Dy was investigated from crystal structures, conductivities, and water incorporation behaviors.

5.2 Experimental

Samples were prepared by conventional solid state reaction. The same process was performed before sintering as described in Chapter 2 and 3. For sintering, the pellets were heated up to the sintering temperature of 1600 $^{\circ}$C at the rate about 4 $^{\circ}$Cmin^{-1} in an O_2 flow, kept for 24 h, and finally furnace cooled to room temperature. Morphologies of the sintered pellets were observed by SEM. Total compositions were measured by ICP-AES. Structures of the samples were identified by XRD. And the lattice volumes were calculated by Rietveld refinement with X'Pert HighScore Plus.

After mechanically polishing the surface of a sintered pellet, palladium thin films were deposited by electroless plating as electrodes. The impedance spectra of the pellet were collected by a.c. impedance spectroscopy in the frequency range from 10 Hz to 7 MHz using a frequency response analyzer (Solartron SI 1260) with applied voltage of 100 mV. In order to saturate water in pellet quickly, the pellet was held at 700 $^{\circ}$C for more than 30 h, and then cooled to 100 $^{\circ}$C at a rate of 0.2 $^{\circ}$Cmin^{-1}. The impedance was measured at the interval of 50 min. An equivalent circuit model was fitted to the impedance spectra by using Z Plot (Scribner Associates Inc.). By a.c. impedance measurement, two semicircles were observed as shown in Figure 5.1. Based on the equivalent circuit, the two circles came from bulk and grain boundary, and the diameters of the semicircles corresponded to their resistances. It is reported that the capacitances corresponding to bulk and grain boundary are about the magnitude of 10^{-11} F and 10^{-9} F, respectively [86Ger, 99Dus]. Therefore, these semicircles could be identified whether belonged to bulk or grain boundary by evaluating the capacitance. Then, the bulk conductivities were calculated by utilizing the cross-section area and length of the pellet.

Water contents of the hydrated samples were measured by Karl-Fischer titration method, as described in Chapter 2. In this work, samples with the size of 2 mm in length,

which were broken from sintered pellets, were placed in atmosphere of 5% H_2O - Ar or 5% H_2O - O_2 at various temperatures for 72 h for water saturation.
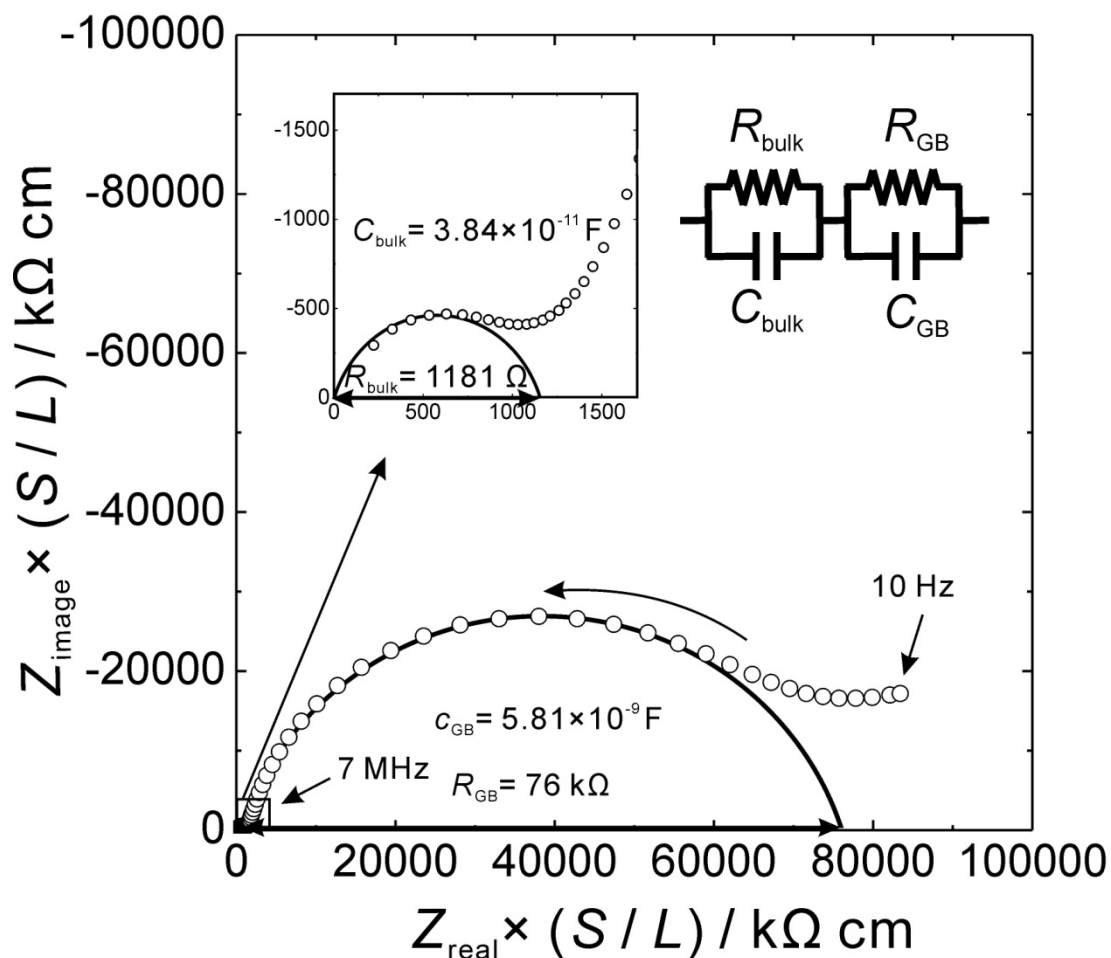

Figure 5.1 Impedance spectra of $BaZr_{0.8}Dy_{0.2}O_{3-\delta}$ measured in the atmosphere of 30% - H_2 at $147^{o}C$. The sample was sintered at $1600^{o}C$ for 24 h in an O_2 flow. R_{GB} and C_{GB} are resistance and capacitance of grain boundary, respectively. And R_{bulk} and C_{bulk} are resistance and capacitance of bulk, respectively.

5.3 Results

5.3.1 Structure and Morphology

XRD patterns of $BaZr_{0.8}Dy_xY_{0.2-x}O_{3-\delta}$ (BZDY), as shown in Figure 5.2, indicated that regardless of the variation of Dy and Y contents, all the sintered samples were of perovskite-type single phase, implying that Dy and Y dissolved into the lattice of $BaZrO_3$

with arbitrary ratio when the nominal atomic ratio of Ba : Zr : (Dy + Y) is 1 : 0.8 : 0.2.   As shown in Figure 5.3, there was little difference in morphologies of the samples with different Dy and Y contents.   All the pellets were dense after sintering.   The crystal lattice volume of BZDY after being sintered, and annealed in H_2 and O_2 subsequently, are shown in Figure 5.4. It is interesting that the lattice volume of as-sintered BZDY decreased with the increasing Dy content, indicated as solid circles in Figure 5.4, although the six-coordinated radius of Dy(III) cation (0.912 Å [76Sha]) is larger than that of Y(III) cation (0.900 Å [76Sha]).   After being annealed in H_2 for 72 h at 600 ^{o}C, as shown as symbols of blue solid squares in Figure 5.4, an expansion of lattice volume from the oxidized state was observed in each Dy-doped sample. The Dy content dependence in the variation of lattice volume became smaller.   When annealed in O_2 at 600 ^{o}C for 72 h again, as indicated as solid triangles in Figure 5.4, the lattice volumes became small again and approached to the former values for the as-sintered samples. However, little variation of lattice volume of the solely Y-doped sample was observed.
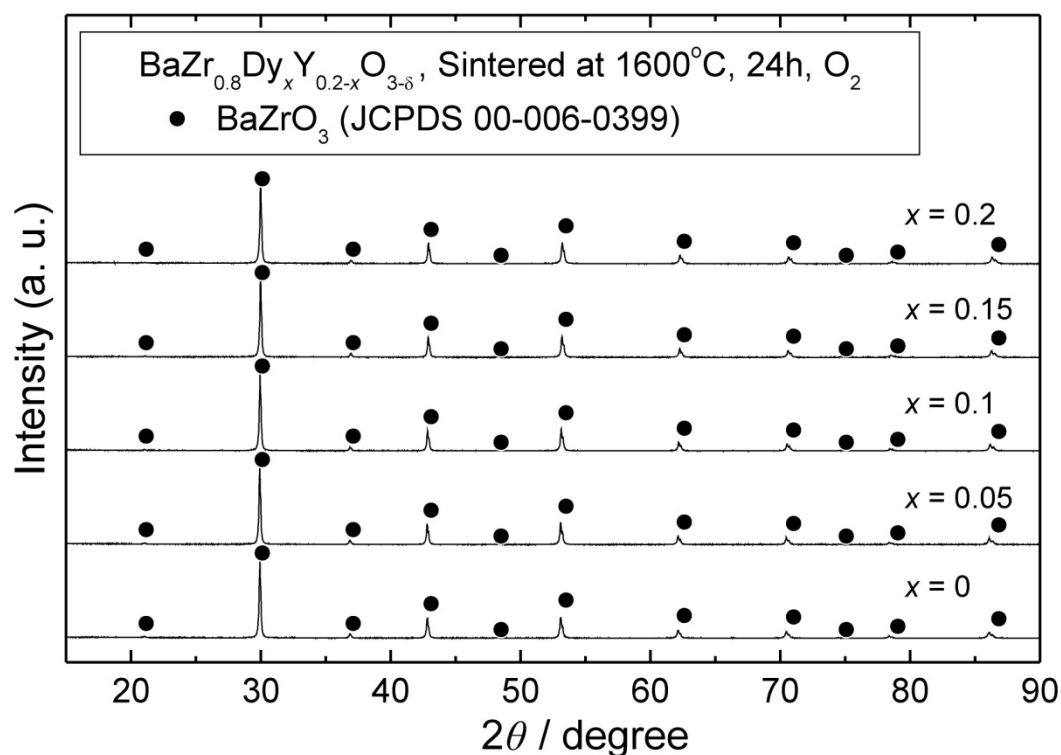
Figure 5.2 XRD patterns of $BaZr_{0.8}Dy_{0.2-x}Y_xO_{3-\delta}$ (x = 0, 0.05, 0.1, 0.15, 0.2).   All the samples were sintered at 1600°C for 24h in an O_2 flow.
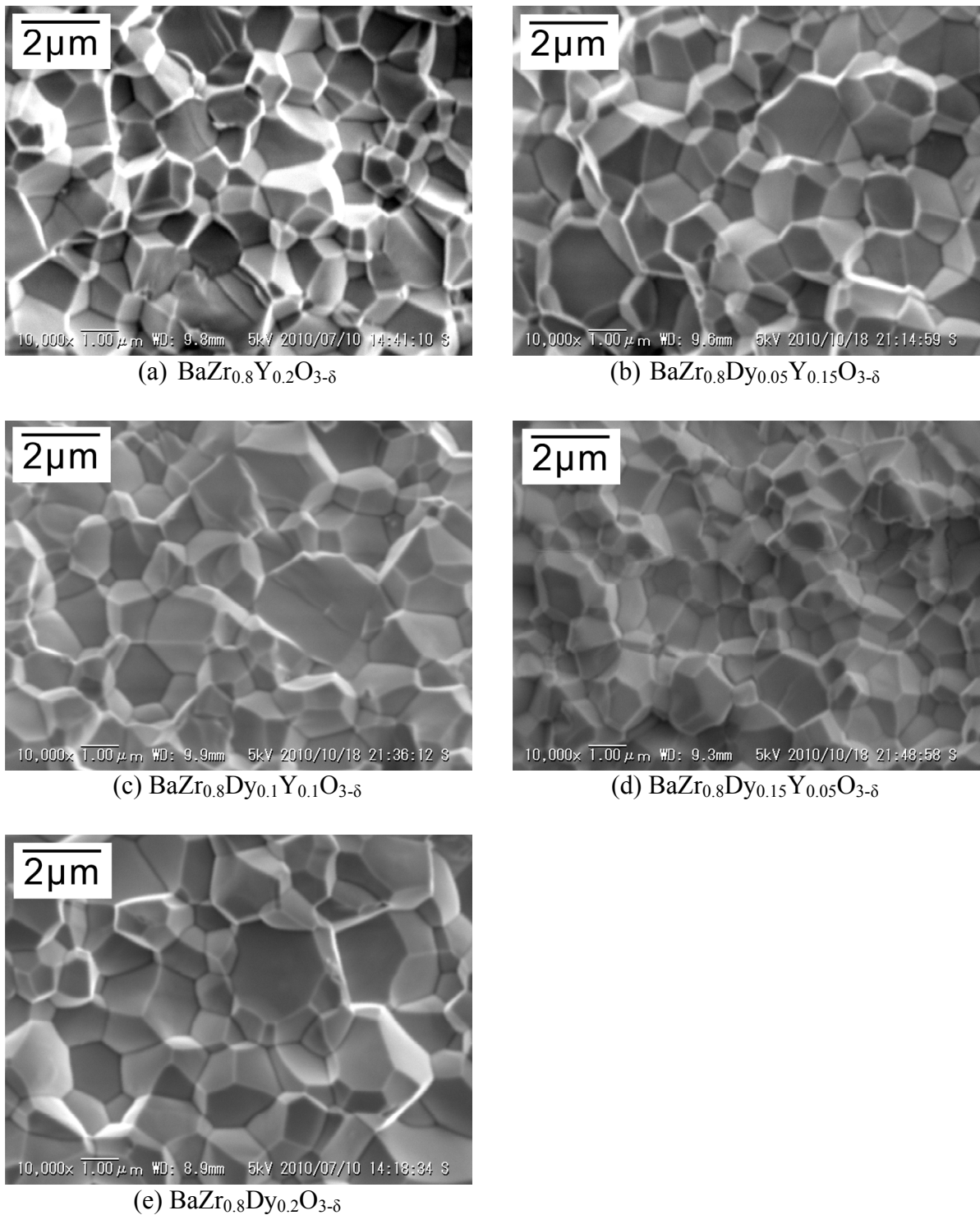
(a) $BaZr_{0.8}Y_{0.2}O_{3-\delta}$

(b) $BaZr_{0.8}Dy_{0.05}Y_{0.15}O_{3-\delta}$

(c) $BaZr_{0.8}Dy_{0.1}Y_{0.1}O_{3-\delta}$

(d) $BaZr_{0.8}Dy_{0.15}Y_{0.05}O_{3-\delta}$

(e) $BaZr_{0.8}Dy_{0.2}O_{3-\delta}$

Figure 5.3 SEM images of cross-sections of pellets of $BaZr_{0.8}Dy_xY_{0.2-x}O_{3-\delta}$ (x = 0, 0.05, 0.1, 0.15, 0.2) sintered at 1600°C for 24h in an O_2 flow.

5.3.2 Water Incorporation Behavior

The results of water content measurement of BZDY hydrated in 5% H_2O - Ar or 5% H_2O - O_2 are as shown in Figure 5.5.   The values of $BaZr_{0.8}Dy_{0.2}O_{3-\delta}$ and $BaZr_{0.8}Y_{0.2}O_{3-\delta}$
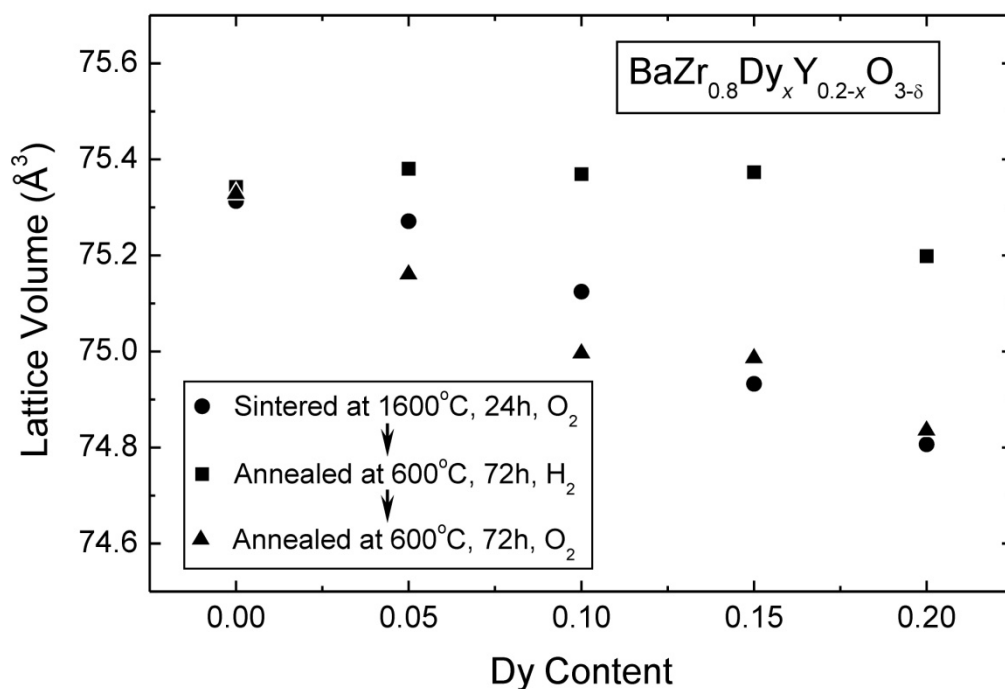
Figure 5.4 Lattice volume of $BaZr_{0.8}Dy_{0.2-x}Y_xO_{3-\delta}$ (x = 0, 0.05, 0.1, 0.15, 0.2), evaluated after being sintered at 1600^oC for 24 h in O_2, and subsequently annealed for 72 h in H_2, then annealed for 72 h in O_2 again, respectively.
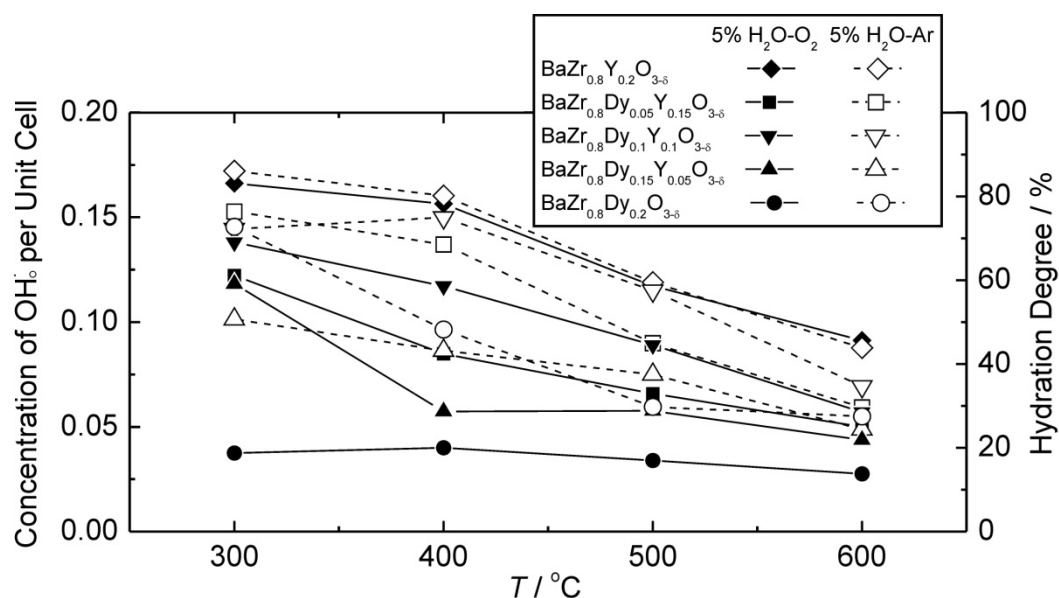
Figure 5.5 Concentration of hydroxide ions per unit cell of $BaZr_{0.8}Dy_xY_{0.2-x}O_{3-\delta}$ (x = 0.05, 0.1, 0.15) measured by Karl-Fischer titration method in 5% H_2O - O_2 or 5% H_2O - Ar.   The samples for measurement were of the size about 2 mm in length, broken from pellets sintered at 1600^oC for 24 h in an O_2 flow.   The reported values of $BaZr_{0.8}Y_{0.2}O_{3-\delta}$ and $BaZr_{0.8}Dy_{0.2}O_{3-\delta}$ were plotted for comparison.

already shown in Figure 2.7 in Chapter 2 are plotted for comparison.   The results revealed that although there was little difference in the concentrations of hydroxide ions per unit cell of $BaZr_{0.8}Y_{0.2}O_{3-\delta}$ between the measurements in 5% H_2O - Ar and 5% H_2O - O_2, for all the Dy-doped samples, higher concentrations of hydroxide ions were obtained when the samples were hydrated in humid Ar than O_2.

5.3.3 Conductivity Dependence on Atmosphere

The results of the measurements of the bulk conductivities of the samples of $BaZr_{0.8}M_{0.2}O_{3-\delta}$ (M = Sc, Y, Dy) are summarized in Figure 5.6.   It was observed that for the Sc and Y doped samples, there was little difference in conductivities measured in the atmosphere of wet O_2 or Ar.   As reported [08Ima], the bulk conductivity of $BaZr_{0.8}Sc_{0.2}O_{3-\delta}$ was more than one order of magnitude lower than that of $BaZr_{0.8}Y_{0.2}O_{3-\delta}$, although the

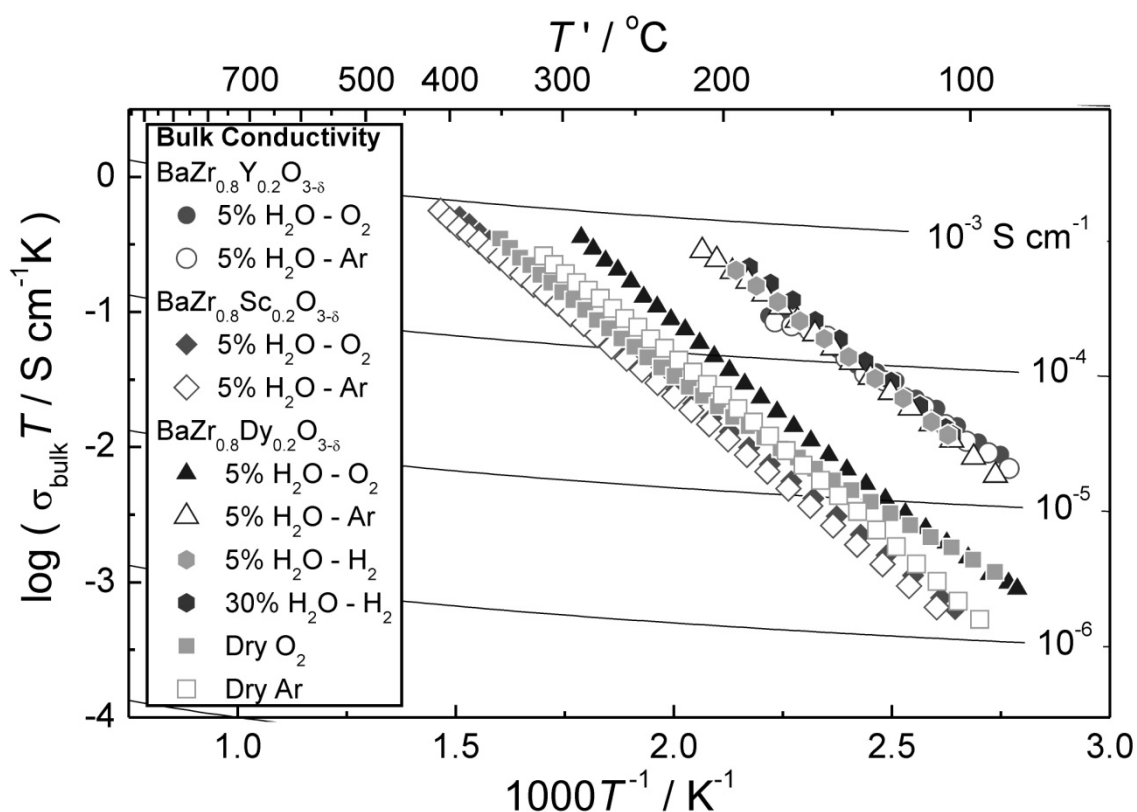**Figure 5.6** Conductivities of the samples of $BaZr_{0.8}M_{0.2}O_{3-\delta}$ (M = Sc, Y, Dy) as a function of temperature plotted in the Arrhenius form.

concentrations of hydroxide ions of the $BaZr_{0.8}M_{0.2}O_{3-\delta}$ (M = Sc, Y) samples are comparable, as shown in Figure 2.7. For the sample of $BaZr_{0.8}Dy_{0.2}O_{3-\delta}$, comparing to the measurements in dry O_2 or dry Ar, an elevation in bulk conductivity was observed in humid atmosphere, indicating the generation of protonic conduction in humid Ar. The bulk conductivities of $BaZr_{0.8}Dy_{0.2}O_{3-\delta}$ measured in humid Ar and H_2 were higher than in humid O_2, and comparable to that of $BaZr_{0.8}Y_{0.2}O_{3-\delta}$.
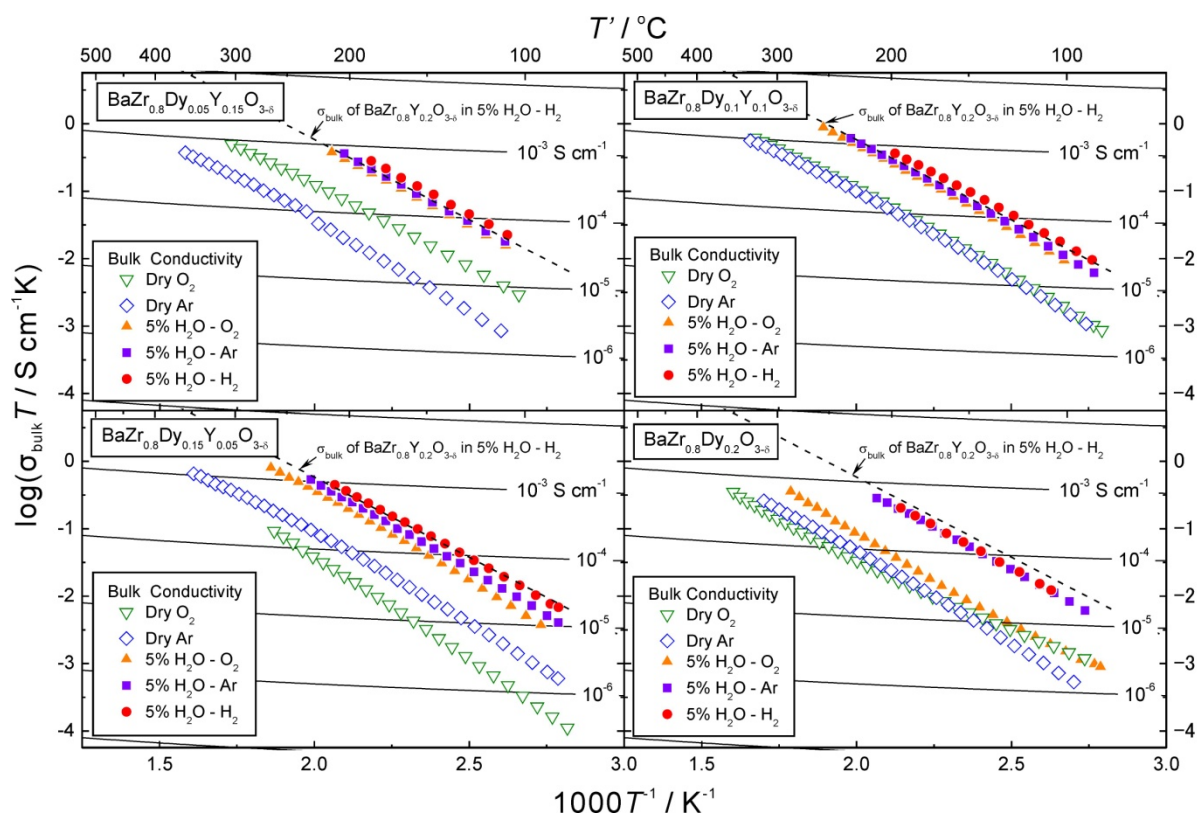
Figure 5.7 Bulk conductivities of (a) $BaZr_{0.8}Dy_{0.05}Y_{0.15}O_{3-\delta}$, (b) $BaZr_{0.8}Dy_{0.1}Y_{0.1}O_{3-\delta}$, (c) $BaZr_{0.8}Dy_{0.15}Y_{0.05}O_{3-\delta}$, and reported values of (d) $BaZr_{0.8}Dy_{0.2}O_{3-\delta}$ measured in various atmospheres as a function of temperature plotted in the Arrhenius form. The bulk conductivity of $BaZr_{0.8}Y_{0.2}O_{3-\delta}$ measured in 5% H_2O - H_2 is plotted as dash line as reference.

The bulk conductivities of the Dy-doped samples measured in various atmospheres are as shown in Figure 5.7. For all the samples, the bulk conductivities measured in humid Ar and O_2 were higher than those measured in dry Ar and O_2, respectively, indicating the generation of protonic conductivity in humid atmospheres. In comparison with the

measurements in the three kinds of humid atmospheres, the protonic conductivity in 5% H_2O - O_2 and 5% H_2O - H_2 decreased with the increasing Dy content, while the protonic conductivity in 5% H_2O - Ar did not change so much. In addition, an interesting phenomenon has been observed in the color of the Dy-doped samples. The Dy-doped samples appeared black after being sintered, but changed to white after the conductivity measurement in 5% H_2O - H_2. The photograph of $BaZr_{0.8}Dy_{0.2}O_{3-\delta}$ is shown in Figure 5.8 for example. And the Dy-doped samples remained black after the conductivity measurement in 5% H_2O - O_2. Empirically, black appearance of perovskite-type oxides probably reminds of electronic conduction, such as $La_{1-x}Sr_xCoO_{3-\delta}$, $La_{1-x}Sr_xCo_{1-y}Fe_yO_{3-\delta}$, $La_{1-x}Sr_xMnO_{3-\delta}$, *etc*. However, significant electronic conductivity was not observed for BZDY.
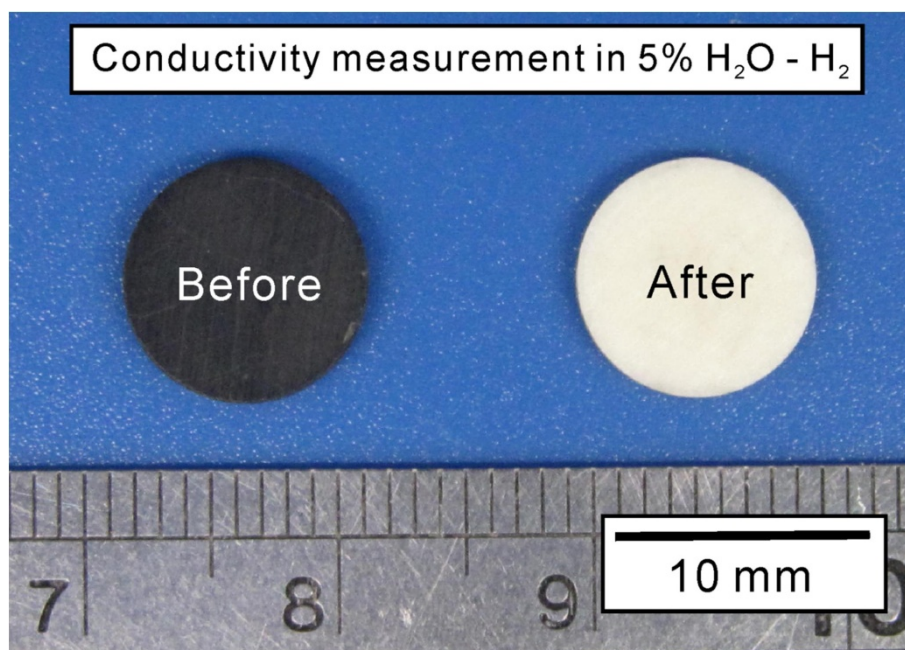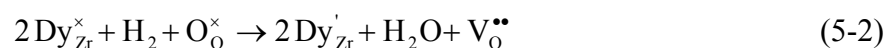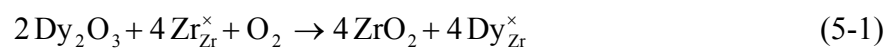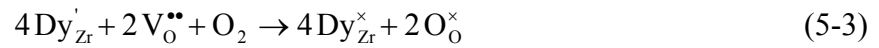

Figure 5.8 Photograph of the pellet of $BaZr_{0.8}Dy_{0.2}O_{3-\delta}$. The color of the as-sintered pellet was black, and changed to white after the conductivity measurement in 5% H_2O - H_2.

5.4 Discussion

Referring to the decreasing lattice volume of as-sintered samples with the increasing Dy content, it is rather contradictory if all the Dy cations in the sintered BZDY are trivalent, since

lattice volume is expected to expand by introducing more Dy due to the larger six-coordinated radius of the Dy(III) cation (0.912 Å [76Sha]) than that of the Y(III) cation (0.900 Å [76Sha]), based on Vegard's Law.   There are two possible explanations for this abnormal phenomenon. One is that although Dy and Y are mainly of B-site occupation, a partial amount of the dopant cations occupy A-site with different contents.   Since the twelve-fold coordinated radii of the cations of Dy(III) (1.255 Å [09Par]) and Y(III) (1.234 Å [09Par]) are smaller than that of Ba(II) (1.610 Å [76Sha]), substituting the Ba(II) cations will consequently induce the lattice volume shrinkage.   As illustrated in Chapter 2 and 3, no A-site occupation of Y was confirmed by Rietveld refinement for analyzing the diffraction pattern of nominally stochiometric $BaZr_{0.8}Y_{0.2}O_{3-\delta}$, while about 5% of the doped Dy was estimated to occupy A-site of $BaZr_{0.8}Dy_{0.2}O_{3-\delta}$, indicating a relatively large capacity for Dy to occupy A-site compared with Y.   However, such small amount of Dy cations occupying A-site is not expected to sensitively result in a great change in lattice volume.   The other possible explanation is partial existence of tetravalent Dy cations in the oxidizing atmosphere, by which the phenomena of lattice volume variation in Figure 5.4 can be understood.   The reaction of incorporation of Dy(IV) into the B-site of $BaZrO_3$ for sintering in O_2 atmosphere is given as Eq. (5-1).   Since the six-fold coordinated radius of Dy(IV) cation (0.78 Å [74Kno]) is smaller than that of Y(III) cation (0.900 Å [76Sha]), it is reasonable that the lattice volume of BZDY decreases with the increasing Dy content.   When subsequently annealed in H_2, the Dy cations are reduced to trivalent, as given in Eq. (5-2), and the radius of the Dy cation therefore increases to 0.912 Å [76Sha], by which the lattice volume increased.   When annealed in O_2 again, as expressed in Eq. (5-3), the Dy(III) cations are oxidized to be tetravalent again, and the lattice volume approaches to those of the as-sintered samples.

$$2\,Dy_2O_3 + 4\,Zr_{Zr}^{\times} + O_2 \rightarrow 4\,ZrO_2 + 4\,Dy_{Zr}^{\times} \qquad (5\text{-}1)$$

$$2\,Dy_{Zr}^{\times} + H_2 + O_O^{\times} \rightarrow 2\,Dy_{Zr}^{'} + H_2O + V_O^{\bullet\bullet} \qquad (5\text{-}2)$$

$$4\,\mathrm{Dy}'_{\mathrm{Zr}} + 2\,\mathrm{V}_{\mathrm{O}}^{\bullet\bullet} + \mathrm{O}_2 \rightarrow 4\,\mathrm{Dy}_{\mathrm{Zr}}^{\times} + 2\,\mathrm{O}_{\mathrm{O}}^{\times} \tag{5-3}$$

After being annealed in H_2 at 600 $^{\circ}$C for 72 h, the Dy cations in BZDY are considered to be of trivalent, whose radius is slightly larger than that of the Y(III) cation. However, increase of lattice volume of the H_2-annealed sample with the increasing Dy content was not clearly observed as expected. This is considered to be attributed to the relatively large capacity for Dy to occupy A-site than Y. The way how lattice volume changes with the increasing Dy content is a combination of the expansion effect by substituting Y(III) cations with larger Dy(III) cations in B-site, and the shrinkage effect by partitioning of Dy(III) cations into A-site where larger Ba(II) cations occupy.

As given in Eq. (5-3), in O_2 atmosphere, with the oxidization of Dy cations from trivalent to tetravalent, oxide ion vacancies, which are essential for introducing protons by dissociative dissolving of water molecules as given in Eq. (1-3), are consumed. Therefore, compared to humid Ar and H_2, lower hydroxide ion concentrations were obtained in humid O_2. Since the conductivity is a function of the carrier concentration, low concentration of hydroxide ions causes poor protonic conductivity, therefore, lower bulk conductivity was observed in the humid O_2 atmosphere, compared to the measurements performed in humid Ar and H_2.

5.5 Conclusions

(1) Single phase of BZDY was obtained by conventional solid state reaction method. After being sintered at 1600 $^{\circ}$C, all the samples exhibited dense cross-section morphology.

(2) The lattice volume of the as-sintered BZDY decreased with the increasing Dy content. After being annealed in the H_2 atmosphere, the difference in lattice volume of the samples with various compositions became small.

(3) The concentrations of hydroxide ions per unit cell of all the Dy-doped samples were

higher when hydrated in humidified Ar, compared with those hydrated in humid O_2. And the bulk conductivities of BZDY measured in humid Ar were therefore higher than that in humid O_2. The highest bulk conductivities were obtained for the measurement in humid H_2. (4) These phenomenon strongly implied that a partial amount of Dy cations existed as tetravalent in $BaZrO_3$.

References

[74Kno] O. Knop, J. Carlow, *Can. J. Chem*. 52 (1974) 2175-2183.

[76Sha] R.D. Shannon, *Acta Crystallogr. A* 32 (1976) 751-767.

[80Bra] V.G. Brauer, H. Kristen, *Z. Anorg. Allg. Chem*. 462 (1980) 35-41.

[85Miz] J. Mizusaki, M. Yoshihiro, S. Yamauchi, K. Fueki, *J. Solid State Chem*. 58 (1985) 257-266.

[86Ger] R. Gerhardt, A.S. Nowick, *J. Am. Ceram. Soc*. 69 (1986) 641-646.

[87Sod] L. Soderholm, L.R. Morss, M.F. Mohar, *J. Less-Common Mel*. 127 (1987) 131-135.

[89Miz] J. Mizusaki, Y. Mima, S. Yamauchi, K. Fueki, *J. Solid State Chem*. 80 (1989) 102-111.

[91Miz] J. Mizusaki, H. Tagawa, K. Naraya, T. Sasamoto, *Solid State Ionics* 49 (1991) 111-118.

[95Tai] L.T. Tai, M.M. Nasrallah, H.U. Anderson, D.M. Sparlin, S.R. Sehlin, *Solid State Ionics* 76 (1995) 273-283.

[99Dus] V. Dusastre, J.A. Kilner, *Solid State Ionics* 126 (1999) 163-174.

[08Ima] S. Imashuku, T. Uda, Y. Nose, K. Kishida, S. Harada, H. Inui, Y. Awakura, J. Electrochem. Soc. 155 (2008) B581-B586.

[09Par] K. Park, C. Kim, Y. Yoon, S. Song, Y. Kim, K. Hur, *J. Eur. Ceram. Soc*. 29 (2009) 1735-1741.
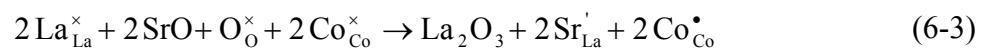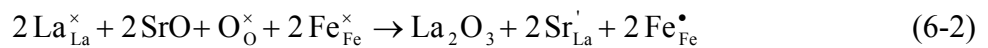
Chapter 6

Preparation of $La_{1-x}Sr_xSc_{1-y}Fe_yO_{3-\delta}$ (LSSF) Aiming Mixed Protonic and Electronic Conductive Cathode for PCFCs

6.1 Introduction

As illustrated in Chapter 1, several perovskite-type oxides with remarkably high electronic conductivity under oxidizing atmosphere were attempted for the application as cathode in PCFCs, such as $La_{1-x}Sr_xCoO_{3-\delta}$ (LSC) [04Maf], $La_{1-x}Sr_xFeO_{3-\delta}$ (LSF) [05Yam], $La_{1-x}Sr_xCo_{1-y}Fe_yO_{3-\delta}$ (LSCF) [08Epi], *etc*. In these materials, there are two ways for the system to maintain electroneutrality when divalent Sr cations are introduced to substitute trivalent La cations. One is by generating oxide ion vacancies, as given in Eq. (6-1).

$$2\,La_{La}^{\times} + 2\,SrO + O_O^{\times} \rightarrow La_2O_3 + 2\,Sr_{La}^{'} + V_O^{\bullet\bullet} \tag{6-1}$$

The other is by oxidizing the conventionally trivalent Fe and Co cations to tetravalent, as given in Eq. (6-2) and (6-3).

$$2\,La_{La}^{\times} + 2\,SrO + O_O^{\times} + 2\,Fe_{Fe}^{\times} \rightarrow La_2O_3 + 2\,Sr_{La}^{'} + 2\,Fe_{Fe}^{\bullet} \tag{6-2}$$

$$2\,La_{La}^{\times} + 2\,SrO + O_O^{\times} + 2\,Co_{Co}^{\times} \rightarrow La_2O_3 + 2\,Sr_{La}^{'} + 2\,Co_{Co}^{\bullet} \tag{6-3}$$

By hopping of electrons among the cations of different valence states, LSC, LSF and LSCF exhibit high electronic conductivities. [83Miz, 85Miz, 89Miz, 92Miz, 95Ta1, 95Ta2]

However, the ideal cathode material for PCFCs is expected to be mixed protonic and electronic conductive [10Fab], therefore, the whole interface between cathode and gas phase is also reactive site for the cathode reaction, as given in Eq. (1-5). In addition, $La_{1-x}Sr_xScO_{3-\delta}$ (LSS) is reported to be a proton conductor [97Nom, 99Lyb, 02Nom], which exhibits about 4.6×10^{-3} Scm^{-1} at $600^{\circ}C$ [06Liu]. Therefore, considering the mechanism for the electronic conductivity in LSF, if Fe can be introduced into the Sc site of LSC, the resulting new compound of $La_{1-x}Sr_xSc_{1-y}Fe_yO_{3-\delta}$ (LSSF) would possibly exhibit a mixed protonic and
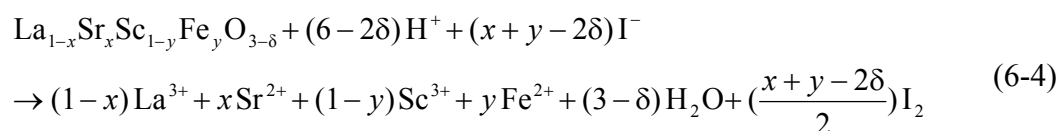
electronic conductivity.

6.2 Experimental

Samples were fabricated by conventional solid state reaction.   The starting materials were prepared by mixing La_2O_3, $SrCO_3$, Sc_2O_3 and Fe_2O_3 powders for LSSF, La_2O_3, $SrCO_3$ and Co_3O_4 powders for LSC, La_2O_3, $SrCO_3$, Co_3O_4 and Fe_2O_3 powders for LSCF, at the desired ratios.   After ball-milling for 24 h, the mixtures were pressed into pellets under 9.8 MPa and heated at 1000 ^{o}C for 10 h.   The samples were then ball-milled for 10 h, and pressed into pellets under 9.8 MPa again, followed by a subsequent heat treatment for 10 h, at 1300 ^{o}C for LSSF, and 1000 ^{o}C for LSC and LSCF.   The process of the ball-milling for 10 h and heat treatment at 1300 ^{o}C / 1000 ^{o}C for 10 h was repeated for three times at most, in order to acquire a single phase confirmed by XRD analysis.   After that, the samples were ball-milled for 10 h and mixed with an organic binder solution consisting of water, polyvinyl alcohol, glycerin and ethanol.   The mixtures were then pressed into pellets at 392 MPa, followed by a subsequent heat treatment at 600 ^{o}C for 8 h to remove the binder solution. Finally, the pellets were sintered for 24 h at 1500 ^{o}C for LSSF, and 1300 ^{o}C for LSC and LSCF.

Water contents of the hydrated samples were measured by Karl-Fischer titration method as illustrated in Chapter 2.   In the present work, samples with the size of 2 mm in length which were broken from the sintered pellets were adopted to hydrate at 300 ^{o}C for 48 h in humid atmosphere of 5% H_2O - 19% O_2 - Ar.   Conductivities were measured by a.c. 2-terminal method as described in Chapter 5.   In this work, silver paste (Fujikura Kasei) was painted on both surfaces of the pellets as electrodes.   And the conductivity measurements were performed in the atmosphere of 5% H_2O - 19% O_2 - Ar.

Nonstoichiometries of oxide ions (δ) in the LSSF samples were determined by classical titration method [50Jon, 53Jon]. About 30 mg of the LSSF sample and sufficient amount of solid KI were dissolved in 1M HNO_3 solution in a sealed glass tube. Before being sealed, the glass tube was filled with N_2 gas to avoid undesired oxidation of I^- anions by O_2 gas in air. The total reaction is given in Eq. (6-4). In the reaction, I^- anions are oxidized to I_2, and Fe^{3+} and Fe^{4+} cations in the LSSF samples are reduced to Fe^{2+} cations. Then, by titrating the generated I_2 with 0.1 M $Na_2S_2O_3$ solution, the nonstoichiometries of oxide ions in the LSSF samples were determined.

$$La_{1-x}Sr_xSc_{1-y}Fe_yO_{3-\delta} + (6-2\delta)H^+ + (x+y-2\delta)I^-$$
$$\rightarrow (1-x)La^{3+} + xSr^{2+} + (1-y)Sc^{3+} + yFe^{2+} + (3-\delta)H_2O + (\frac{x+y-2\delta}{2})I_2 \qquad (6-4)$$

6.3 Results and Discussion

6.3.1 Structure Identifications of LSC, LSCF and LSSF

Crystallographic structures of the prepared LSC samples were identified as rhombohedral with the Sr contents between 0.1 and 0.5, and as cubic with the Sr contents of 0.6 and 0.7. The structures of the prepared $La_{0.6}Sr_{0.4}Co_{1-y}Fe_yO_{3-\delta}$ samples were identified as rhombohedral regardless of the Sr contents. The results of the preparation of LSSF are summarized in Figure 6.1. In the figure, the abscissa and ordinate represent the compositions of the cations in A and B-sites in $La_{1-x}Sr_xSc_{1-y}Fe_yO_{3-\delta}$ by showing the ratios of the Sr and Fe contents, respectively. And the filled circles indicate the samples with a single phase of perovskite-type structure obtained after the heat treatment at 1300 ^{o}C. The filled inverted-triangles indicate that the samples were not of single phase after the heat treatment at 1300 ^{o}C, but became single phase after being sintered at 1500 ^{o}C. Meanwhile, a few of the prepared samples were not of single phase either after being heat-treated at 1300 ^{o}C or after

the subsequent sintering at 1500 ^{o}C, as indicated by cross symbols.   It can be concluded that single phase LSSF could be prepared in a wide composition range.
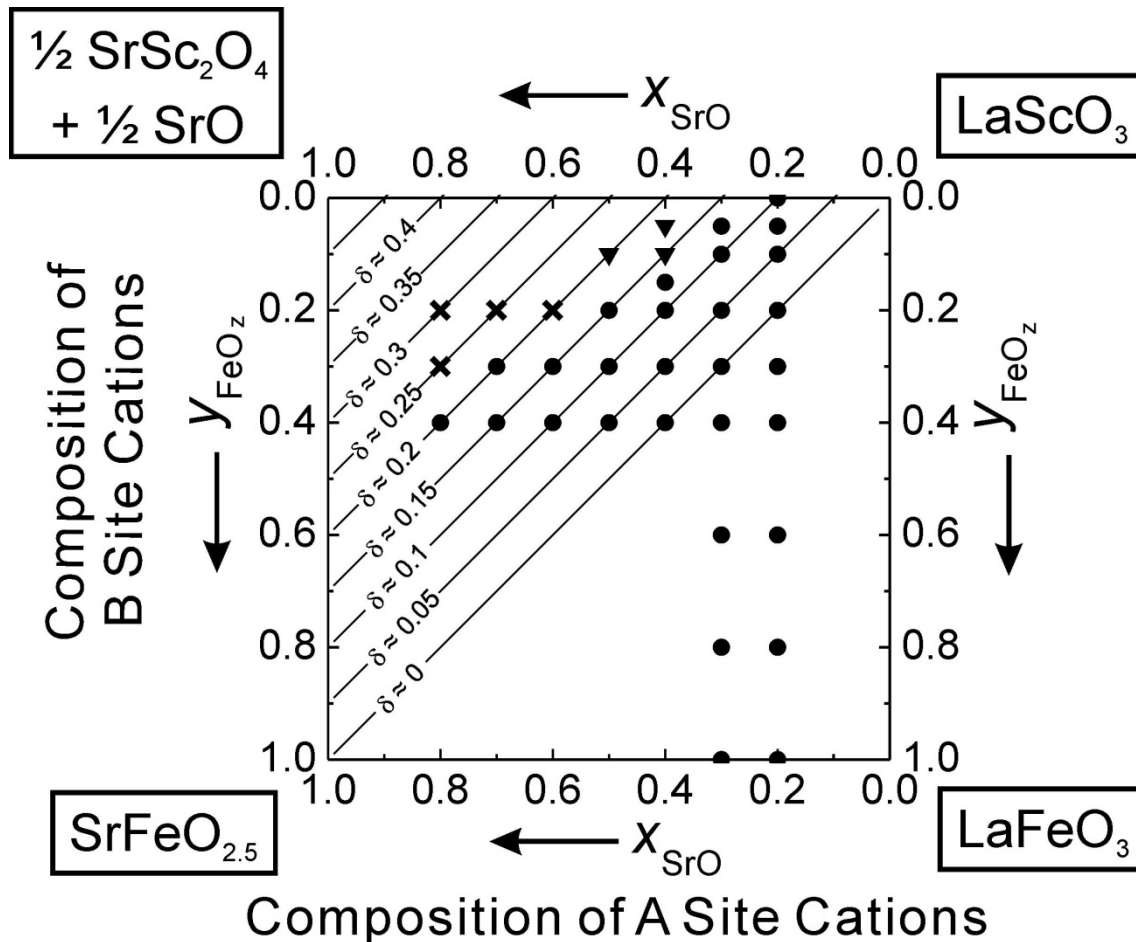

Figure 6.1 La_2O_3 - SrO - Fe_2O_3 - Sc_2O_3 tetragonal composition diagram.   ●: Perovskite-type single phase was acquired after the thermal treatment at 1300 ^{o}C, ▼: Perovskite-type single phase was acquired after the sintering at 1500 ^{o}C, ✗: Single phase was not acquired either after the thermal treatment at 1300 ^{o}C or after the sintering at 1500 ^{o}C.   Isoconcentration lines of oxide ion vacancies are drawn based on the assumption of predomination of Fe(IV) cations.

Since for perovskite-type oxides, protons are introduced by dissociative dissolving of water molecules into the oxide ion vacancies in the material, which implies that the higher the concentration of oxide ion vacancies contained in the sample, the larger the amount of protons would be introduced in humid atmosphere.   Thus, it is meaningful to determine the concentration of the oxide ion vacancies, namely, the nonstoichiometry of oxide ions (δ), in

the samples before hydration.   Since the Fe(III) cations in B site of perovskite-type oxides tend to be oxidized to Fe(IV) cations in atmospheric air, it is assumed here that after doping Sr into A site, Fe(IV) cations form prior to that of oxide ion vacancies for charge compensation.   For the LSSF samples where the Sr content is larger than the Fe content, all the Fe cations are assumed to be tetravalent.   Based on this assumption, the δ for LSSF can be estimated from Eq. (6-5).   The isoconcentration lines of oxide ion vacancies are drawn in Figure 6.1, indicating that the samples having higher Sr contents and lower Fe contents contain higher concentrations of oxide ion vacancies, offering a considerably greater possibility of introducing hydroxide ions by hydration.

$$\delta = \frac{x - y}{2} \qquad (6\text{-}5)$$

Structures of the LSSF samples with different compositions were identified as cubic, orthorhombic and rhombohedral.   The XRD patterns of the samples of $La_{0.8}Sr_{0.2}Sc_{1-y}Fe_yO_{3-\delta}$ with the Fe content varying from 0 to 1 are shown in Figure 6.2 for example, and only the shifts of peak positions were observed.   Since the structures of $La_{0.8}Sr_{0.2}ScO_{2.9}$ and $La_{0.8}Sr_{0.2}FeO_{3-\delta}$ can be identified as orthorhombic by comparing with the JCPDS cards of $LaScO_3$ (JCPDS 00-026-1148) and $LaFeO_3$ (JCPDS 01-088-0641), respectively, it is considered to be reasonable that the structures of the $La_{0.8}Sr_{0.2}Sc_{1-y}Fe_yO_{3-\delta}$ samples with the Fe content varying from 0 to 1 are also orthorhombic.   It was also observed that with the increase of the Sr content, the structure of the samples transferred from orthorhombic to cubic. For example, $La_{1-x}Sr_xSc_{0.6}Fe_{0.4}O_{3-\delta}$ with $x = 0.2$, 0.3 and 0.4 have orthorhombic structures, but when $x > 0.5$, cubic LSSF was identified.   This phenomenon can be explained by using the tolerance factor given in Eq. (1-1).   The tolerance factors of LSSF calculated from the Shannon radii [76Sha] are plotted in Figure 6.3.   With the increasing Sr content, the tolerance factor increased and approached to 1.   Since the ideal perovskite is a cubic structure with the tolerance factor of 1 [29], approaching of the tolerance factor to 1 implies an improvement in

structural symmetry of LSSF, which was observed as the change of structure to cubic in the present work.
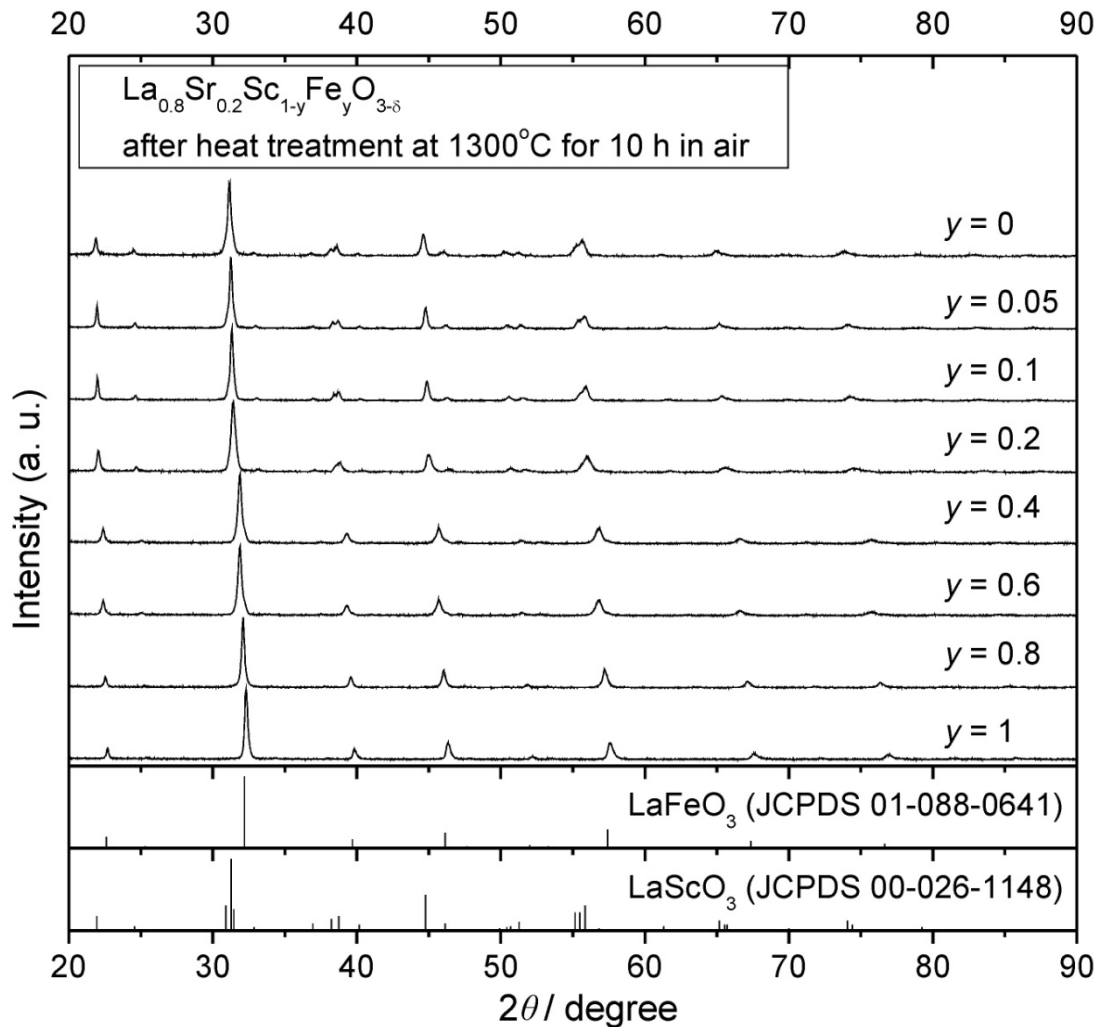

Figure 6.2 XRD patterns of $La_{0.8}Sr_{0.2}Sc_{1-y}Fe_yO_{3-\delta}$ (y = 0, 0.05, 0.1, 0.2, 0.4, 0.6, 0.8 and 1) after the heat treatment at 1300 ^oC for 10 h in air.

The lattice volumes of LSSF and LSCF as a function of the Fe content are shown in Figure 6.4. The lattice volume of LSCF increased, while the lattice volume of LSSF decreased clearly with the increasing Fe content. This is because the radii of Fe(IV) cation (0.585 Å [76Sha]) and Fe(III) cation (0.55 Å [76Sha]) are larger than those of Co(IV) cation (0.53 Å [76Sha]) and Co(III) cation (0.545 Å [76Sha]), but smaller than that of Sc(III) cation (0.745 Å [76Sha]). The lattice volumes of LSSF and LSC as a function of the Sr content are shown in

Figure 6.5. Since the radius of Sr(II) cation (1.44 Å [76Sha]) is close to that of La(III) cation (1.36 Å [76Sha]), there was no significant change in the lattice volume with the increase of the Sr content for both the LSSF and LSC.
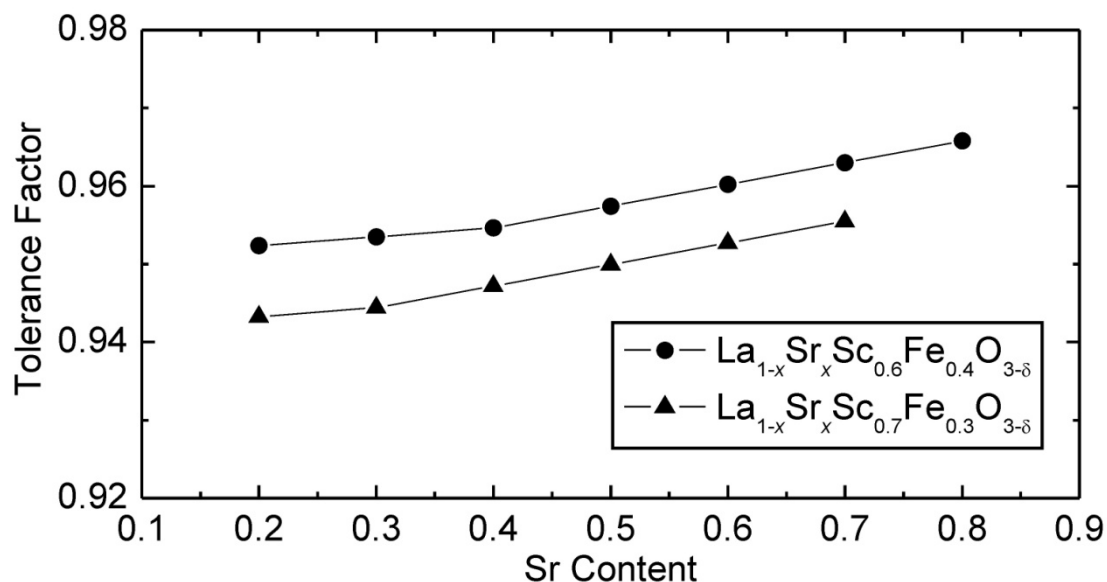
Figure 6.3 Tolerance factors of $La_{1-x}Sr_xSc_{1-y}Fe_yO_{3-\delta}$ (y = 0.3, 0.4) as a function of the Sr content.
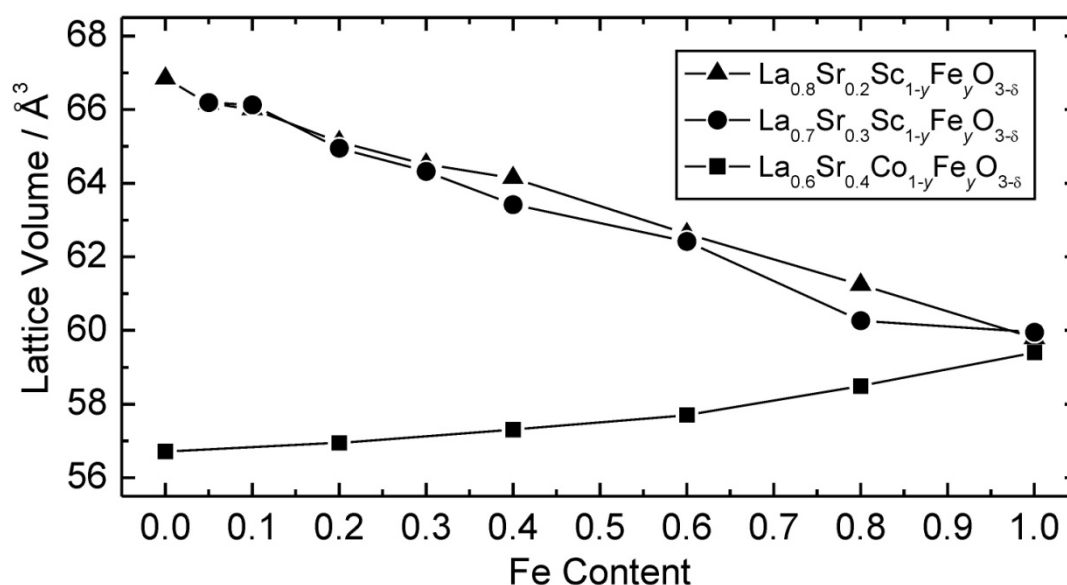
Figure 6.4 Lattice volumes of $La_{1-x}Sr_xSc_{1-y}Fe_yO_{3-\delta}$ (x = 0.2, 0.3) and $La_{0.6}Sr_{0.4}Co_{1-y}Fe_yO_{3-\delta}$ as a function of the Fe content. The LSSF and LSCF samples were obtained after the sintering at 1500 ^{o}C and 1300 ^{o}C, respectively.
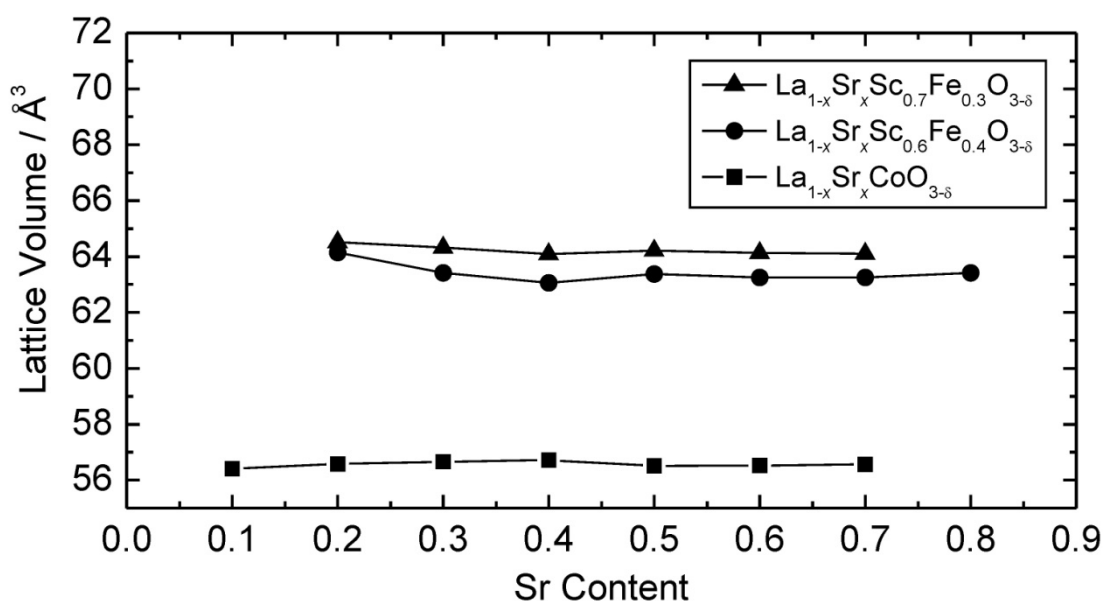
Figure 6.5 Lattice volumes of $La_{1-x}Sr_xSc_{1-y}Fe_yO_{3-\delta}$ (y = 0.3, 0.4) and $La_{1-x}Sr_xCoO_{3-\delta}$ as a function of the Sr content.　The LSSF and LSC samples were obtained after the sintering at 1500 ^{o}C and 1300 ^{o}C, respectively.

6.3.2 Hydration Behaviors of LSC, LSCF and LSSF

(a) LSCF

　　The measured water contents and concentrations of hydroxide ions per unit cell of the $La_{0.6}Sr_{0.4}Co_{1-y}Fe_yO_{3-\delta}$ samples are shown in Figure 6.6.　The concentrations of hydroxide ions per unit cell for all the samples were less than 2.6×10^{-3}.　Since the protonic conductivity of perovskite-type oxides is generated by the moving of protons, which are introduced into the oxides in the form of hydroxide ions by dissolving of water as given in Eq. (1-3), a great dependence of the protonic conductivity on the concentration of hydroxide ions is implied. Therefore, such low concentrations of hydroxide ions in the LSCF samples may indicate their negligible protonic conductivities.
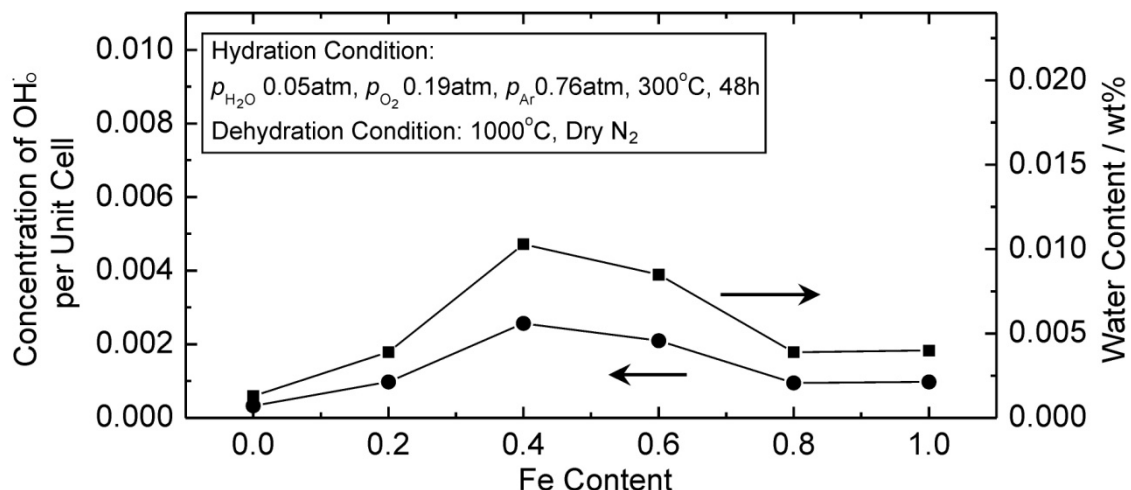
Figure 6.6 Water content and concentration of hydroxide ions per unit cell of $La_{0.6}Sr_{0.4}Co_{1-y}Fe_yO_{3-\delta}$ as a function of the Fe content. The measured samples were about 2 mm in length, broken from pellets sintered at 1300 ^oC.

(b) LSC

As shown in Figure 6.7, the concentrations of hydroxide ions per unit cell of the LSC samples were less than 3.0×10^{-3}, and thus the protonic conductivity of LSC was also considered to be negligible. Meanwhile, when the Sr contents of the LSC samples were less than 0.4, the concentration of the hydroxide ions were of a lower magnitude. When the Sr content increased from 0.4 to 0.6, the concentration of hydroxide ions increased slightly. Comparing with the nonstoichiometry of oxide ions of LSC measured at 300^oC in air reported by Mizusaki *et al*. [89Miz], a certain degree of similarity exists between the two profiles, which implies the dependence of introduction of hydroxide ions on the concentration of oxide ion vacancies. This is because the increase of the Sr content of LSC directly results in an increase of the concentration of oxide ion vacancies.
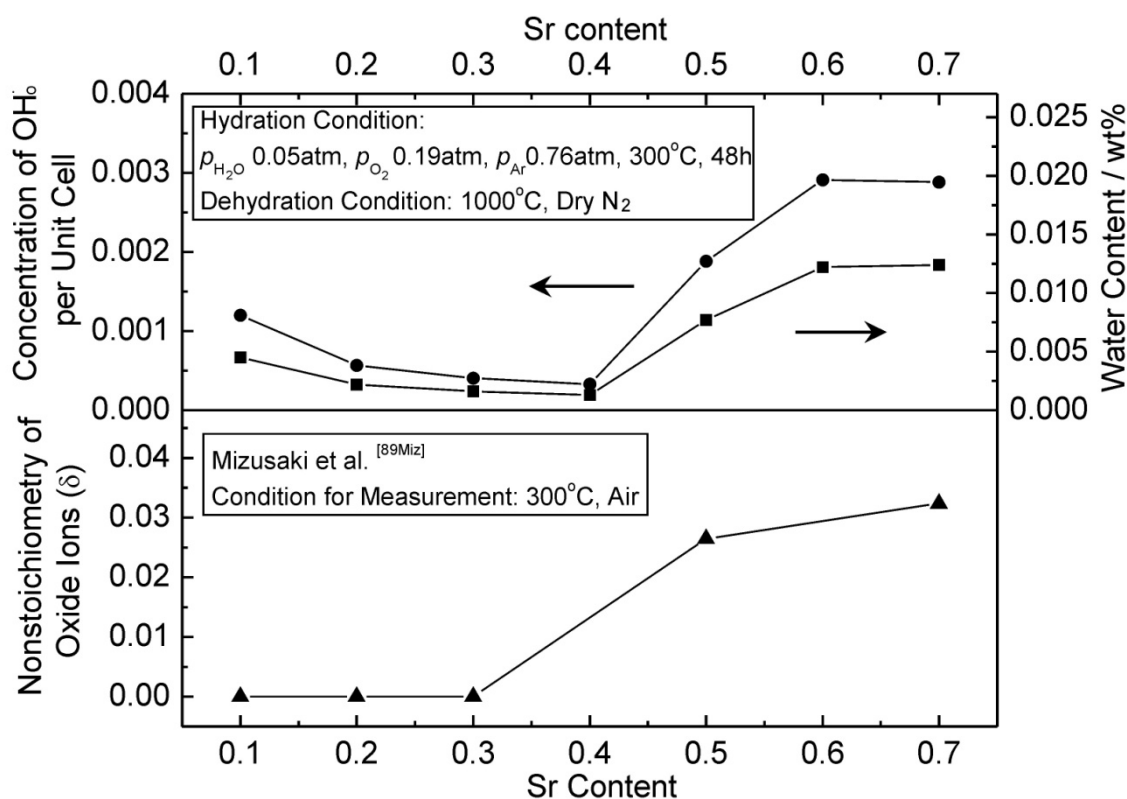
Figure 6.7 Water content and the concentration of hydroxide ions per unit cell of $La_{1-x}Sr_xCoO_{3-\delta}$ as a function of the Sr content. The measured samples were of the size about 2 mm in length, broken from pellets sintered at 1300 ^{o}C. The reported nonstoichiometry of oxide ions in LSC [89Miz] is plotted for comparison.

(c) LSSF

The results of the measurement of water contents of LSSF samples are plotted three-dimensionally in Figure 6.8. The concentration of the hydroxide ions varied dramatically with the variation of composition. When the Fe content was constant, the concentration of hydroxide ions increased with the increasing Sr content. Meanwhile, when the Sr content was constant, the concentration of hydroxide ions decreased with the increasing Fe content. And as shown in Figure 6.1, when the Sr content or Fe content is kept constant, the oxide ion vacancies increases with the decreasing Fe content or increasing Sr content, respectively. Since the hydroxide ions are introduced by dissolving water into the oxide ion vacancies, the observed tendency can be related to the increase or decrease of the

concentration of oxide ion vacancies.   However, there was no linear relationship between the concentrations of hydroxide ions and oxide ion vacancies.   For example, the concentration of hydroxide ions per unit cell of $La_{0.8}Sr_{0.2}ScO_{3-\delta}$ is as high as 1.32×10^{-1}, but by introducing just a small amount of Fe, $y = 0.05$, a dramatic drop in the concentration of hydroxide ions can be observed, to the value of 2.60×10^{-2}.   The effect of the Fe content is also evident, as seen in Figure 6.9 by comparing the concentration of hydroxide ions of the LSSF samples whose compositions are on the isoconcentration lines of oxide ion vacancies.   Understanding this interesting phenomenon is not quite easy.   Empirically, introduction of a small amount of Fe cations causes a large change of the chemical properties of oxide ions and oxide ion vacancies, that is, the hydration enthalpy increases greatly.
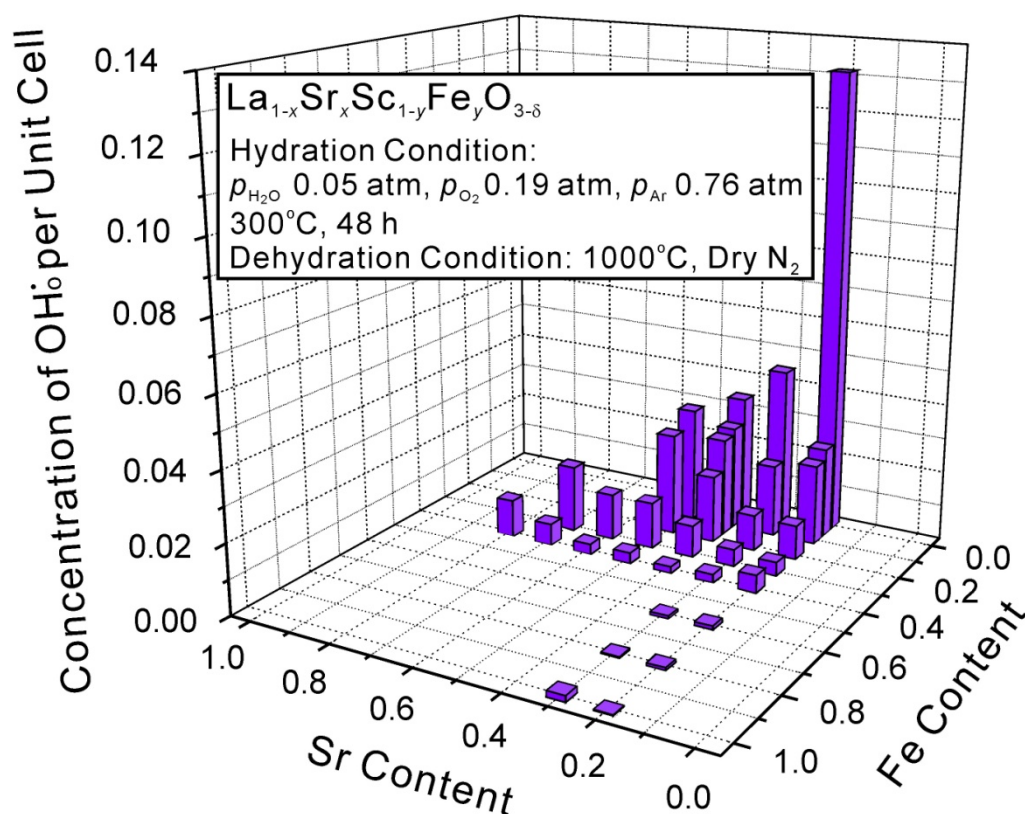

Figure 6.8 Three-dimensional plots of the concentration of hydroxide ions per unit cell of LSSF.   The measured samples were of the size about 2 mm in length, broken from pellets sintered at 1500 $^{\circ}$C.
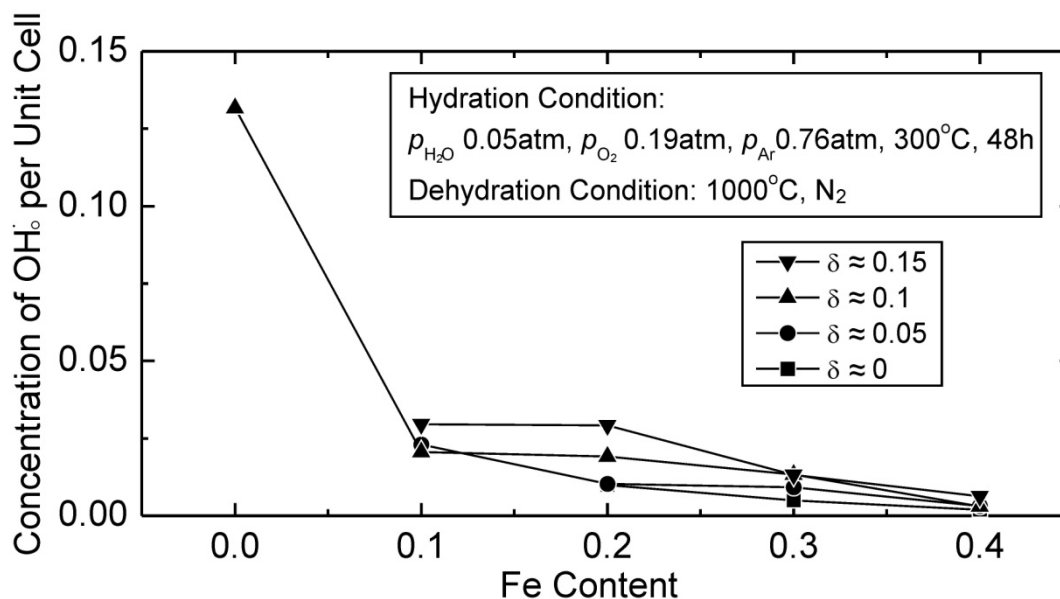
Figure 6.9 Concentration of hydroxide ions per unit cell of LSSF with the compositions on the isoconcentration lines of oxide ion vacancies as a function of Fe content. The isoconcentration lines of oxide ion vacancies are drawn based on the assumption of predomination of Fe(IV) cations as shown in Figure 6.1.

6.3.3 Nonstoichiometry of Oxide Ions by Titration

The plotted isoconcentration lines of oxide ion vacancies are based on the assumption that all the Fe cations in the LSSF samples, which contain more Sr cations than Fe cations, are tetravalent. However, there might be a certain amount of Fe(III) cations coexisting with the Fe(IV) cations in reality, which implies the possibility of deviation of the real values of δ from the assumed ones. In order to check whether such assumption is reasonable, nonstoichiometry of oxide ions (δ) with the compositions on the isoconcentration lines of oxide ion vacancies were confirmed by the titration method. The results are shown in Figure 6.10. As can be seen, the measured values of δ for the samples with the compositions on the isoconcentration lines of δ with the values of 0.05 and 0.1 were close to the assumed values, indicating the predomination of Fe(IV) cations in these LSSF samples. On the other hand, the δ measured for the samples with the compositions on the isoconcentration lines of δ with

the values of 0 and 0.15 were greater than the value estimated, indicating that significant amounts of the Fe(III) cations were coexistent with the Fe(IV) cations. Thus, the assumption is valid in the cases of isoconcentration lines of δ of 0.05 and 0.1. Small refinements might be needed in the case of δ of 0 and 0.15, but these are tolerable deviations.
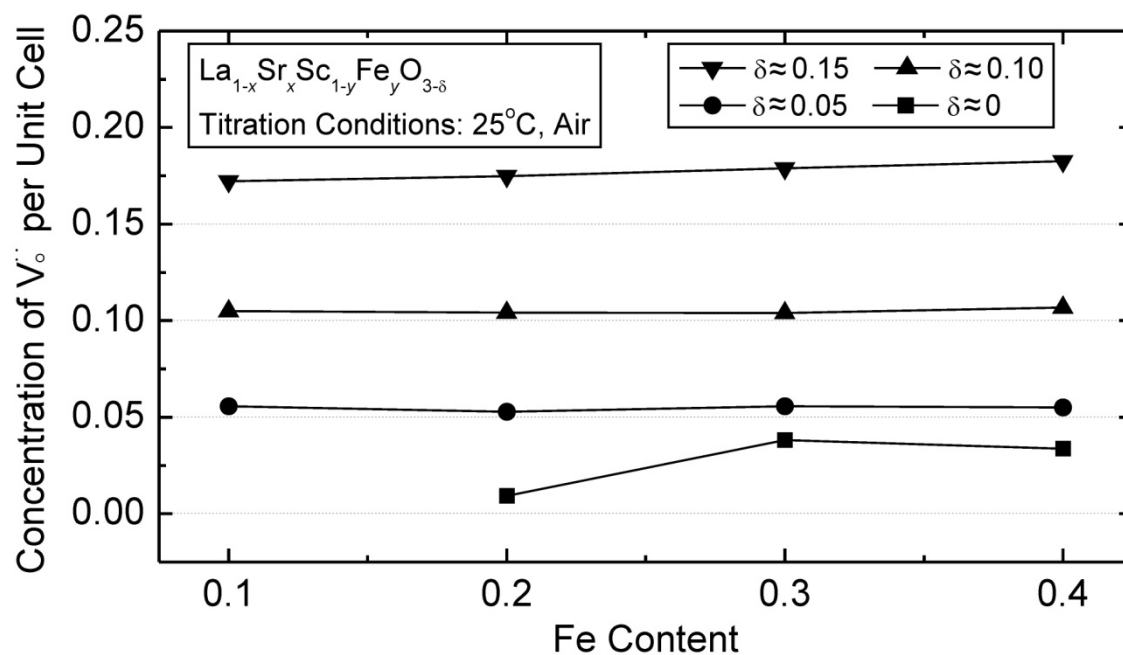

Figure 6.10 Concentration of the oxide ion vacancies of LSSF as a function of the Fe content by the titration method.

6.3.4 Conductivity of LSSF

The conductivities were measured for the LSSF samples ($La_{0.8}Sr_{0.2}Sc_{0.95}Fe_{0.05}O_{3-\delta}$, $La_{0.7}Sr_{0.3}Sc_{0.95}Fe_{0.05}O_{3-\delta}$, $La_{0.8}Sr_{0.2}Sc_{0.9}Fe_{0.1}O_{3-\delta}$, $La_{0.7}Sr_{0.3}Sc_{0.9}Fe_{0.1}O_{3-\delta}$, $La_{0.5}Sr_{0.5}Sc_{0.8}Fe_{0.2}O_{3-\delta}$ and $La_{0.3}Sr_{0.7}Sc_{0.7}Fe_{0.3}O_{3-\delta}$) which were confirmed to have relatively high concentrations of hydroxide ions, as shown in Figure 6.11. For the samples of $La_{0.8}Sr_{0.2}Sc_{0.95}Fe_{0.05}O_{3-\delta}$, $La_{0.8}Sr_{0.2}Sc_{0.9}Fe_{0.1}O_{3-\delta}$, $La_{0.7}Sr_{0.3}Sc_{0.95}Fe_{0.05}O_{3-\delta}$, the bulk conductivities and grain boundary conductivities were identified by analyzing the impedance spectra. While for the other samples, only the bulk conductivities were identified. The conductivities of all the examined

samples were close to each other and to the total conductivity of $La_{0.97}Sr_{0.03}ScO_{3-\delta}$ single crystal reported by Liu *et al.* [06Liu], while about two orders of magnitude less than the total conductivity of $La_{0.7}Sr_{0.3}FeO_{3-\delta}$ reported by Yamamoto *et al.* [87Yam]. It is generally accepted that an ideal cathode material for fuel cells should possess high electronic conductivity (~100 S cm^{-1}) and ionic conductivity close to that of the electrolyte material [01Ste, 02Sim]. From this point of view, LSSF may not be a promising mixed protonic and electronic conductor for the application as a cathode material in PCFCs.
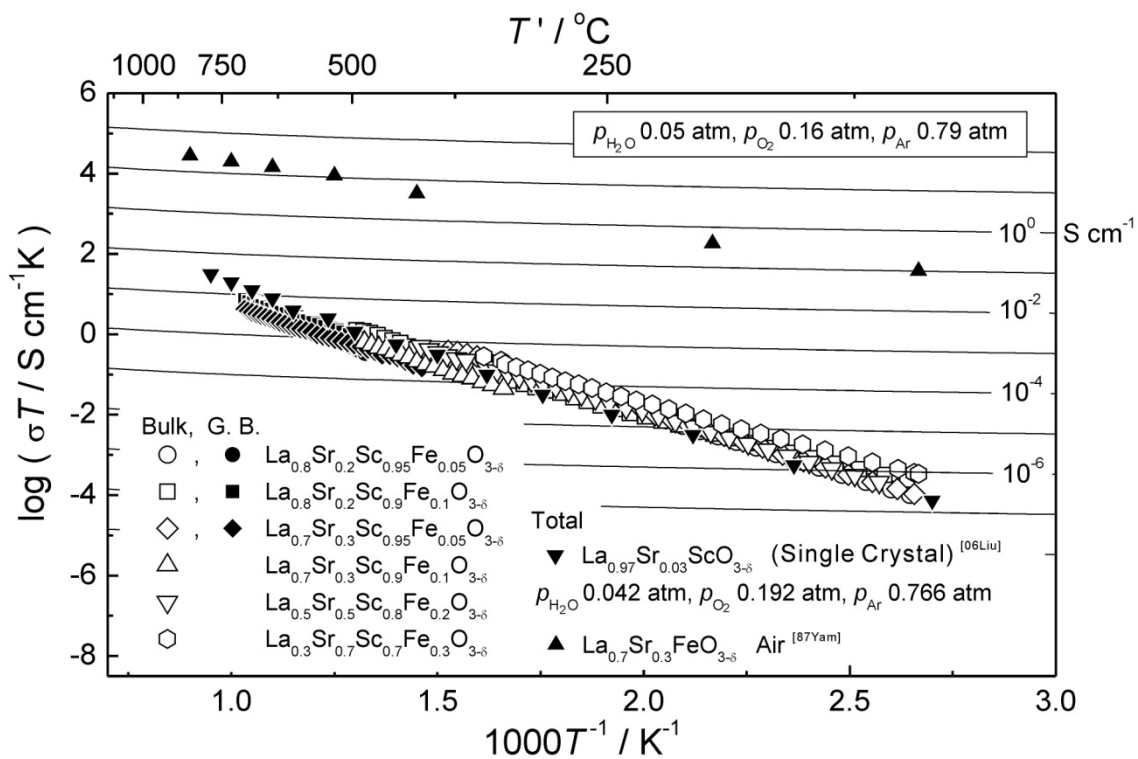

Figure 6.11 Conductivities of LSSF with relatively high proton concentrations as a function of temperature plotted in the Arrhenius form. For comparison, the reported total conductivities of $La_{0.97}Sr_{0.03}ScO_{3-\delta}$ [06Liu] and $La_{0.7}Sr_{0.3}FeO_{3-\delta}$ [87Yam] are also plotted.

6.4 Conclusions

(1) After being heat-treated at 1300 $^{\circ}$C, and then sintered at 1500 $^{\circ}$C, single phase of LSSF was obtained in a wide composition range.

(2) The concentrations of hydroxide ions in the LSC and LSCF samples hydrated at 300 $^{\circ}$C in the atmosphere of 5% H_2O - 16% O_2 - Ar were quite low.

(3) The concentrations of hydroxide ions in the LSSF samples hydrated at 300 $^{\circ}$C in the atmosphere of 5% H_2O - 16% O_2 - Ar increased with increasing Sr content while keeping the Fe content of the samples constant, and decreased with increasing Fe content while keeping the Sr content constant. Comparing the samples with equal concentrations of oxide ion vacancies, the concentrations of hydroxide ions in the samples decreased with the increasing Fe content, indicating that the Fe content contained in the sample plays an important role in the hydration properties.

(4) The conductivities of the LSSF samples were close to that of LSS, but about two orders lower than that of LSF. Therefore, LSSF is considered probably not to be a promising mixed protonic and electronic conductor for application as a cathode material in PCFCs

References

[50Jon] G.H. Jonker, J.H. van Santen, *Physica* 16 (1950) 337-349.

[53Jon] G.H. Jonker, J.H. van Santen, *Physica* 19 (1953) 120-130.

[76Sha] R.D. Shannon, *Acta Crystallogr. A* 32 (1976) 751-767.

[83Miz] J. Mizusaki, T. Sasamoto, W.R. Cannon, H.K. Bowen, *J. Am. Ceram. Soc.* 66 (1983) 247-252.

[85Miz] J. Mizusaki, M. Yoshihiro, S. Yamauchi, K. Fueki, *J. Solid State Chem.* 58 (1985) 257-266.

[89Miz] J. Mizusaki, Y. Mima, S. Yamauchi, K. Fueki, *J. Solid State Chem.* 80 (1989) 102-111.

[92Miz] J. Mizusaki, M. Okayasu, S. Yamauchi, K. Fueki, *J. Solid State Chem.* 99 (1992) 166-172.

[95Ta1] L.T. Tai, M.M. Nasrallah, H.U. Anderson, D.M. Sparlin, S.R. Sehlin, *Solid State Ionics* 76 (1995) 259-271.

[95Ta2] L.T. Tai, M.M. Nasrallah, H.U. Anderson, D.M. Sparlin, S.R. Sehlin, *Solid State Ionics* 76 (1995) 273-283.

[97Nom] K. Nomura, S. Tanase, *Solid State Ionics* 98 (1997) 229-236.

[99Lyb] D. Lybye, N. Bonanos, *Solid State Ionics* 125 (1999) 339-344.

[99Hya] H. Hayashi, H. Inaba, M. Matsuyama, N.G. Lan, M. Dokiya, H. Tagawa, *Solid State Ionics* 122 (1999) 1-15.

[01Ste] B.C.H. Steele, A. Heinzel, *Nature* 414 (2001) 345-352.

[02Nom] K. Nomura, T. Takeuchi, S. Tanase, H. Kageyama, K. Tanimoto, Y. Miyazaki, *Solid State Ionics* 154-155 (2002) 647-651.

[02Sim] S.P. Simner, J.F. Bonnett, N.L. Canfield, K.D. Meinhardt, V.L. Sprenkle, J.W. Stevenson, *Electrochem. Solid St.* 5 (2002) A173-A175.

[04Maf] N. Maffei, L. Pelletier, A. McFarlan, *J. Power Sources* 136 (2004) 24-29.

[05Yam] H. Yamamura, T. Ikuta, H. Yahiro, G. Okada, *Solid State Ionics* 176 (2005) 269-274.

[06Liu] J. Liu, Y. Chiba, J. Kawamura, H. Yugami, *Solid State Ionics* 177 (2006) 2329-2332.

[08Epi] A.D'Epifanio, E. Fabbri, E. Di Bartolomeo, S. Licoccia, E. Traversa, *Fuel Cells* 1 (2008) 69-76.

[10Fab] E. Fabbri, D. Pergolesi, E. Traversa, *Sci. Technol. Adv. Mater.* 11 (2010) 044301.

Chapter 7

Summary

Dopant cations play important roles in conduction properties of perovskite-type oxides. The generation of protonic conductivity in $BaZrO_3$ is based on occupation of trivalent cations in B-site to substitute tetravalent Zr cations, and oxide ion vacancies are generated consequently for charge compensation. Since the mechanism of proton introduction in perovskite-type oxides can be expressed in brief as dissociative dissolving of water molecules into oxide ion vacancies, the B-site occupation of trivalent dopant cations benefits the protonic conductivity. Meanwhile, if the trivalent dopant cations partition into A-site to substitute divalent Ba cations, oxide ion vacancies are consumed, and therefore, obstructions occur for the hydration reaction for proton introduction, as well as the generation of protonic conductivity. Hence, clarifying the site occupation of dopant cations in $BaZrO_3$ is meaningful for further increasing the protonic conductivity.

In addition, the mechanism for the electronic conductivity in perovskite-type oxides, such as $La_{1-x}Sr_xFeO_{3-\delta}$ (LSF), $La_{1-x}Sr_xCo_{1-y}Fe_yO_{3-\delta}$ (LSCF), *etc*, is attributed to hopping of electrons among multivalent dopant cations. Thus, in order to develop mixed protonic and electronic conductors for the application as cathode material in protonic ceramic fuel cells (PCFCs), it is essential to investigate the doping behavior when the multivalent dopant cations are introduced into the protonic conductive base materials.

In this dissertation, a systematic investigation of the site occupation of dopants of Sc, Y, Sm, Eu and Dy in $BaZrO_3$ was performed. The atmosphere dependence of valence state of Dy in Y-codoped $BaZrO_3$ (BZDY), and the properties of a new material of $La_{1-x}Sr_xSc_{1-y}Fe_yO_{3-\delta}$ (LSSF) were also investigated as a preliminary step for the further development of mixed protonic and electronic conductors.

Chapter 2

Site occupation of the dopants of Sc, Y, Sm, Eu and Dy was investigated by comparing the lattice volume difference between undoped Ba-rich and B-poor samples with that of the doped samples. The results revealed that for doping Eu or Sm into $BaZrO_3$, not only B-site, but also A-site was occupied by the dopant cations. Therefore, Eu and Sm are considered to be amphoteric dopants for $BaZrO_3$. For doping Sc, Y or Dy into $BaZrO_3$, restricted by the sensitivity of the method applied in this chapter, these dopant cations were only confirmed to mainly occupy B-site. In order to check whether there was small amount of these dopant cations occupying A-site, more sensitive methods were applied as the following works in Chapter 3 and 4. In addition, by evaluating water content contained in hydrated samples, it was observed that the concentrations of hydroxide ions in the Sm and Eu-doped $BaZrO_3$ were greatly lower than those in the Sc and Y-doped samples, regardless of the hydration atmospheres of humid Ar and humid O_2. And the concentration of hydroxide ions in the Dy-doped sample hydrated in humid Ar was obviously higher than that hydrated in humid O_2. Clear dependence of hydration behavior on oxygen partial pressure was only recognized in the Dy-doped sample.

Chapter 3

In order to investigate the site occupation of Y in $BaZrO_3$ more precisely, X-ray diffraction (XRD) pattern was collected by using synchrotron radiation based on anomalous dispersion effect with incident X-ray energies of 17.026 keV and 16.908 keV, close to the Y K absorption edge of 17.037 keV. The samples with the nominal compositions of $Ba_{0.9}Zr_{0.8}Y_{0.2}O_{3-\delta}$ and $BaZr_{0.8}Y_{0.2}O_{3-\delta}$ for measurement by synchrotron radiation were prepared by slow heating process, in which the samples were gradually heated to the sintering temperature of 1600 ^oC at a heating rate of 0.4 $^oCmin^{-1}$. By Rietveld refinement, Y in the

Chapter 7

sample of $BaZr_{0.8}Y_{0.2}O_{3-\delta}$ was evaluated to only occupy B-site.   For the sample of

$Ba_{0.9}Zr_{0.8}Y_{0.2}O_{3-\delta}$, in addition to the precipitation of Y_2O_3, coexistence of two perovskite-type

phases was confirmed.   In one Y-poor phase, all doped Y was evaluated to be of A-site

occupation.   And in the other greatly Y-rich phase, in addition to B-site occupation, a partial

amount of Y was estimated to occupy A-site.   However, a discrepancy between the phase

relationship in the sample prepared by the slow heating process in this work and the reported

BaO - ZrO_2 - $YO_{1.5}$ pseudo-ternary phase diagram was confirmed, which is considered to be

attributed to the route for material preparation.   And therefore, dependence of phase

relationship on preparation method was studied.   The results revealed that for the slow

heating process, in which the samples were gradually heated up to the sintering temperature,

phase relationship of lower temperature is considered to be established preferentially,

obstructing the phase equilibrium at the sintering temperature in desired time.   On the

contrary, during the rapid heating process, in which the samples were inserted directly into the

furnace already kept at the sintering temperature and subsequently quenched to the room

temperature, only the phase relationship at the sintering temperature is expected to be

established.   In addition, periodic planar defects were observed in both the samples

nominally stoichiometric and Ba-deficient by TEM.   And the relatively larger amount of

planar defects existed in the more Ba-deficient sample.

Chapter 4

Site occupation of Sc, Sm, Eu and Dy in $BaZrO_3$ were investigated by utilizing Rietveld

refinement to analyze the XRD patterns collected by synchrotron radiation with the incident

energy of 17.026 keV.   The results revealed that Sc was only of B-site occupation.   And in

addition to the B-site occupation, a small amount of Dy was evaluated to occupy A-site for

the sample with Ba-deficiency of 0.03.   Meanwhile, a relatively larger amount of Sm and Eu

occupying the A-site was evaluated, implying that Sm and Eu are amphoteric dopants for BaZrO$_3$, which is in accordance with the results achieved in Chapter 2.

Chapter 5

In Chapter 2, an interesting phenomenon was observed that for the Dy-doped BaZrO$_3$, higher water content was measured in humid Ar than humid O$_2$, which was considered to be relative to the change in valence state of Dy with atmosphere altering. Therefore, in this chapter, in order to investigate the atmosphere dependence of the valence state of Dy, samples of BaZr$_{0.8}$Dy$_x$Y$_{0.2-x}$O$_{3-\delta}$ (x = 0, 0.05, 0.1, 0.15, 0.2) with perovskite-type single phase were prepared by conventional solid state reaction method. The lattice volumes of the as-sintered BZDY samples decreased with the increasing Dy content. But after being annealed in the H$_2$ atmosphere, the difference in lattice volume of the samples with various compositions became small. Higher values of the concentrations of hydroxide ions per unit cell, and the bulk conductivities of all the Dy-doped samples were obtained in humidified Ar than in humidified O$_2$. The highest bulk conductivities were obtained for the measurement in humid H$_2$. All these phenomena strongly implied that a partial amount of Dy cations existed as tetravalent in BaZrO$_3$ in oxidizing atmosphere.

Chapter 6

In this chapter, an attempt for preparing the mixed protonic and electronic conductor for cathode for PCFCs was performed. The conventional multivalent dopant of Fe was doped into the protonic conductor of La$_{1-x}$Sr$_x$ScO$_{3-\delta}$ (LSS) to prepare a new perovskite-type oxide of La$_{1-x}$Sr$_x$Sc$_{1-y}$Fe$_y$O$_{3-\delta}$ (LSSF). The samples were prepared by solid state reaction method. After being heat-treated at 1300 ^{o}C, and then sintered at 1500 ^{o}C, single phase of LSSF was obtained in a wide composition range. The concentrations of hydroxide ions in the LSSF

samples hydrated at 300 ^{o}C in the atmosphere of 5% H_2O - 16% O_2 - Ar increased with the increasing Sr content while keeping the Fe content of the samples constant, and decreased with the increasing Fe content while keeping the Sr content constant. Comparing the samples with equal concentrations of oxide ion vacancies, the concentrations of hydroxide ions in the samples decreased with the increasing Fe content, indicating that the Fe content in the sample plays an important role in the hydration properties. The conductivities of the LSSF samples were close to that of LSS, but about two orders lower than that of LSF. Therefore, LSSF is considered probably not to be a promising mixed protonic and electronic conductor for application as a cathode material in PCFCs.

List of Publications

Perovskite-type Oxides

Papers

"Synthesis of $La_{1-x}Sr_xSc_{1-y}Fe_yO_{3-\delta}$ (LSSF) and Measurement of Water Content in LSSF, LSCF and LSC Hydrated in Wet Artificial Air at 300^oC"

Donglin HAN, Yusuke OKUMURA, Yoshitaro NOSE, Tetsuya UDA

Solid State Ionics, **181** (35-36) (2010) 1601-1606.

"Site Selectivity of Dopants in $BaZr_{1-y}M_yO_{3-\delta}$ (M = Sc, Y, Sm, Eu, Dy) and Measurement of Their Water Contents, Concentrations of Oxide Ion Vacancies and Conductivities,"

Donglin HAN, Yoshitaro NOSE, Kozo SHINODA, Tetsuya UDA,

Submitted to *Solid State Ionics*.

"Tetravalent Dysprosium in Perovskite $BaZrO_3$"

Donglin HAN, Kozo SHINODA, Yoshitaro NOSE, Tetsuya UDA

Submitted to *Journal of Solid State Chemistry*.

"Evaluation of Site Occupancy of Yttrium in Barium Zirconate by X-ray Diffraction Based on Anomalous Dispersion Effect"

Donglin HAN, Kyosuke KISHIDA, Kozo SHINODA, Yoshitaro NOSE, Haruyuki INUI, Tetsuya UDA

In preparation.

List of Publications

Oral Presentations

International Conference

"Synthesis of $La_{1-x}Sr_xSc_{1-y}Fe_yO_{3-\delta}$ and Measurement of Their Water Contents, Concentration of Oxide Ion Vacancies and Conductivities"

Donglin HAN, Yusuke OKUMURA, Yoshitaro Nose, Tetsuya UDA

Joint Symposium on Materials Science and Engineering for the 21st Century, Daejeon, Korea, June, 2010.

Domestic Conferences in Japan

"Measurement of Water Contents in $La_{1-x}Sr_xCoO_{3-\delta}$, $La_{0.6}Sr_{0.4}Co_{1-y}Fe_yO_{3-\delta}$ and $La_{0.8}Sr_{0.2}Sc_{1-y}Fe_yO_{3-\delta}$"

Donglin HAN, Yusuke OKUMURA, Yoshitaro Nose, Tetsuya UDA

2009 Fall Meeting of the Japan Institute of Metals, Kyoto, September, 2009.

"Measurement of Water Contents and Conductivity of $La_{1-x}Sr_xSc_{1-y}Fe_yO_{3-\delta}$"

Donglin HAN, Yusuke OKUMURA, Yoshitaro NOSE, Tetsuya UDA

The 6th Symposium for Young Researchers and Students of the Kansai Branch of the Mining and Materials Processing Institute of Japan, Kyoto, December, 2009.

"Measurement of Water Contents, Concentration of Oxide Ion Vacancies and Conductivity of $La_{1-x}Sr_xSc_{1-y}Fe_yO_{3-\delta}$ (LSSF)"

Donglin HAN, Yusuke OKUMURA, Yoshitaro NOSE, Tetsuya UDA

2010 Spring Meeting of the Japan Institute of Metals, Tsukuba, March, 2010.

"Site Selectivity of Dopants in $BaZr_{1-x}M_yO_{3-\delta}$ (M = Dy, Eu, Sm) and Measurement of Their Water Contents, Concentrations of Oxide Ion Vacancies and Conductivities"

Donglin HAN, Yoshitaro NOSE, Kozo SHINODA, Tetsuya UDA

2010 Autumn Meeting of the Mining and Materials Processing Institute of Japan, Fukuoka, September, 2010.

"Site Selectivity of Dopants in $BaZr_{1-x}M_yO_{3-\delta}$ (M = Y, Dy, Eu, Sm) and Dependence of Their Water Contents, Concentrations of Oxide Ion Vacancies and Conductivities"

Donglin HAN, Yoshitaro NOSE, Kozo SHINODA, Tetsuya UDA

The 36th Symposium on Solid State Ionics in Japan, Sendai, November, 2010.

Poster Presentations

International Conferences

"Measurement of Water Contents in Hydrated $La_{1-x}Sr_xCoO_{3-\delta}$, $La_{0.6}Sr_{0.4}Co_{1-y}Fe_yO_{3-\delta}$, $La_{0.8}Sr_{0.2}Sc_{1-y}Fe_yO_{3-\delta}$ and $La_{0.8}Sr_{0.2}Sc_{1-y}Fe_yO_{3-\delta}$"

Donglin HAN, Yusuke OKUMURA, Yoshitaro NOSE, Tetsuya UDA

Joint Symposium on Materials Science and Engineering for the 21st Century, Kyoto, Japan, September, 2009.

"Site Selectivity of Dopants in $BaZr_{1-x}M_yO_{3-\delta}$ (M = Dy, Eu, Sm) and Measurement of Their Water Contents, Concentrations of Oxide Ion Vacancies and Conductivities"

Donglin HAN, Yoshitaro NOSE, Kozo SHINODA, Tetsuya UDA

The 15th International Conference on Solid State Proton Conductors, Santa Barbara, USA, August, 2010.

"Site Selectivity of Dopant in Trivalent Rare Earth Cation Doped Barium Zirconate"

Donglin HAN, Kozo SHINODA, Yoshitaro NOSE, Tetsuya UDA

KIFEE International Symposium on Environment, Energy and Materials, Kyoto, Japan, March, 2011.

"Evaluation of Site Occupancy of Yttrium in Barium Zirconate"

Donglin HAN, Yusuke OKUMURA, Yoshitaro NOSE, Tetsuya UDA

Joint Symposium on Materials Science and Engineering for the 21st Century, Singapore, June, 2011.

Cu(In, Ga)Se$_2$ Solar Cell Absorber Film

Papers

"Selenization Temperature and Properties of CuInSe$_2$ Films"

Xiaofeng DING, Donglin HAN, Gong ZHANG, Daming ZHUANG

Chinese Journal of Vacuum Science and Technology, **26** (2006) 32-35.

"Influences of Se Source Temperature on Microstructure and Morphologies of CIGS Films"

Donglin HAN, Gong ZHANG, Daming ZHUANG, Jinshi YUAN, Jun SONG

Vacuum, **44** (6) (2007) 30-33.

"Influences of Bilayer Precursor Films on Microstructure and Morphology of CIGS Films"

Donglin HAN, Gong ZHANG, Daming ZHUANG, Jinshi YUAN, Chunlei LI

Chinese Journal of Vacuum Science and Technology, **28** (1) (2008) 78-82.

"Influences of N$_2$ flux on Microstructure and Morphologies of CIGS Films"

Donglin HAN, Gong ZHANG, Daming ZHUANG, Shenchun SHA, Jinshi YUAN

Journal of Functional Material, **39** (3) (2008) 446-448, 452.

"Influences of Carrier Gas on Microstructure and Morphologies of CIGS Films"

Donglin HAN, Gong ZHANG, Daming ZHUANG, Jinshi YUAN, Chunlei LI.

Chinese Journal of Vacuum Science and Technology, **28** (3) (2008) 235-239.

"Se Vapor Selenization Method Parameters for Deposition of CIGS Films (I)"

Donglin HAN, Gong ZHANG, Daming ZHUANG, Jinshi YUAN, Jun SONG,

Acta Energiae Solaris Sinica, **30** (4) (2009) 426-429.

"Se Vapor Selenization Method Parameters for Deposition of CIGS Films (II)"

Donglin HAN, Gong ZHANG, Daming ZHUANG, Jinshi YUAN, Chunlei LI,

Acta Energiae Solaris Sinica, **30** (5) (2009) 607-610.

Proceedings

"Influences of Flux of Carrier Gas on Microstructure and Morphologies of CIGS Films"

Donglin HAN, Gong ZHANG, Daming ZHUANG, Jinshi YUAN, Jun SONG

Proceedings of ISES World Congress 2007, (2008) 1289-1294.

"Influence of Ar Flux on Microstructure and Morphologies of CIGS Films"

Donglin HAN, Gong ZHANG, Daming ZHUANG, Jinshi YUAN, Jun SONG

The Proceedings of the China Association for Science and Technology, **7** (2011) Accepted

"Influence of Precursor Films on Microstructure and Morphologies of CIGS Films"

Donglin HAN, Gong ZHANG, Daming ZHUANG, Jinshi YUAN, Jun SONG

The Proceedings of the China Association for Science and Technology, **7** (2011) Accepted

Oral Presentation

"Influences of Flux of Carrier Gas on Microstructure and Morphologies of CIGS Films"

Donglin HAN, Gong ZHANG, Daming ZHUANG, Jinshi YUAN, Jun SONG

ISES Solar World Congress 2007, Beijing, China, September 2007.

Acknowledgements

I would like to express deep gratitude to Prof. Tetsuya Uda for offering me the precious opportunity to finish the doctoral course in Department of Materials Science and Engineering, Kyoto University, Japan, and also for the countless valuable discussions and advices during the last three years. I was especially greatly impressed by his tireless curiosity in research. In addition, at the very beginning, I was "pushed" by Prof. Uda to perform my first oral presentation in Japanese, my first poster presentation in English, *etc*. All these "firsts" are precious, leading me to enjoy the life as a real researcher.

I would also like to express my gratitude to Prof. Yoshitaro Nose for his valuable discussions and sincere supporting. A specially thing I want to mention is that he offered me the information and encouraged me to apply for research funding from Marubun Research Promotion Foundation, whose application document should be prepared in Japanese, seeming impossible for me at that time. However, I succeeded eventually, and recognized impressively that no attempt, no result, which is useful for all my life.

I am grateful to Prof. Yasuhiro Awakura for teaching me thermodynamics and electrochemistry with great patience. His knowledge, and also the life attitude are admirable.

I would like to thank Prof. Isao Tanaka and Prof. Haruyuki Inui for their valuable discussions and suggestions. I am grateful to Prof. Kozo Shinoda, Tohoku University, for teaching me the knowledge of X-ray diffraction, and great help in the experiment in SPring-8. I also want to thank Prof. Kyosuke Kishida for help of TEM analysis.